UNIVERSITY OF OKLAHOMA

GRADUATE COLLEGE

NON-LTI ANTENNA DESIGN AND MODELING TECHNIQUES

A DISSERTATION

SUBMITTED TO THE GRADUATE FACULTY

in partial fulfillment of the requirements for the

Degree of

DOCTOR OF PHILOSOPHY

By

STEPHEN BASS
Norman, Oklahoma
2022

Downloaded from SHAREOK. Persistent Handle URL: https://hdl.handle.net/11244/333868

NON-LTI ANTENNA DESIGN
AND MODELING TECHNIQUES

A DISSERTATION APPROVED FOR THE
SCHOOL OF ELECTRICAL AND COMPUTER ENGINEERING

BY THE COMMITTEE CONSISTING OF

Dr. Jessica Ruyle, Chair

Dr. K.C. Kerby-Patel, Co-Chair

Dr. Eric Abraham

Dr. Jay McDaniel

Dr. Justin Metcalf

Dr. Caleb Fulton

Dr. Kurt Schab

© Copyright by STEPHEN BASS 2022
All Rights Reserved.

Acknowledgments

Throughout the writing of this dissertation I have received a great deal of support and assistance.

I would first like to thank my supervisor, Dr. Jessica Ruyle, whose expertise was invaluable in formulating the research questions and methodology. Your insightful feedback pushed me to sharpen my thinking and brought my work to a higher level.

I would also like to thank Dr. K.C. Kerby-Patel and Dr. Kurt Schab for their insight and guidance. You provided me with the tools that I needed to choose the right direction and successfully complete my dissertation.

In addition, I would like to acknowledge my colleagues from the Radar Innovations Laboratory at the University of Oklahoma for their collaboration. I would particularly like to thank Kyle Kanaly and Clayton Blosser. Thank you for the discussion and for all of the ideas we bounced off each other in our research.

Finally, I would like to thank my parents for their wise counsel and sympathetic ear. You are always there for me.

Table of Contents

List of Tables viii

List of Figures ix

Abstract xiv

1 Introduction 1

2 Nonlinear Modeling 5
- 2.1 Harmonic Balance Circuit Analysis . . . 6
  - 2.1.1 History and Development . . . 7
  - 2.1.2 Harmonic Balance Methodology . . . 11
  - 2.1.3 Solvers . . . 21
- 2.2 Combining with MoM . . . 24
  - 2.2.1 Partition the Matrix . . . 25
  - 2.2.2 Equivalent Source Model . . . 26
- 2.3 Examples . . . 27
  - 2.3.1 Resistor, Inductor, and Capacitor Configurations . . . 28
  - 2.3.2 Diodes and Switches . . . 33
  - 2.3.3 Transistors . . . 39
  - 2.3.4 Diode-loaded Dipole Antenna . . . 45
- 2.4 Limitations and Advantages . . . 50
  - 2.4.1 Nonlinear Devices . . . 50
  - 2.4.2 Time-varying Devices . . . 52
- 2.5 Concluding Remarks . . . 53

3 Time-Variant Modeling 54
- 3.1 Conversion Matrix Circuit Analysis . . . 55
  - 3.1.1 Lumped Time-Varying Components . . . 55
  - 3.1.2 Loaded Multi-port Networks . . . 59
- 3.2 Conversion Matrix / Method of Moments . . . 62
  - 3.2.1 Formulation . . . 63
  - 3.2.2 Loading . . . 64
  - 3.2.3 Lumped Time-Varying Loads . . . 64

3.3 Examples . . . 65
3.3.1 Scattering from a singly-loaded bowtie dipole . . . 65
3.3.2 Harmonic generation in a multiply-loaded transmit system . . . 68
3.4 Rederiving Basic Network Relations with CMMoM . . . 70
3.4.1 Loading . . . 72
3.4.2 Reflection Coefficient . . . 72
3.4.3 Input Impedance . . . 74
3.5 Concluding Remarks . . . 75

4 Parametric Amplifiers 76
4.1 Configurations . . . 76
4.1.1 Series Configuration . . . 77
4.1.2 Shunt Configuration . . . 80
4.2 Realistic Time-varying Capacitor . . . 82
4.3 Parametric Amplifier-Based Antenna Designs . . . 84
4.3.1 Amplifier . . . 84
4.3.2 Merging with an LTI System . . . 85
4.3.3 Frequency Conversion . . . 85
4.4 Concluding Remarks . . . 85

5 Non-LTI Antenna Design 87
5.1 CMMoM Design Equations . . . 87
5.1.1 Single Time-Varying Load . . . 91
5.1.2 Interaction Between Multiple Loads . . . 91
5.2 Power Transfer and Loss . . . 92
5.2.1 Extincted Power . . . 93
5.2.2 LTI Antenna Circuit Model . . . 94
5.2.3 TV Antenna Circuit Model . . . 96
5.3 Impedance Matching . . . 101
5.4 Bounds on Performance Metrics . . . 107
5.4.1 Perfectly Tuned Structures - R Bound . . . 111
5.4.2 Efficiency Bound . . . 112
5.5 Realized Non-LTI Antenna Challenges . . . 114
5.5.1 Realized Components . . . 114
5.5.2 Non-LTI Measurements . . . 115
5.6 Concluding Remarks . . . 116

6 Conclusions and Future Work 117
6.1 Conclusions . . . 117
6.2 Future Work . . . 119
6.2.1 Combination of Harmonic Balance and CMMoM . . . 119
6.2.2 Interactions between Time-Varying Components . . . 120
6.2.3 Antenna Designs . . . 120

6.2.4 Fundamental Bounds 120
6.2.5 Data Integrity and Capacity 121
6.3 Scientific Impact 121
6.3.1 Dissertation Contributions 121
6.3.2 Publications and Conferences 122

References **125**

List of Tables

3.1 Comparison of backscatter (dBsm) data from Fig. 3.4 68

List of Figures

2.1 Arbitrary networks representing different subcircuits. The networks can be disconnected and additional sources added to keep the voltages and currents inside each network identical [44]. 12
2.2 Simple DC circuit illustrating the subcircuit concept. 13
2.3 Circuit divided into linear and nonlinear subcircuits with N ports connecting them and two additional source/load ports. Source and load ports can also be added with the source and load impedances absorbed into the subcircuits [26]. 15
2.4 Circuit divided into linear and nonlinear subcircuits with N ports connecting them. The source/load ports have been absorbed into the linear subcircuit so a current source appears at each port [26]. 18
2.5 Equivalent source model using the solved voltages at the nonlinear loads as additional voltage sources at the harmonic frequencies. 27
2.6 Comparison of the charge-voltage relationship of linear and nonlinear capacitors. 29
2.7 Circuit diagram of the series RC circuit. The voltage and current were measured at the node between the resistor and capacitor. 29
2.8 Response of a linear capacitor in an RC circuit where $R = 2\ \Omega$, $C = 500\ pF$, and the voltage source has an amplitude of 2 V at a frequency of 0.5 GHz. 31
2.9 Response of a nonlinear capacitor in an RC circuit where $R = 2\ \Omega$, $C = 500\ pF$, and the voltage source has an amplitude of 2 V at a frequency of 0.5 GHz. 32
2.10 Response of a nonlinear capacitor in an RC circuit where $R = 2\ \Omega$, $C = 500\ pF$, and the voltage source has an amplitude of 10 V at a frequency of 0.5 GHz. 34
2.11 Circuit diagram of the tank LC circuit with a series resistance. The voltage and current were measured on the capacitor on the end near the resistor and inductor. 35
2.12 Response of a nonlinear capacitor in an RLC circuit where $R = 2\ \Omega$, $C = 500\ pF$, $L = 0.15\ nH$, and the voltage source has an amplitude of 10 V at a frequency of 0.5 GHz. 36
2.13 The voltage-current relationship of a realistic diode shown at two different scales. Note that in (a), the current is in μA. 37

2.14 Circuit diagram of the series resistor and diode circuit. The voltage and current were measured at the node between the resistor and the diode. . . . 37
2.15 Response of a diode in series with a 2 Ω resistor and the voltage source has an amplitude of 10 V at a frequency of 0.5 GHz. 38
2.16 Circuit diagram of the series resistors and switch circuit. The voltage and current were measured at the node between the first resistor and the switch. 39
2.17 Response of a 4 GHz triggered switch in series with two resistors where $R = 1\ \Omega$ and the voltage source has an amplitude of 1 V at a frequency of 0.5 GHz. 40
2.18 Common-source MOSFET amplifier with a biasing voltage divider. The voltage bias on the gate is controlled by changing the grounded gate resistor, $RG2$. 41
2.19 Small signal model of the amplifier shown in Figure 2.18. This model assumes no DC bias, but uses a current source that has the parameters of a biased transistor. 42
2.20 Drain current and voltage for given gate voltages. The vertical red line shows the bias voltage for linear operation at 3.46 V, and the two purple lines show the limits of the small signal modulation. 42
2.21 Response of a linearly biased MOSFET amplifier. The voltage was amplified by about 2.45 times to achieve a 0.245 V peak. 44
2.22 Response of a small signal model of the linearly biased MOSFET amplifier. The voltage was amplified by about 2.45 times to achieve a 0.245 V peak. . 46
2.23 Drain current and voltage for given gate voltages. The vertical red line shows the bias voltage for nonlinear operation at 1.61 V, and the two purple lines show the limits of the small signal modulation. 47
2.24 Response of a nonlinearly biased MOSFET amplifier. The voltage was amplified by about 0.13 times to achieve a 0.013 V peak. 48
2.25 Response of a small signal model of the nonlinearly biased MOSFET amplifier. The voltage was amplified by about 0.13 times to achieve a 0.013 V peak. 49
2.26 Current distribution and radiation characteristics for a 75 mm wire dipole loaded with a diode at its center. The time- and frequency domain current through the diode is shown in (a), and the current distribution across the dipole at each simulated frequency is shown in (b) in a logarithmic scale to show the magnitude at each harmonic. The total power radiated is shown in (c) with the backscatter pattern shown in (d). 51

3.1 Frequency convention used throughout this chapter. Time-varying loads are represented in Fourier series of the fundamental frequency ω_0, e.g., $\{G_k\}$, while current and voltage indexing centers around a modulation frequency ω_c. 58

3.2 Diagram of LTI multiport system (a) and periodically time-varying multiport system (b) as represented by a conversion matrix. Double slash across port symbol denotes N physical ports. Each physical port supports voltages and currents at each of the $2K + 1$ harmonic frequencies. An LTI system with $2K+1$ frequencies can be represented by $2K+1$ independent linear systems, or a block diagonal conversion matrix, because there is no conversion between frequencies. 60
3.3 Discretization of a structure Ω (left) into finite elements supporting localized basis functions $\{\boldsymbol{\psi}_n\}$ (right). RWG basis functions [74] are depicted, with each basis function centered on one mesh edge and spanning two adjacent triangles. 63
3.4 Cross-frequency backscatter spectra from CMMoM, transient circuit co-simulation, FDTD, and measurement, compared to backscatter from LTI bowtie. Inset schematic. 66
3.5 Normalized backscattered power (dBsm) of the bowtie example from CMMoM vs. declination angle θ in the xz plane for the frequencies of greatest returned power. 69
3.6 CMMoM calculation of broadside radiated electric fields from a transmitting square loop loaded with two time-varying resistive or capacitive loads. Load (blue) and voltage source (red) locations are shown on the inset schematic. 71
3.7 Diagram of a transmission line of length L, characteristic impedance Z_0, and propagation constant β that is loaded with a time-varying impedance $\hat{\mathbf{Z}}_{\mathrm{L}}$. 71

4.1 Basic design of a parametric amplifier. 77
4.2 Shunt configuration of a parametric amplifier. 80
4.3 Tuning circuit Z_T shown in series with the time-varying capacitance C_3. . . 83

5.1 Equivalent circuit model of single-port antenna loaded with a port impedance Z_c. The antenna has an input impedance Z_a and input power P_{in} that change with the frequency and excitation as a function of the antenna geometry. 95
5.2 Equivalent circuit model of single-port antenna loaded with a tuning capacitance C_T and a port impedance Z_c. The added capacitance forces the antenna to resonate at the excitation frequency. The antenna has an input impedance Z_a and input power P_{in} that change with the frequency and excitation as a function of the antenna geometry. 96

5.3 Equivalent circuit model of single-port antenna loaded with a port impedance Z_c and a time-varying component with an input impedance $Z_{TV,\text{in}}$. The time-varying component takes the place of the capacitor in Figure 5.2 and forces the antenna to resonate at a broad range of frequencies around the excitation frequency. The antenna has an input impedance Z_a and input power P_{in} that change with the frequency and excitation as a function of the antenna geometry. 97
5.4 Equivalent circuit model of single-port antenna loaded with a port impedance Z_c and a time-varying component $\hat{\mathbf{Z}}_{TV}$. The time-varying component has been expanded into an equivalent two-port network and the antenna impedance at the harmonic frequency Z_a^1. The antenna has an input impedance Z_a^0 and input power P_{in} that change with the frequency and excitation as a function of the antenna geometry. 98
5.5 Equivalent circuit model of single-port antenna loaded with a port impedance Z_c and a time-varying component $\hat{\mathbf{Z}}_{TV}$. The time-varying component has been fully expanded into a dependent source model with the parameters from the time-varying component in (5.32). The antenna has an input impedance Z_a^0 and input power P_{in} that change with the frequency and excitation as a function of the antenna geometry. 99
5.6 A square loop antenna with a side length of 12mm and driven by a lumped port excitation on one side. Its input impedance is shown in (b) and has a resonance at 3 GHz. 102
5.7 The square loop antenna from Figure 5.6 now tuned with a time-varying resistor at the excitation port. The time-varying resistor had a magnitude of $r_0 = 860\ \Omega$ and a frequency of 3 GHz. The reactance has been canceled for the lower frequencies as shown in (a), but the efficiency has been greatly reduced by the resistance of the load, shown in (b). 103
5.8 Power quantities on the square loop antenna from Figure 5.6 tuned with a sinusoidally time-varying resistor at the excitation port. The time-varying resistor had a magnitude of $r_0 = 860\ \Omega$ and a frequency of 3 GHz with one negative harmonic used and the port impedance Z_c is equal to the resistance of the antenna. The different power quantities derived in Section 5.2 are shown in (b) for different loading types and the power received by the port impedance Z_c is compared in (c). 104
5.9 Power quantities on the square loop antenna from Figure 5.6 tuned with a sinusoidally time-varying resistor at the excitation port. The time-varying resistor had a magnitude of $r_0 = 860\ \Omega$ and a frequency of 3 GHz with one negative harmonic used and the port impedance Z_c is equal to $50\ \Omega$. The different power quantities derived in Section 5.2 are shown in (b) for different loading types and the power received by the port impedance Z_c is compared in (c). 105

5.10 Power quantities on the square loop antenna from Figure 5.6 tuned with a sinusoidally time-varying resistor at the excitation port. The time-varying resistor had a magnitude of $r_0 = 860\ \Omega$ and a frequency of 3 GHz with one negative harmonic used and the port impedance Z_c is equal to the magnitude of the time-varying resistor. The different power quantities derived in Section 5.2 are shown in (b) for different loading types and the power received by the port impedance Z_c is compared in (c). 106
5.11 Power quantities on the square loop antenna from Figure 5.6 tuned with a switching time-varying resistor at the excitation port. The time-varying resistor had a magnitude of $r_0 = 687\ \Omega$ and a frequency of 3 GHz with 10 negative harmonics used and the port impedance Z_c is equal to the resistance of the antenna. The different power quantities derived in Section 5.2 are shown in (b) for different loading types and the power received by the port impedance Z_c is compared in (c). 108
5.12 Power quantities on the square loop antenna from Figure 5.6 tuned with a switching time-varying resistor at the excitation port. The time-varying resistor had a magnitude of $r_0 = 687\ \Omega$ and a frequency of 3 GHz with 10 negative harmonics used and the port impedance Z_c is equal to $50\ \Omega$. The different power quantities derived in Section 5.2 are shown in (b) for different loading types and the power received by the port impedance Z_c is compared in (c). 109
5.13 Power quantities on the square loop antenna from Figure 5.6 tuned with a switching time-varying resistor at the excitation port. The time-varying resistor had a magnitude of $r_0 = 687\ \Omega$ and a frequency of 3 GHz with 10 negative harmonics used and the port impedance Z_c is equal to the magnitude of the time-varying resistor. The different power quantities derived in Section 5.2 are shown in (b) for different loading types and the power received by the port impedance Z_c is compared in (c). 110
5.14 Optimal extincted power P_{ex}^{opt} using the R bound for a sphere of radius $a = 1\ \mathrm{cm}$ at 100 MHz with a surface resistance $R_s = 0.01\ \Omega$. Results shown for the LTI case of a static load resistance and two different load frequencies f_0. 112
5.15 Efficiency bound for a sphere of radius $a = 1$ cm at 100 MHz with a surface resistance $R_s = 0.01\ \Omega$ (left) and $R_s = 100\ \Omega$ (right). Results shown for the LTI case of a static load resistance and two different load frequencies f_0. 114

Abstract

Nearly all contemporary antenna systems are Linear Time-Invariant (LTI) devices, and allow for assumptions of frequency independence and reciprocity, but are governed by strict bounds on their performance. Recently, nonlinear and time-varying (non-LTI) antennas have become a common path of research in an attempt to break the LTI assumption and improve antenna performance beyond these limits, but lack a general modeling technique to develop fundamental equations for antenna design. The adaptability of the established method of moments (MoM) allows for a complete model of virtually any structure. Conversely, the conversion matrix method allows the expansion of circuit and network parameters to model time-varying structures. The combination of the two methods allows for a generalized model of a time-varying antenna while granting insight into their design. In a similar way, MoM can be combined with the harmonic balance method and allow for the accurate simulation of nonlinear components and pumped nonlinearities on antennas of arbitrary structure. These aspects of MoM, conversion matrices, and harmonic balance are leveraged in this work to provide a better understanding of non-LTI antennas and develop several models for achieving better performance or different capabilities.

Chapter 1

Introduction

Linear and time-invariant (LTI) structures have been used in electromagnetic systems to great effect because they allow engineers to assume frequency independence and reciprocity as well as simplify Maxwell's equations. Even structures that are not strictly LTI can generally be assumed to be LTI for some region of operation (e.g., amplifiers). Specifically for antennas, fundamental performance bounds have been derived using the LTI assumption [1]–[5], but recently, time-varying and nonlinear (non-LTI) structures have become a common path of research in an attempt to break these LTI performance bounds [6]–[11].

Non-LTI electromagnetic structures are capable of exhibiting unique behaviors beyond the capabilities of their LTI counterparts. The interaction between a time-varying or nonlinear structure and a time-varying voltage creates currents on harmonic frequencies which may not be present in the original excitation. This phenomenon is called the "Rusty Bolt Effect" [12]. Examples of non-LTI antenna systems include the use of active and non-Foster matching [6]–[8], direct antenna modulation [9]–[11], and time-varying loading whose modulation rate is comparable to the carrier or antenna resonant frequency (as opposed to the symbol rate) [13]–[17]. These methods all involve locally time-varying or nonlinear loading, though the effects of distributed time-variation, i.e., space-time modulated materials, have also been explored [18]–[25]. While non-LTI structures may offer

an improvement over the typical LTI systems, their modeling and simulation is generally more difficult. To fully explore the combination of non-LTI structures on antennas, robust electromagnetic solvers must first be established. This dissertation investigates a couple of solvers and discusses their application to non-LTI antennas.

Nonlinear components have a nonlinear voltage-current relationship, such as in the case of a diode, but do not necessarily change with time. Occasionally it is possible to analyze a nonlinear component in a predefined linear range of operation so that it can easily be incorporated into another linear system [26], removing the need for a specialized solver. However, other applications require further analysis, such as in mixers and frequency multipliers, where the nonlinear behavior of the component is necessary. There are many different nonlinear circuit solvers in use today. They can be largely grouped into three different categories: time domain, frequency domain, and hybrid methods [26]–[29]. Time-domain methods are useful in that they directly solve numerical equations that describe nonlinear currents and accurately calculate both the transient and steady-state responses, but they are unable to easily solve transmission lines or sub-networks defined by network parameters [26]–[28], [30]. Frequency domain methods, such as Volterra-series and power-series, are designed for frequency and network analysis and can easily handle transmission lines and network parameters, but struggle to model strong nonlinearities [27]. Hybrid methods, specifically harmonic balance, combine the advantages of time and frequency domain solvers and operate in both domains, and are common solvers for complex nonlinear circuits and networks of impedances [27], [28]. Expansion of harmonic balance to model a full electromagnetic structure should be possible through integration with a circuit or network model of the structure.

Time-varying devices, on the other hand, change their properties over time but maintain their linearity at any given point in time. Most of the modeling of time-varying electromagnetic structures relies on time-domain techniques such as the finite difference time

domain method (FDTD), transient circuit co-simulation, and time-domain method of moments [12]. While these techniques are accurate and extremely general, they have certain disadvantages that motivate the development of alternative modeling strategies [31]. For example, full-wave transient analyses have few opportunities for partial simulation re-use between variations of time-varying properties. Additionally, these methods do not directly represent frequency domain phenomena frequently employed in the design of LTI systems (e.g., steady-state radiated power, network parameters), though these can be obtained via Fourier transformations. By contrast, frequency-domain techniques often afford significant opportunities for partial simulation re-use and their formulations naturally align with many common frequency domain metrics. In particular, conversion matrices enable the analysis of time-varying structures in the frequency domain by modeling the mixing properties and harmonic generation of time-varying structures as interactions between networked ports, allowing integration with strictly LTI-based solvers. Early uses combined conversion matrices with the method of moments (MoM) to model time-varying electromagnetic structures, but have focused on sparse loading or the reduction of an antenna to a single lumped impedance, ignoring the potential interaction between multiple or distributed time-varying loads. But by leveraging the multiport formulation of conversion matrices, it can be fully integrated with MoM, preserving the full MoM analysis of electromagnetic structures and providing a framework to efficiently model any number of lumped or distributed loads and the interactions between them [32], [33].

The capabilities of non-LTI circuits and their integration with electromagnetic structures have been modeled with both frequency- and time-domain approaches[26], [27], [29], but a versatile method that can incorporate arbitrary loading with non-LTI components while still providing design insight is not currently established. This dissertation seeks to define methods of analyzing non-LTI electromagnetic structures by combining a non-LTI circuit solver (harmonic balance or conversion matrices) with a full LTI electromagnetic

solver (MoM). First, in Chapters 2 and 3, the key aspects of harmonic balance and conversion matrices are reviewed before expanding them with MoM into their full form. Then, in Chapter 4, a brief analysis is performed on parametric amplifiers to gain insight into how non-LTI structures can be utilized, followed by an investigation in Chapter 5 into the structures of the resulting non-LTI solvers to determine how non-LTI loading can affect the performance of an electromagnetic scatterer. Additionally, a method of determining fundamental bounds on several performance metrics based on MoM is derived and applied to different case studies. Finally Chapter 6 concludes with an analysis of the methods and a discussion of future work in this area.

Chapter 2

Nonlinear Modeling

There are many different nonlinear circuit solvers in use today. They can be largely grouped into three different categories: time-domain, frequency-domain, and hybrid methods [26]–[29]. Time-domain methods are useful in that they directly solve numerical equations that describe nonlinear currents and accurately calculate both the transient and steady-state responses, but they are unable to easily solve transmission lines or subnetworks defined by network parameters [26]. As a special kind of time-domain analysis, the Shooting method is a method of analyzing transmission line parameters with nonlinear circuits in the time domain, but it assumes a periodic input and only a steady-state solution [27], [28], [30].

Frequency-domain methods, on the other hand, such as Volterra-series and power-series, are designed for frequency and network analysis and can easily handle transmission lines and network parameters, but have their own problems. Their main focus is to model the interaction of multiple input signals in a weakly-nonlinear system, but cannot handle strong nonlinearities. Another frequency-domain solver, frequency-domain spectral balance (FDSB) takes a similar approach to the harmonic balance methods described in the following chapters and seeks to balance out the spectra of the linear and nonlinear components [27]. Originally needing a power-series description of the nonlinear system to utilize these methods, this restriction was later removed, enabling the use of these methods in more diverse systems.

Hybrid methods, such as harmonic balance, combine the advantages of time- and frequency-domain solvers and operate in both domains [27], [28]. Specifically, harmonic balance analyzes the linear components, such as transmission lines and other network parameters, in the frequency-domain where they are more easily defined. The nonlinear components, on the other hand, are analyzed in the time domain where virtually any equation can be used to describe their steady-state functionality. The solutions from the different components are brought back together in the same domain with a Fourier transform and compared. In this way, harmonic balance is able to take the best parts from the other nonlinear analysis methods and combine them into a powerful nonlinear circuit solver. The following sections seek to provide understanding in the basic theory of harmonic balance and the related Co-simulation and provide examples of how they can be used.

2.1 Harmonic Balance Circuit Analysis

Harmonic balance, in general terms, is the method of analyzing a nonlinear, steady-state system and balancing the harmonics produced by different parts of the system [27], [34]. For electrical circuits in particular, this method balances out the voltages and currents produced by any linear and nonlinear lumped component in the circuit using Kirchoff's voltage and current laws [28], [35]. The major differences between the harmonic balance methods are primarily in how parts of the circuit are combined and the type of solver used [26]. In this chapter, a general overview of the history of harmonic balance will be presented, then the two primary methods of harmonic balance for electrical circuits will be discussed in further detail.

2.1.1 History and Development

2.1.1.1 Initial Conception and Application to Electrical Circuits

The term “harmonic balance” was first used by Kryloff and Bogoliuboff as a part of their book “Introduction to Nonlinear Mechanics” originally published in 1937 and translated into English in 1943 [34], [36]. Based on a Galerkin Method [27], [37]–[39], they approximate the solutions to nonlinear systems as the summation of harmonic sinusoids because nonlinear systems usually have a response with a period that is a rational multiple of the input period [40]. With this method they were able to solve systems such as the oscillatory shaft, the pendulum, as well as a couple of simple electrical circuits with resistance.

In 1968 and 1969, the theory was further developed for electrical networks composed of nonlinear lumped elements by Baily [40] and Lindenlaub [41]. Referred in this communication as “classic harmonic balance”, this method assumes a solution to a nonlinear circuit as a number of weighted harmonic sinusoids governing the electrical charge and magnetic flux through nonlinear capacitors and inductors. It then applies Kirchoff’s voltage and current laws in the time domain and sums up all of the currents leaving a node and the voltage changes in a loop. Because these should add up to zero, any different result is calculated as a mean-square error [35]. The charge and flux is then modified based on this error to obtain a more accurate solution. This process is repeated through a minimization technique until the error is suitably low [40].

2.1.1.2 Problems and Small Improvements

At this time, the method of harmonic balance was not widely accepted because of several issues with the initial implementation [30]. The assumed solution could be unstable, be missing an important harmonic, or have no relation to the actual solution and were highly dependent on the initial guess [30]. The optimization techniques had convergence problems

stemming from the mean-square error and the low computational power of computers at that time. Additionally, these techniques could only produce steady-state solutions and could not provide the transient response. Finally, the implementation of the method resulted in some configurations producing invalid matrices and breaking the process [40].

While the initial harmonic balance method had some problems, changes were gradually made to help mitigate them, primarily focusing on the method of optimization. In 1974, the Newton Iteration procedure was used to minimize the error in the harmonic balance method in a Schottky diode mixer [42]. While this method depended greatly on the initial guess and sometimes could not converge with large voltages, it helped bring attention to the method. A year later, the Relaxation Iteration procedure was used on a similar diode mixer, but improved on the convergence and the allowed larger voltages to be used [43].

2.1.1.3 New Methods

The harmonic balance method was further improved significantly in 1976 with the new piecewise harmonic balance [44]. This is the method that is commonly known as harmonic balance today [27], [28], but here it will still be referred to as "piecewise harmonic balance", while "harmonic balance" will refer to the general theory. The new piecewise harmonic balance method took advantage of the fact that usually most of an electrical network is linear. The network could then be split up into a linear subcircuit and a nonlinear subcircuit and evaluated as two separate networks with connecting ports. The linear subcircuit could be analyzed as a normal linear network in the frequency domain, while the nonlinear subcircuit could still be analyzed in the time domain [26], [44]. Once evaluated, the nonlinear subcircuit could then converted back to the frequency domain using a Fourier transform. The solution set became the voltages across each of the nonlinear ports, and the currents resulting from each subcircuit would then be solved independently. From here, a similar analysis to classic harmonic balance could be done to balance out the resulting

voltages and currents that appear at the terminals of each port using Kirchoff's Laws and optimization techniques, but could now be done in the frequency domain [26], [44], [45]. This allowed the the final cost equation to have an multi-variable error function for each harmonic so that later, in 1990 [29], the optimization function could balance out each harmonic instead of the resulting time-domain waveform. The piecewise method's primary improvements over the classic method is that it simplifies the linear subcircuit, reduces the number of variables to be optimized, and allows the analysis of Kirchoff's Laws in the frequency domain [28]. This method is discussed in more detail in Section 2.1.2.

Later, in 1986, another method, called nodal harmonic balance, was introduced [45]. When many nonlinear components are considered, such as in MMICs, removing the nonlinear subcircuit can sometimes result in a linear network with singular-network parameters [26]. Nodal harmonic balance fixed many of these cases by changing the solution set of piecewise harmonic balance from the voltages on each port to the voltages on each node. This method was more tolerant of circuit disconnections, but did not always solve the problem [26]. Outside of these cases, nodal harmonic balance has not seen much use because there are usually more nodes in a circuit than nonlinear components, so the greater number of variables to be solved takes longer for the solution to converge.

2.1.1.4 Further Improvements and Applications

Over the years since, several modifications and improvements were made to improve convergence such as the continuation method, which gradually increases the power from the source so that the circuit appears linear at first, then gradually becomes nonlinear with more power [26], [46]. More recently, the addition of the Block Newton Algorithm introduced in 1990 enabled the simultaneous solution of error functions for each harmonic, instead of a single mean-squared error for the entire system, and allowed the harmonic balance method to converge faster and more accurately [29].

Additionally, while piecewise and nodal harmonic balance both assume there is only one primary signal input frequency and all others are harmonically related, there is a large class of nonlinear problems that require multiple inputs from very different frequencies, such as mixers and power amplifiers [26]. For many of these cases, a kind of "Large-Signal/Small-Signal" analysis can be used to approximate a solution. This approximation uses conversion matrices and assumes that when a large signal is modulated with a vanishingly small signal, the impact of the small signal on the circuit can be approximated as linear. First, in the "Large-Signal" analysis, harmonic balance is performed on the circuit with the large signal. The resulting voltages and currents can be combined to approximate a time-varying impedance or conductance. Then the "Small-Signal" analysis can be done over the approximately-linear circuit with the time-varying impedance and just the small signal so that an approximate solution can be obtained [26]. This method cannot be used in determining saturation or intermodulation distortion, but can be used for mixer conversion efficiency, port impedances, and adding time-varying components.

When there are multiple input signals of different frequencies and significantly large magnitude, the "Large-Signal/Small-Signal" approximation will not work. For these cases, a different method called multi-tone harmonic balance or generalized harmonic balance can be used to account for all of the possible harmonics [26], [47]. This modified harmonic balance method solves for all possible linear combinations of the input frequencies. Solving such a system often requires using the almost periodic discrete Fourier transform [48], [49], the multi-dimensional Fourier transform [50], or special frequency mapping [26], which are not simple processes. With these changes and the additional piecewise and nodal methods, harmonic balance has managed to become one of the preferred nonlinear microwave circuit techniques [27]–[29].

2.1.2 Harmonic Balance Methodology

While the different harmonic balance methods all vary in terms of assumptions, applications, and specific steps, every harmonic balance method has the same basic procedure:

1. Guess a solution (usually a set of zeros).
2. Solve the electrical circuit with the assumed solution.
3. Apply Kirchoff's Laws and calculate the error.
4. If the error is too large, modify the assumed solution and start again.

These steps are usually placed inside an optimization function set to minimize the error. The primary differences between harmonic balance methods are the types of solution, how the electrical circuit is solved, and what kind of minimization function is used. In this section, the piecewise and nodal harmonic balance methods will be discussed and will point out the assumptions that are made, how they have been used in the past, and what kinds of structures they were designed for.

2.1.2.1 Theory

Assume a network exists that can be split into two subnetworks, as in Figure 2.1.a. Additionally, assume that the two subnetworks are not identical and that there are no sources in one subnetwork which are dependent on a voltage or current in the other. This split, but connected, network has a specific, time-varying voltage across the connecting port, $v(t)$, and a related current flowing between the two subnetworks, $i(t)$ or $i(v(t))$. If the two subnetworks are completely disconnected, and a source is placed at each port that mimics the voltage or current of the connected network at the port, as in Figure 2.1.b, then the voltages and currents inside each of the subnetworks will match those of the connected circuit in Figure 2.1.a [44].

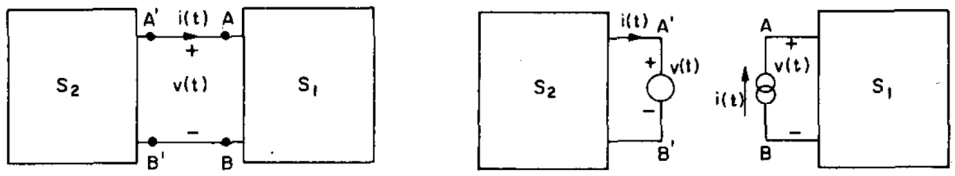

(a) Network composed of two subcircuits

(b) Disconnected network with equivalent sources

Figure 2.1: Arbitrary networks representing different subcircuits. The networks can be disconnected and additional sources added to keep the voltages and currents inside each network identical [44].

In the same way, if a different voltage source, $v_1(t)$, is connected to the disconnected network S_1 of Figure 2.1.b so that $v_1(t) \neq v(t)$, a resulting current $i_1(t)$ will flow through the terminal. Similarly, if the same voltage source $v_2(t) = v_1(t) \neq v(t)$ is connected to S_2, a current $i_2(t)$ will flow through its terminal. Because the two subnetworks, S_1 and S_2, are not identical, the resulting currents will not be equal, or in other words $i_2(t) \neq i_1(t)$.

For example, consider the network in Figure 2.2.a. The resulting voltage v and current i at the terminals of R_2 are easily determined as

$$v = V_D \frac{R_2}{R_1 + R_2} \qquad \text{and} \qquad i = \frac{V_D}{R_1 + R_2}. \tag{2.1}$$

So for $V_D = 6\ V$, $R_1 = 5\ \Omega$, and $R_2 = 10\ \Omega$, the resulting voltage and current are $v = 4\ V$ and $i = 0.4\ A$, respectively. In the same way described above, the circuit can be split into two subcircuits as shown in Figure 2.2.b. If each of the voltages on the terminals are also set as $v_1 = v_2 = 4\,V = v$, then the currents across each terminal can be calculated as $i_1 = i_2 = 0.4\ A$. As described previously, the voltage sources on the terminals of a subcircuit are mimicking the effect of the other subcircuit. However, if a different voltage is chosen, for example $v_1 = v_2 = 5\,V \neq v$, then the resulting currents are $i_1 = 0.2\ A$ and $i_2 = 0.5\ A$. By defining the error as $\epsilon = i_2 - i_1$, a metric can be obtained to evaluate the accuracy of the voltage. If the correct voltage was unknown, this error could then be

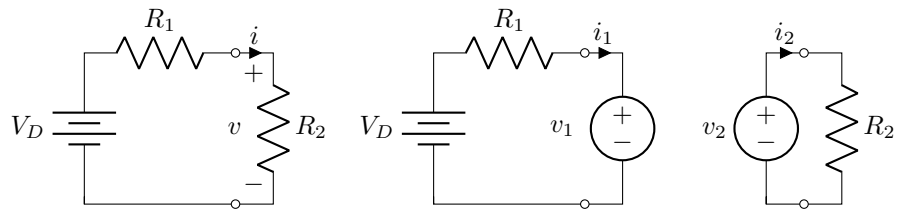

(a) Connected circuit (b) Disconnected circuit with added voltage sources

Figure 2.2: Simple DC circuit illustrating the subcircuit concept.

minimized using optimization techniques to solve for the correct voltage.

The process described above is simply a rederivation of Kirchoff's Current Law [35]. If all positive currents were defined as entering a network (or leaving a port), then all currents in a port must sum to zero, or

$$0 = \sum_m i_{mn}(t) \tag{2.2}$$

for every m current on port n. Additionally, because (2.2) is a linear operation, the same can be said for the currents in the frequency domain as

$$0 = \sum_m I_{mn}(k\omega_p) \tag{2.3}$$

where $I_{mn}(\omega) = \mathscr{F}\{i_{mn}(t)\}$ and $I_{mn}(k\omega_p)$ is the k-th harmonic of the fundamental frequency ω_p of I_{mn}.

In most cases, the voltage at all N ports will not be known. If a guess is made, a current will appear at each node, as described in the example from Figure 2.2. The resulting currents will probably not satisfy Kirchoff's Current Law, so the error function of the voltage guess can be defined in the frequency domain as

$$\epsilon_{n,k} = \sum_m I_{mn}(k\omega_p) \tag{2.4}$$

where $\epsilon_{n,k}$ is defined as the error for the k-th harmonic on the n-th port and the error vector

can be defined as

$$\underline{\epsilon} = \sum_m \underline{\mathbf{I}}_m \tag{2.5}$$

where $\underline{\epsilon}$ is a column vector of length $N(K+1)$ containing all of the errors of K harmonics (including DC) and N ports. Likewise, $\underline{\mathbf{I}}_m$ is a similar column vector containing all of the K harmonics of the m-th current leaving all N of the ports. These vectors are organized as

$$\underline{\mathbf{X}} = \begin{bmatrix} \mathbf{X}_1 \\ \mathbf{X}_2 \\ \mathbf{X}_3 \\ \vdots \\ \mathbf{X}_N \end{bmatrix} \qquad \text{where} \qquad \mathbf{X}_n = \begin{bmatrix} X_{n,0} \\ X_{n,1} \\ X_{n,2} \\ \vdots \\ X_{n,K} \end{bmatrix} \tag{2.6}$$

and $X_{n,k}$ is the k-th harmonic on the n-th port. The error vector, $\underline{\epsilon}$, can now be minimized through an optimization function to solve for the K voltage harmonics on N ports. In this way, the harmonics are almost literally being "balanced".

At this point, the piecewise and nodal harmonic balance methods begin to diverge. Specifically, the piecewise method deals with the voltages and currents on each *port*, while the nodal method deals with the voltages and currents on each *node*. Because of this, the nodal method tends to have more variables and takes longer to solve, but is less likely to have to use singular matrices. The derivation will continue to be discussed in terms of ports, but the nodal method has a similar process.

The next step is to define the individual subnetworks or subcircuits and the m currents on each port as functions of the voltages on each port. It is useful at this point to split the network into linear and nonlinear subnetworks or subcircuits as in Figure 2.3. The new

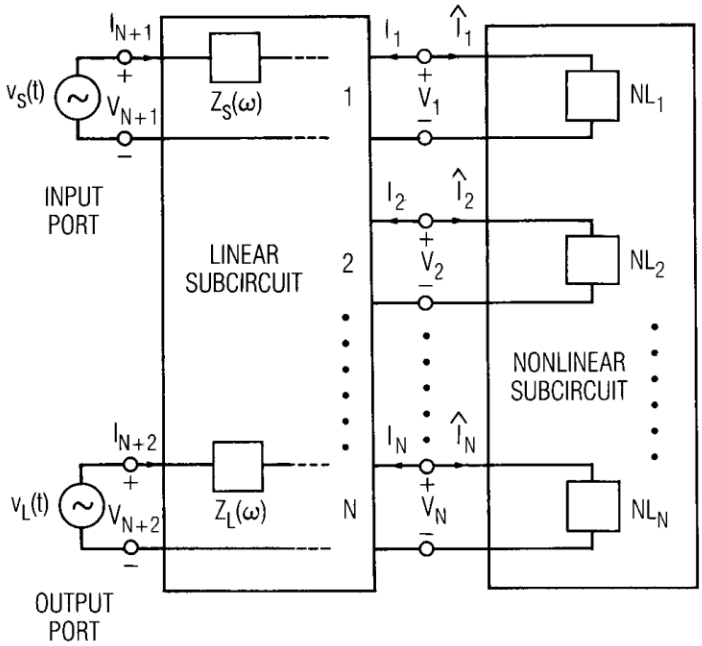

Figure 2.3: Circuit divided into linear and nonlinear subcircuits with N ports connecting them and two additional source/load ports. Source and load ports can also be added with the source and load impedances absorbed into the subcircuits [26].

error vector for all N ports, originally defined in (2.5), becomes

$$\underline{\epsilon} = \underline{\mathbf{I}}_{LIN} + \underline{\mathbf{I}}_{NL} \tag{2.7}$$

where $\underline{\mathbf{I}}_{LIN}$ is a column vector of the current harmonics on each port entering the linear subcircuit and $\underline{\mathbf{I}}_{NL}$ is a column vector of the current harmonics on each port entering the nonlinear subcircuit. Both vectors are of the same format as in (2.6). Each subnetwork or subcircuit can be handled separately and must be handled differently.

The linear subcircuit can be analyzed like a normal network, but must also take into account the current coming from the sources. Because it is desired to calculate current as a function of voltage, admittance parameters are used. The admittance matrix of the linear

subcircuit takes the form

$$\begin{bmatrix} \mathbf{I}_1 \\ \mathbf{I}_2 \\ \mathbf{I}_3 \\ \vdots \\ \mathbf{I}_N \\ \mathbf{I}_{N+1} \\ \mathbf{I}_{N+2} \end{bmatrix} = \begin{bmatrix} \mathbf{Y}_{1,1} & \mathbf{Y}_{1,2} & \dots & \mathbf{Y}_{1,N} & \mathbf{Y}_{1,N+1} & \mathbf{Y}_{1,N+2} \\ \mathbf{Y}_{2,1} & \mathbf{Y}_{2,2} & \dots & \mathbf{Y}_{2,N} & \mathbf{Y}_{2,N+1} & \mathbf{Y}_{2,N+2} \\ \mathbf{Y}_{3,1} & \mathbf{Y}_{3,2} & \dots & \mathbf{Y}_{3,N} & \mathbf{Y}_{3,N+1} & \mathbf{Y}_{3,N+2} \\ \vdots & \vdots & \ddots & \vdots & \vdots & \vdots \\ \mathbf{Y}_{N,1} & \mathbf{Y}_{N,2} & \dots & \mathbf{Y}_{N,N} & \mathbf{Y}_{N,N+1} & \mathbf{Y}_{N,N+2} \\ \mathbf{Y}_{N+1,1} & \mathbf{Y}_{N+1,2} & \dots & \mathbf{Y}_{N+1,N} & \mathbf{Y}_{N+1,N+1} & \mathbf{Y}_{N+1,N+2} \\ \mathbf{Y}_{N+2,1} & \mathbf{Y}_{N+2,2} & \dots & \mathbf{Y}_{N+2,N} & \mathbf{Y}_{N+2,N+1} & \mathbf{Y}_{N+2,N+2} \end{bmatrix} \begin{bmatrix} \mathbf{V}_1 \\ \mathbf{V}_2 \\ \mathbf{V}_3 \\ \vdots \\ \mathbf{V}_N \\ \mathbf{V}_{N+1} \\ \mathbf{V}_{N+2} \end{bmatrix} \tag{2.8}$$

where $\mathbf{I}_n$ and $\mathbf{V}_n$ contain K harmonics of the n port as in (2.6). $\mathbf{Y}_n$, on the other hand, is a $K+1$ diagonal matrix of the form

$$\mathbf{Y}_{m,n} = \begin{bmatrix} Y_{m,n}(0) & 0 & 0 & \dots & 0 \\ 0 & Y_{m,n}(\omega_p) & 0 & \dots & 0 \\ 0 & 0 & Y_{m,n}(2\omega_p) & \dots & 0 \\ \vdots & \vdots & \vdots & \ddots & \vdots \\ 0 & 0 & 0 & \dots & Y_{m,n}(K\omega_p) \end{bmatrix} \tag{2.9}$$

where $Y_{m,n}(k\omega_p)$ is the admittance between ports m and n at $\omega = k\omega_p$. While this is the complete matrix for the linear subcircuit, it would be better to absorb the source ports and be left with an $N \times N$ matrix. This can be done by modifying the network diagram of Figure 2.3 to that of Figure 2.4. This format removes the source and load ports and adds an effective current source at each of the ports. The resulting current at each of the ports is

then

$$\begin{bmatrix} \mathbf{I}_{LIN;1} \\ \mathbf{I}_{LIN;2} \\ \mathbf{I}_{LIN;3} \\ \vdots \\ \mathbf{I}_{LIN;N} \end{bmatrix} = \begin{bmatrix} \mathbf{Y}_{1,N+1} & \mathbf{Y}_{1,N+2} \\ \mathbf{Y}_{2,N+1} & \mathbf{Y}_{2,N+2} \\ \mathbf{Y}_{3,N+1} & \mathbf{Y}_{3,N+2} \\ \vdots & \vdots \\ \mathbf{Y}_{N,N+1} & \mathbf{Y}_{N,N+2} \end{bmatrix} \begin{bmatrix} \mathbf{V}_{N+1} \\ \mathbf{V}_{N+2} \end{bmatrix} + \begin{bmatrix} \mathbf{Y}_{1,1} & \mathbf{Y}_{1,2} & \dots & \mathbf{Y}_{1,N} \\ \mathbf{Y}_{2,1} & \mathbf{Y}_{2,2} & \dots & \mathbf{Y}_{2,N} \\ \mathbf{Y}_{3,1} & \mathbf{Y}_{3,2} & \dots & \mathbf{Y}_{3,N} \\ \vdots & \vdots & \ddots & \vdots \\ \mathbf{Y}_{N,1} & \mathbf{Y}_{N,2} & \dots & \mathbf{Y}_{N,N} \end{bmatrix} \begin{bmatrix} \mathbf{V}_1 \\ \mathbf{V}_2 \\ \mathbf{V}_3 \\ \vdots \\ \mathbf{V}_N \end{bmatrix} \tag{2.10}$$

and in vector form

$$\underline{\mathbf{I}}_{LIN} = \underline{\mathbf{Y}}_s \underline{\mathbf{V}}_s + \underline{\mathbf{Y}}_{N\times N} \underline{\mathbf{V}} = \underline{\mathbf{I}}_s + \underline{\mathbf{I}}_l \tag{2.11}$$

where $\underline{\mathbf{I}}_{LIN}$ is the total current from the linear subcircuit from (2.7), $\underline{\mathbf{I}}_s$ is the current contribution from the voltage source, $\underline{\mathbf{I}}_l$ is the current contribution from the linear Y-matrix, $\underline{\mathbf{Y}}_s$ and $\underline{\mathbf{Y}}_{N\times N}$ are the portions of the linear Y-matrix as shown in (2.10), $\underline{\mathbf{V}}_s$ is the source voltages, and $\underline{\mathbf{V}}$ is the voltage guess for each harmonic on each port.

For the nodal method, the same steps can be accomplished with nodal admittance parameters [51]. While constructed differently, the result is nearly identical to the network admittance parameters, but produce nodal currents from an input of nodal voltages.

While the linear subcircuit could be completely analyzed in the frequency domain from the guessed voltage, the harmonic balance method analyzes the nonlinear subcircuit in the time domain and then converts it back to the frequency domain. This requires an equation of current as a function of voltage in the time domain to be known before harmonic balance begins. In order to obtain the time-domain guessed voltages, an inverse Fourier transform is needed as in

$$v_n(t) = \mathscr{F}^{-1}\{\mathbf{V}_n\} \tag{2.12}$$

where $v_n(t)$ is the time-domain voltage guess and $\mathbf{V}_n$ is the frequency-domain voltage

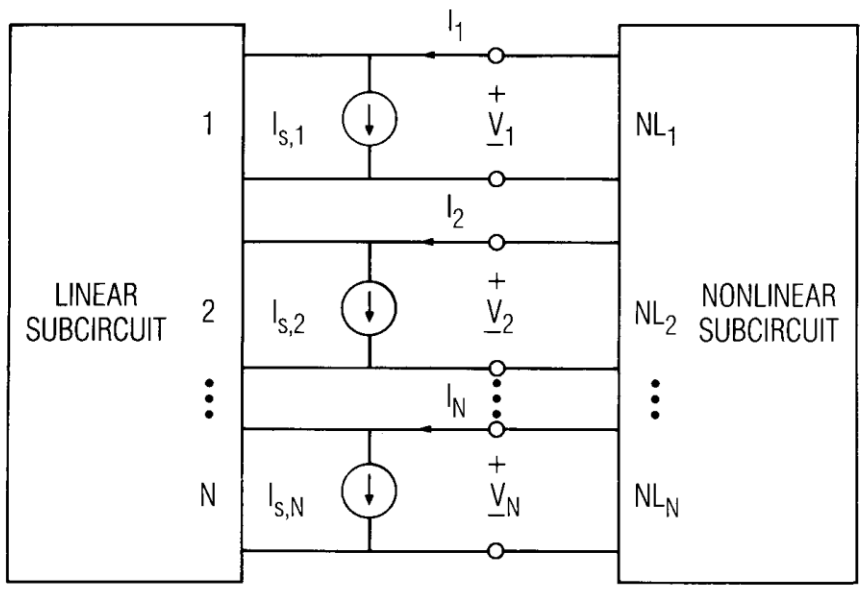

Figure 2.4: Circuit divided into linear and nonlinear subcircuits with N ports connecting them. The source/load ports have been absorbed into the linear subcircuit so a current source appears at each port [26].

guess at the n-th node. The time-domain current is then obtained by the predetermined equation

$$i_{nl;n}(t) = f_n(v_1(t), v_2(t), v_3(t), ..., v_N(t)) \tag{2.13}$$

where $f_n(v_1(t), ..., v_N(t))$ is the function that calculates the nonlinear current $i_{nl;n}(t)$ of the n-th node from the guessed voltages at each of the ports. This equation must be known prior to the harmonic balance method. A Fourier transform converts the current back into the frequency domain as in

$$\mathbf{I}_{nl;n} = \mathscr{F}\{i_{nl;n}(t)\} \tag{2.14}$$

where $\mathbf{I}_{nl;n}$ is the nonlinear current at the n-th node in the frequency domain as calculated from the predetermined equation.

If a nonlinear capacitor is in the circuit, a slightly different method can be used to calculate the resulting nonlinear current from the voltage guess. Because current is the

time derivative of charge ($i(t) = \delta q/\delta t$), the predetermined equation can be altered to solve for charge instead and then taken immediately into the frequency domain as in

$$\mathbf{Q}_n = \mathscr{F}\{q_n(t)\} = \mathscr{F}\{f_{qn}(v_1(t), v_2(t), v_3(t), ..., v_N(t))\} \tag{2.15}$$

where $q_n(t)$ is the time-domain capacitor charge and $\mathbf{Q}_n$ is the frequency-domain capacitor charge at the n-th node. The nonlinear capacitor current $\underline{\mathbf{I}}_c$ can then be calculated from $\mathbf{Q}_n$ by

$$\underline{\mathbf{I}}_c = \mathrm{j}\underline{\mathbf{\Omega}}\underline{\mathbf{Q}} \tag{2.16}$$

where j is the imaginary number, $\underline{\mathbf{Q}}$ is of the same format as (2.6), and $\underline{\mathbf{\Omega}}$ is a diagonal matrix of the form

$$\underline{\mathbf{\Omega}} = \begin{bmatrix} 0 & 0 & 0 & \dots & \dots & \dots & \dots & \dots & 0 \\ 0 & \omega_p & 0 & \dots & \dots & \dots & \dots & \dots & 0 \\ 0 & 0 & 2\omega_p & \dots & \dots & \dots & \dots & \dots & 0 \\ \vdots & \ddots & \ddots & \ddots & \ddots & \ddots & \ddots & \ddots & \vdots \\ 0 & \dots & \dots & \dots & K\omega_p & 0 & 0 & \dots & 0 \\ 0 & \dots & \dots & \dots & 0 & 0 & 0 & \dots & 0 \\ 0 & \dots & \dots & \dots & 0 & 0 & \omega_p & \dots & 0 \\ \vdots & \ddots & \ddots & \ddots & \ddots & \ddots & \ddots & \ddots & \vdots \\ 0 & \dots & \dots & \dots & \dots & \dots & \dots & \dots & K\omega_p \end{bmatrix} \tag{2.17}$$

where ω_p is the fundamental frequency. This $N(K+1) \times N(K+1)$ matrix has N cycles of each harmonic to be solved for. Combining (2.14) and (2.16) results in

$$\underline{\mathbf{I}}_{NL} = \underline{\mathbf{I}}_{nl} + \underline{\mathbf{I}}_c \,. \tag{2.18}$$

Finally, by combining (2.7), (2.11), and (2.18), a complete form of the error equation can be shown as

$$\underline{\epsilon} = \underline{\mathbf{I}}_s + \underline{\mathbf{I}}_l + \underline{\mathbf{I}}_{nl} + \underline{\mathbf{I}}_c \tag{2.19}$$

where every term in the above equation is a function of the initial voltage guess $\underline{\mathbf{V}}$, and are of the same format as shown in (2.6). An optimization function can then be defined to minimize $\underline{\epsilon}$ as a function of $\underline{\mathbf{V}}$. This method was created in MATLAB for the examples in the next chapter and implements the `fsolve.m` function and uses the Trust-Region-Dogleg algorithm, which is a form of the Powell and Gauss-Newton methods, discussed further in Section 2.1.3.

2.1.2.2 Assumptions

Over the course of this derivation, a few fundamental assumptions are made about the solution set that should be highlighted. The method can only handle steady-state conditions and the solution is assumed to be a linear combination of a finite number of harmonic sinusoids, but the number can be large with modern optimization techniques.

The circuit itself is not limited in shape, as long as admittance parameters can be formed of the linear subnetworks with ports in meaningful locations. It additionally assumes that all inputs are harmonics of the base frequency, ω_p, but this can be overcome by using Large-Signal/Small-Signal analysis or multi-tone harmonic balance.

Finally, this method assumes that every component can either be absorbed into an admittance matrix or modeled with a time-domain equation describing the relationship between voltage and current. It normally cannot handle any switching or time-varying components, but it is possible with a slight modification discussed in the next chapter.

2.1.2.3 Historical Use and Typical Structures

Although classic harmonic balance is largely overshadowed by more useful transient solvers, the harmonic balance methods were still explored and further developed because they are able to solve some problems that are difficult in the time domain. Now it is one of the more common and widely applicable nonlinear solvers used. Piecewise and nodal harmonic balance specialize in circuits with distributed elements such as transmission lines and circuits utilizing subnetworks with network parameters. They are also particularly useful when multiple harmonic frequencies are used with large differences in their periods, though they could be non-harmonic with the use of multi-tone harmonic balance. Conversely, a time-domain solution would need a small step over a long range of time to solve the same problem. Both piecewise and nodal harmonic balance can be used in professional microwave circuit simulators such as Keysight's Advanced Design System (ADS), National Instruments' Microwave Office (AWR), Ansoft's Nexxim, Cadence Virtuoso Spectre, and Agilent's GoldenGate [52]–[55].

Piecewise harmonic balance is currently the most common form of harmonic balance simulating transistors [56], mixers [49], and amplifiers [57]. Nodal harmonic balance is not as common as the piecewise method, but has been more often used when there are a significant number of nonlinearities so that defining the system in terms of port admittance parameters become less useful than nodal admittance parameters, such as in MMICs [45], [58] or in noise analysis and power systems [59], [60].

2.1.3 Solvers

Previous sections have described the process of several versions of harmonic balance and how to set up the problem, while the actual calculation of the solutions was left to a minimization function of the user's choice. In this section, a couple of common solvers are

introduced before integrating harmonic balance into a larger system in the next section.

2.1.3.1 Parallel-Chord

For a real-valued, single-variable function f with a root at x^*, a linear approximation of f at x^0 can be created as

$$l(x) = \alpha(x - x^0) + f(x^0) \tag{2.20}$$

where x^0 is an initial guess of the root x^* and α is a suitable slope and $\alpha \neq 0$ [61]. A new approximation x^1 of the root x^* can be formed by solving for the root of the linear approximation as

$$x^1 = x^0 - \alpha^{-1} f(x^0) \tag{2.21}$$

and future approximations can be calculated with a constant α as

$$x^{k+1} = x^k - \alpha^{-1} f(x^k), \qquad k = 0, 1, \ldots . \tag{2.22}$$

This creates a series of approximations that gradually converge to the x^*, even with a constant α [61]. For a system of equations or a function with an equal number of inputs and outputs expressed in matrix form as

$$\Big[f(x_1, x_2, \ldots) \Big] = \mathbf{F}\mathbf{x}, \tag{2.23}$$

a linear approximation at $\mathbf{x}^k$ similar to (2.20) can be written as the affine transformation

$$\mathbf{L}\mathbf{x} = \mathbf{A}(\mathbf{x} - \mathbf{x}^k) + \mathbf{F}\mathbf{x}^k \tag{2.24}$$

where $\mathbf{L}$ is a strictly lower triangular matrix and $\mathbf{A}$ is a constant non-singular matrix that replaces α [61]. By setting $\mathbf{L}\mathbf{x} = 0$, the n-dimensional parallel-chord method can be

written as

$$\mathbf{x}^{k+1} = \mathbf{x}^k - \mathbf{A}^{-1}\mathbf{F}\mathbf{x}^k, \qquad k = 0, 1, \ldots . \tag{2.25}$$

The crux of the problem now lies in defining the matrix $\mathbf{A}$. The primary requirement for $\mathbf{A}$ is that (2.25) be locally convergent. In other words, it is required that for $\mathbf{x}^0$ close to $\mathbf{x}^*$, then $\lim_{k\to\infty} \mathbf{x}^k = \mathbf{x}^*$. One simple solution is $\mathbf{A} = \alpha\mathbf{I}$ [61].

2.1.3.2 Newton

The Newton method uses the same process as the previous parallel-chord method, but selects α and $\mathbf{A}$ as a derivative of f or $\mathbf{F}$ [61]. In the simplified Newton method for 1-dimensional functions, the derivative of the initial guess x^0 is chosen as α so that

$$x^{k+1} = x^k - f'(x^0)^{-1} f(x^k), \qquad k = 0, 1, \ldots \tag{2.26}$$

where $f'(x)$ is the derivative of the function f at x. This can be expanded to an n-dimensional function F using the Gateaux derivative $\mathbf{F}'(\mathbf{x})$ as in

$$\mathbf{x}^{k+1} = \mathbf{x}^k - \mathbf{F}'(\mathbf{x}^0)^{-1}\mathbf{F}\mathbf{x}^k, \qquad k = 0, 1, \ldots . \tag{2.27}$$

These equations allow for convergence on the root of the function f or $\mathbf{F}$ with an intelligent, but constant slopes α or $\mathbf{A}$ [61].

The simplified Newton method depends heavily on a good initial guess x^0 to rapid computation and convergence, but a better alternative would allow the slopes α and $\mathbf{A}$ to change with each step of the iteration. This would allow the simulation to adjust as subsequent values of x^k converged to a solution. Modifying (2.22) and (2.25) to include

changing slopes become

$$x^{k+1} = x^k - f'(x^k)^{-1} f(x^k), \qquad k = 0, 1, ... \tag{2.28}$$

and

$$\mathbf{x}^{k+1} = \mathbf{x}^k - \mathbf{F}'(\mathbf{x}^k)^{-1} \mathbf{F}\mathbf{x}^k, \qquad k = 0, 1, ... \tag{2.29}$$

which is more likely to converge, and is known as the Newton method. Note that now the derivative of an n-dimensional system must be calculated for each step.

Block Newton A modified form of the Newton method, called the block Newton method [29], partitions the function matrix $\mathbf{F}$ into sub-matrices to make the computation more efficient. Specifically for harmonic balance, the system matrices are split by harmonic, enabling the solver to minimize each harmonic in the system simultaneously instead of evaluating the entire system as a unit. This allows for a faster and more accurate convergence [29].

2.2 Combining with MoM

Harmonic balance has now been established as a versatile solver for nonlinear circuits, but it has yet to be shown to solve nonlinear electromagnetic structures of arbitrary shape and excitation. Because of the hybrid nature of harmonic balance and the separation between the linear and nonlinear sub-circuits, a pre-existing linear solver can be used as a base model and develop the linear structure that is loaded with nonlinear components.

MoM is a full electromagnetic solver that uses basis functions to produce an impedance matrix of an arbitrary structure, making integration with harmonic balance straightforward. Additionally, the modal nature of MoM makes it useful in applications of modal current analysis and fundamental bounds. For these reasons, MoM was chosen as the method to

model an arbitrary LTI structure as the linear sub-circuit of harmonic balance.

2.2.1 Partition the Matrix

Referring back to Section 2.1.2, there are three portions of a nonlinear-loaded electromagnetic structure or antenna: nonlinear load, linear loaded, and linear unloaded/driven. The method described here uses harmonic balance to balance the currents from these three sections using the equation

$$\underline{\epsilon} = \underline{\mathbf{I}}_{NL} + \underline{\mathbf{I}}_{LL} + \underline{\mathbf{I}}_{LU} \tag{2.30}$$

where $\underline{\mathbf{I}}_{NL}$, $\underline{\mathbf{I}}_{LL}$, and $\underline{\mathbf{I}}_{LU}$ refer to the currents at the nonlinear loads due to voltages on the nonlinear loads, the linear loaded sections, and the linear unloaded/driven sections. Note that MoM produces an impedance matrix, while the harmonic balance method described here uses the admittance matrix. This can be obtained through a simple inversion as

$$\mathbf{Y} = \mathbf{Z}^{-1}. \tag{2.31}$$

The nonlinear load is handled the same way as in the previous versions of harmonic balance. An equation must be predetermined to represent the relationship between voltage and current, such as in (2.13), reproduced below as

$$i_{nl;n}(t) = f_n(v_1(t), v_2(t), v_3(t), ..., v_N(t)) \tag{2.32}$$

where $f_n(v_1(t), ..., v_N(t))$ is the function that calculates the nonlinear current $i_{nl;n}(t)$ of the n-th node from the guessed voltages at each of the ports. A Fourier transform converts the current back into the frequency domain for harmonic balance analysis as in (2.14) to produce $\underline{\mathbf{I}}_{NL}$.

The linear, loaded section corresponds to the portion of the electromagnetic structure

where the nonlinear load is applied, represented by $\underline{\mathbf{Y}}_{LL,LL}$, similar to $\underline{\mathbf{Y}}_{N\times N}$ in (2.11). Note that this is not a reduced matrix, but a specific partition that relates the current at the nonlinear loads generated by a voltage at those locations due to the LTI structure, as shown in (2.10). The resulting current, $\underline{\mathbf{I}}_{LL}$, is then calculated with

$$\underline{\mathbf{I}}_{LL} = \underline{\mathbf{Y}}_{LL,LL}\underline{\mathbf{V}} \tag{2.33}$$

where $\underline{\mathbf{V}}$ is the voltage vector used as the independent variable in the harmonic balance optimization.

The linear, unloaded section handles the effect the rest of the linear structure has on the loaded sections. This includes any excitation that may be present on the structure, either as a lumped voltage source or a plane wave. Similar to the external source matrix $\underline{\mathbf{Y}}_s$ in (2.11), the submatrix $\underline{\mathbf{Y}}_{LL,LU}$ can be used to calculate the current at the linear loaded locations from the rest of the structure. This is accomplished with

$$\underline{\mathbf{I}}_{LU} = \underline{\mathbf{Y}}_{LL,LU}\underline{\mathbf{V}}_{LU} \tag{2.34}$$

where $\underline{\mathbf{V}}_{LU}$ is the voltage vector corresponding to the excitation of the linear unloaded portion of the structure independent of the nonlinear loading.

Once each of the sections of the electromagnetic structure are defined, (2.30) can be minimized over the independent variable $\underline{\mathbf{V}}$ to balance the harmonics of the system.

2.2.2 Equivalent Source Model

The analysis discussed in Sections 2.1.2 and 2.2 solve electromagnetic circuits and structures with nonlinear loading. Specifically, the harmonic balance method solves for the voltages and currents on the nonlinear loading, but often the voltages and currents over the

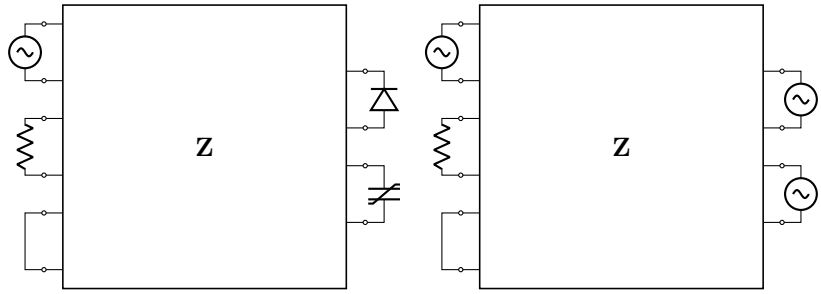

(a) Network composed of two subcircuits

(b) Network composed of two subcircuits

Figure 2.5: Equivalent source model using the solved voltages at the nonlinear loads as additional voltage sources at the harmonic frequencies.

entire structure are needed for complex electromagnetic analysis. When combined with MoM this can be easily done using the MoM matrix of the full linear system by using the results from harmonic balance analysis as equivalent voltage sources, as in Figure 2.5.

From the previous sections, there are two voltage vectors: the linear unloaded voltage $\underline{\mathbf{V}}_{LU}$ and the independent variable used in the harmonic balance $\underline{\mathbf{V}}$. Concatenating the two voltages into a single vector allows it to be used with the full MoM admittance matrix as in

$$\begin{bmatrix} \underline{\mathbf{I}}_{LL} \\ \underline{\mathbf{I}}_{LU} \end{bmatrix} = \begin{bmatrix} \underline{\mathbf{Y}}_{LL,LL} & \underline{\mathbf{Y}}_{LL,LU} \\ \underline{\mathbf{Y}}_{LU,LL} & \underline{\mathbf{Y}}_{LU,LU} \end{bmatrix} \begin{bmatrix} \underline{\mathbf{V}} \\ \underline{\mathbf{V}}_{LU} \end{bmatrix} \tag{2.35}$$

where $\underline{\mathbf{Y}}_{LL,LL}$ and $\underline{\mathbf{Y}}_{LL,LU}$ are the partitioned matrices from (2.33) and (2.34), $\underline{\mathbf{Y}}_{LU,LL}$ and $\underline{\mathbf{Y}}_{LU,LU}$ fill out the rest of the MoM admittance matrix, and $\underline{\mathbf{I}}_{LL}$ and $\underline{\mathbf{I}}_{LU}$ are the currents of the linear loaded and linear unloaded sections.

2.3 Examples

In this section, several different kinds of circuits are analyzed using harmonic balance. For every example, harmonic balance code created by the author is compared to the harmonic

balance solver in Microwave Office (AWR). For each configuration, the voltage and current through the nonlinear device is a function of time for two periods of the input. The impedance of the device is calculated by dividing the voltage and current and can be used for Large-Signal/Small-Signal analysis with conversion matrices. The first 128 harmonics are calculated for each example and is also shown, as well as a plot with just the first 10 shown to make it easier to compare magnitudes. For the classic harmonic balance calculations, only the first 11 harmonics are calculated in the same amount of time (about 3 seconds) and a DFT is used to complete the plot of the other 117 harmonics.

2.3.1 Resistor, Inductor, and Capacitor Configurations

A circuit composed of resistors, inductors, and capacitors is a classic example to start with. Many more complicated devices can be analyzed with a combination of these three components, so being able to predict the response of the basics is useful. In this section, two different circuit configurations are considered: a series RC circuit and an RLC circuit. In each case, the capacitor is the only nonlinear component because it is more commonly nonlinear. Any of the other components could have been made nonlinear. A graphical representation of the difference between a linear capacitor and a nonlinear capacitor are shown in Figure 2.6.

2.3.1.1 RC Circuit

The first set of circuit examples have the simple RC circuit configuration shown in Figure 2.7. This basic circuit has one resistor set to 2 Ω and a capacitor which will be assumed to be linear or nonlinear in the following sections. AWR's harmonic balance solver is compared to the classic and piecewise harmonic balance methods as written by the author.

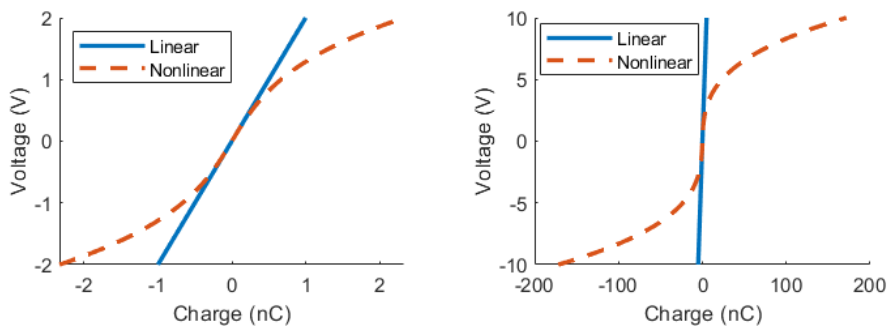

(a) Small Voltages (b) Large Voltages

Figure 2.6: Comparison of the charge-voltage relationship of linear and nonlinear capacitors.

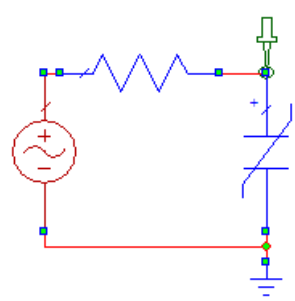

Figure 2.7: Circuit diagram of the series RC circuit. The voltage and current were measured at the node between the resistor and capacitor.

Linear Capacitor: This example simplifies the RC circuit further by assuming every component is linear, as in

$$Q = CV \tag{2.36}$$

where Q is the charge on the capacitor, V is the voltage across the capacitor, and C is the capacitance whose linear relationship is shown in Figure 2.6. The voltage source has an amplitude of 2 V at a frequency of 0.5 GHz and the capacitor has a capacitance of 500 pF. Figure 2.8 shows the resulting voltage and current across the capacitor and the time-domain impedance of the capacitor by dividing voltage and current. The harmonics of the voltage are also shown, and as expected only the first harmonic is significant. This example is shown mostly for comparison purposes and verification of the harmonic balance method.

Nonlinear Capacitor: When the capacitor is made nonlinear, the equations that govern it change slightly. From the traditional equation of $Q = CV$, the charge-voltage relationship is now modeled as

$$Q = C\left(V + \frac{1}{3}V^3\right) \tag{2.37}$$

which is shown in Figure 2.6 and will generate power in the third harmonic. This is a simple model for a nonlinear capacitor, with more complex forms have a higher order polynomial and weights on each indeterminate [26], [62]. Like the previous example, the voltage source has an amplitude of 2 V at a frequency of 0.5 GHz and the capacitor has a linear capacitance of 500 pF. The response of the nonlinear capacitor is shown in Figure 2.9. There is not much of a difference between this example and the linear capacitor, but there is a slight nonlinearity to the voltage and a slight increase in the third harmonic.

While this is a successful model of a nonlinear RC circuit, it is not very impressive as a nonlinear circuit. The next example increased the voltage to a 10 V peak while every other parameter remained the same. This pushed the capacitor further into the nonlinear region

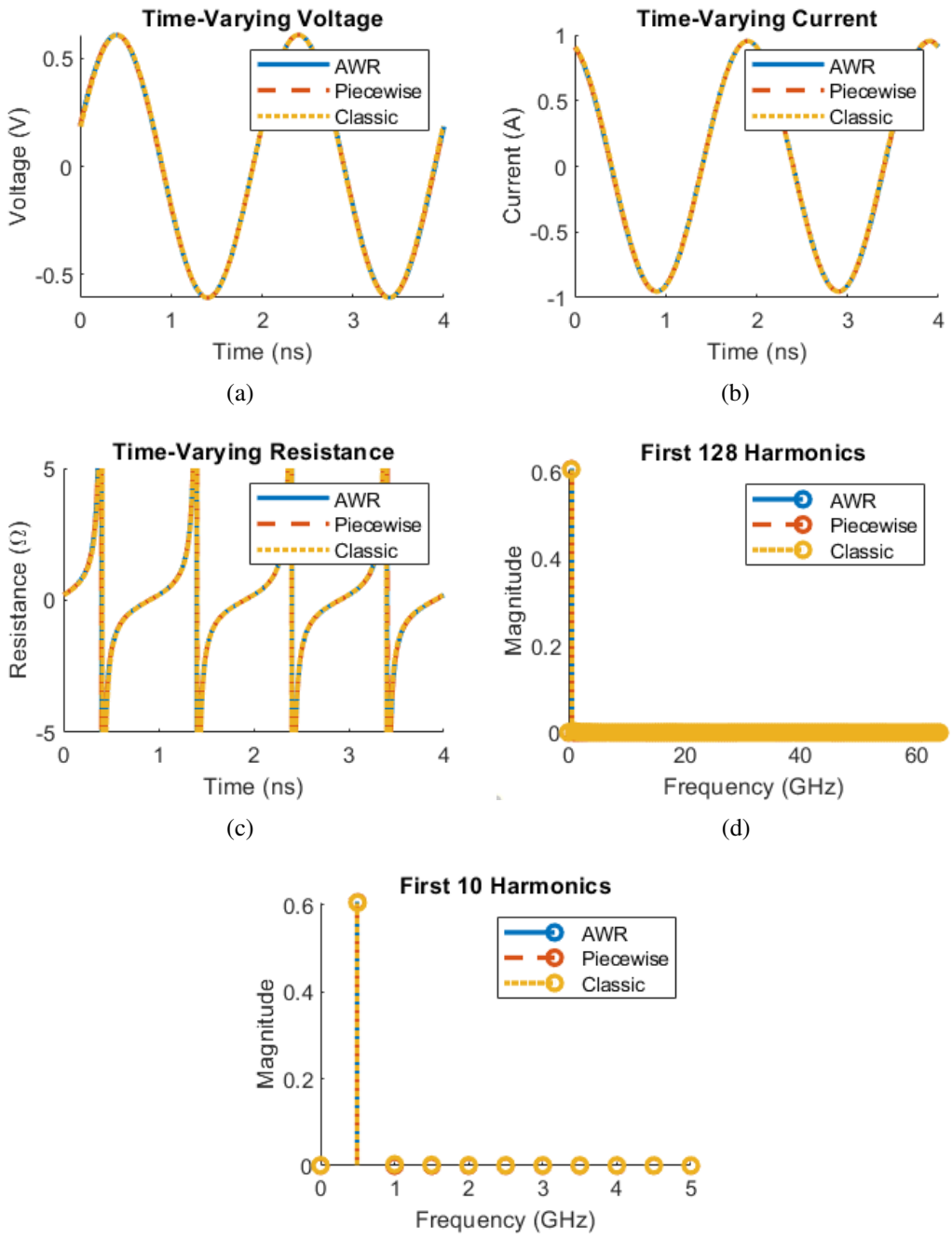

Figure 2.8: Response of a linear capacitor in an RC circuit where $R = 2\ \Omega$, $C = 500\ pF$, and the voltage source has an amplitude of 2 V at a frequency of 0.5 GHz.

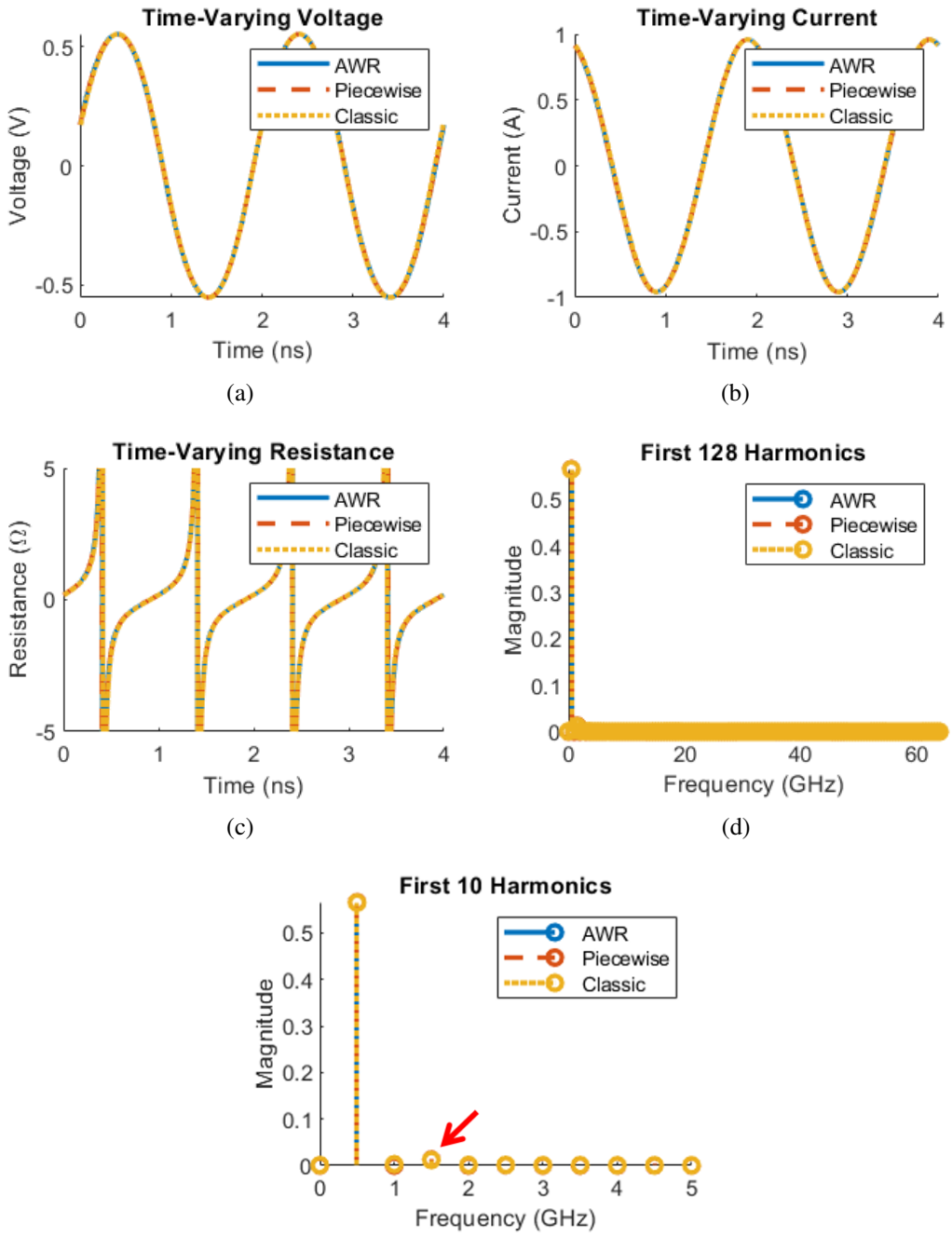

Figure 2.9: Response of a nonlinear capacitor in an RC circuit where $R = 2\ \Omega$, $C = 500\ pF$, and the voltage source has an amplitude of 2 V at a frequency of 0.5 GHz.

shown in Figure 2.6. The response of this capacitor is shown in Figure 2.10 the voltage is clearly more distorted and has a much larger third harmonic with even the fifth showing some significance.

2.3.1.2 RLC Circuit

The final example in this section is an LC tank resonator with series resistance, shown in Figure 2.11. At this point, the classic harmonic balance method was dropped as this example, and the later examples, are an invalid configuration for that model. Most of the circuit is the same as before, with a voltage amplitude of 10 V at a frequency of 0.5 GHz, a resistance of 2 Ω, and a capacitance of 500 pF. The added shunt inductor has an inductance of 0.15 nH, which makes the resonant frequency of the tank resonator around 0.58 GHz. The response of the capacitor in the circuit is shown in Figure 2.12. The current is more triangular than before and even more harmonics can be seen to have a slight significance.

2.3.2 Diodes and Switches

Moving on to more complex circuit components, diodes and switches challenge the harmonic balance method and push it toward the limits of what it can do. Diodes are very simple, but very nonlinear. Switches, on the other hand, are time-variant and not steady-state.

2.3.2.1 Diode

The ideal diode has an infinite impedance when reverse biased and a zero impedance when forward biased. This example uses a more realistic and more complex model of

$$I_d = I_0 \left(e^{\frac{eV}{kT}} - 1 \right) \tag{2.38}$$

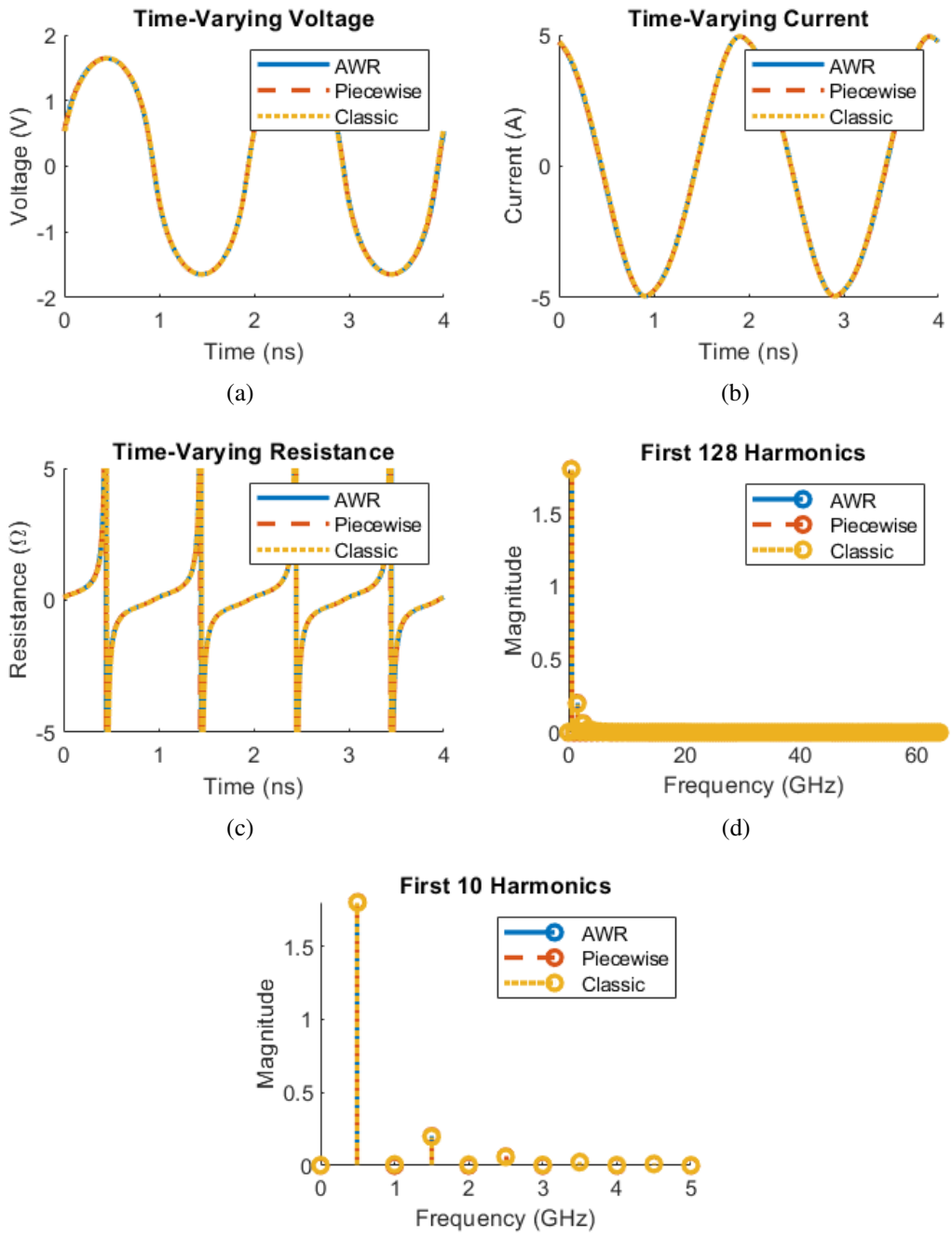

Figure 2.10: Response of a nonlinear capacitor in an RC circuit where $R = 2\ \Omega$, $C = 500\ pF$, and the voltage source has an amplitude of 10 V at a frequency of 0.5 GHz.

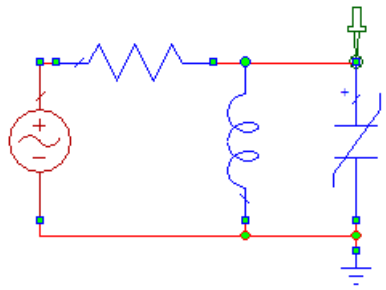

Figure 2.11: Circuit diagram of the tank LC circuit with a series resistance. The voltage and current were measured on the capacitor on the end near the resistor and inductor.

where I_d is the current through a diode, I_0 is the diode's saturation current, e is the charge of an electron, T is the temperature in Kelvin, k is Boltzmann's constant, and V is the voltage across the diode. This curve is shown in Figure 2.13

The circuit used is a very simple series resistor and diode configuration, shown in Figure 2.14. The diode is set to have a saturation current of 1 nA at a temperature of 295 K while the resistor had a resistance of 2 Ω. The response of the diode is shown in Figure 2.15. Now there is a DC component shown in the harmonics, but the higher harmonics die off much faster than in the nonlinear capacitor. Also, the discrepancy in the impedance between AWR and the piecewise method is because of some additional oscillations in the current of AWR that crossed zero. When the current rises again, the impedances agree.

2.3.2.2 Switch

Implementing a switch in harmonic balance was an interesting problem because harmonic balance is a steady-state nonlinear solver and switches are not steady-state. In AWR, it was accomplished with the transient solver and the `Switch_AP` component with nodes 3 and 4 connected to a pulse train that opens and closes the switch, shown in Figure 2.16, which is set to oscillate at 4 GHz. Both resistors have a resistance of 1 Ω and the voltage source has a 1 V peak magnitude at 0.5 GHz. The harmonic balance solver in AWR would not

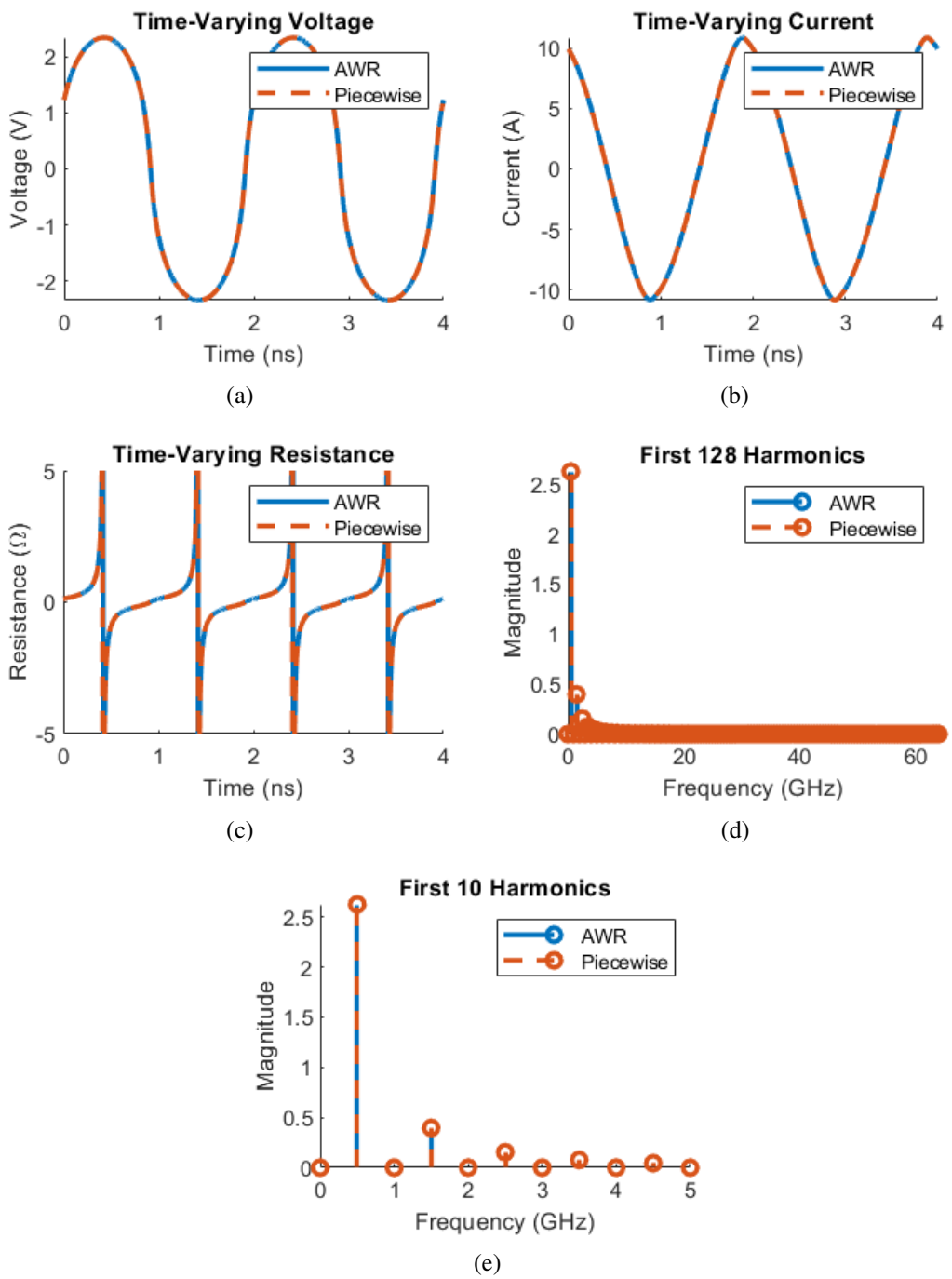

Figure 2.12: Response of a nonlinear capacitor in an RLC circuit where $R = 2\ \Omega$, $C = 500\ pF$, $L = 0.15\ nH$, and the voltage source has an amplitude of 10 V at a frequency of 0.5 GHz.

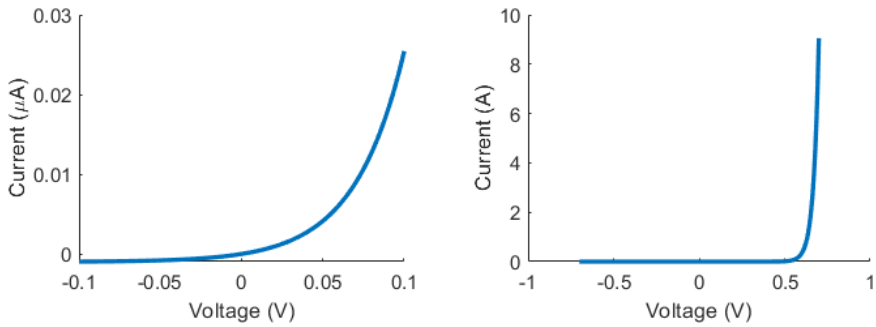

(a) Small Voltages (b) Large Voltages

Figure 2.13: The voltage-current relationship of a realistic diode shown at two different scales. Note that in (a), the current is in μA.

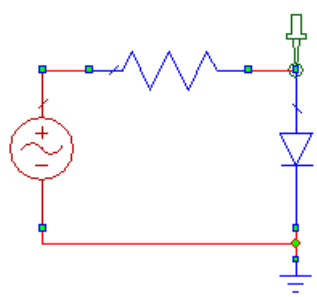

Figure 2.14: Circuit diagram of the series resistor and diode circuit. The voltage and current were measured at the node between the resistor and the diode.

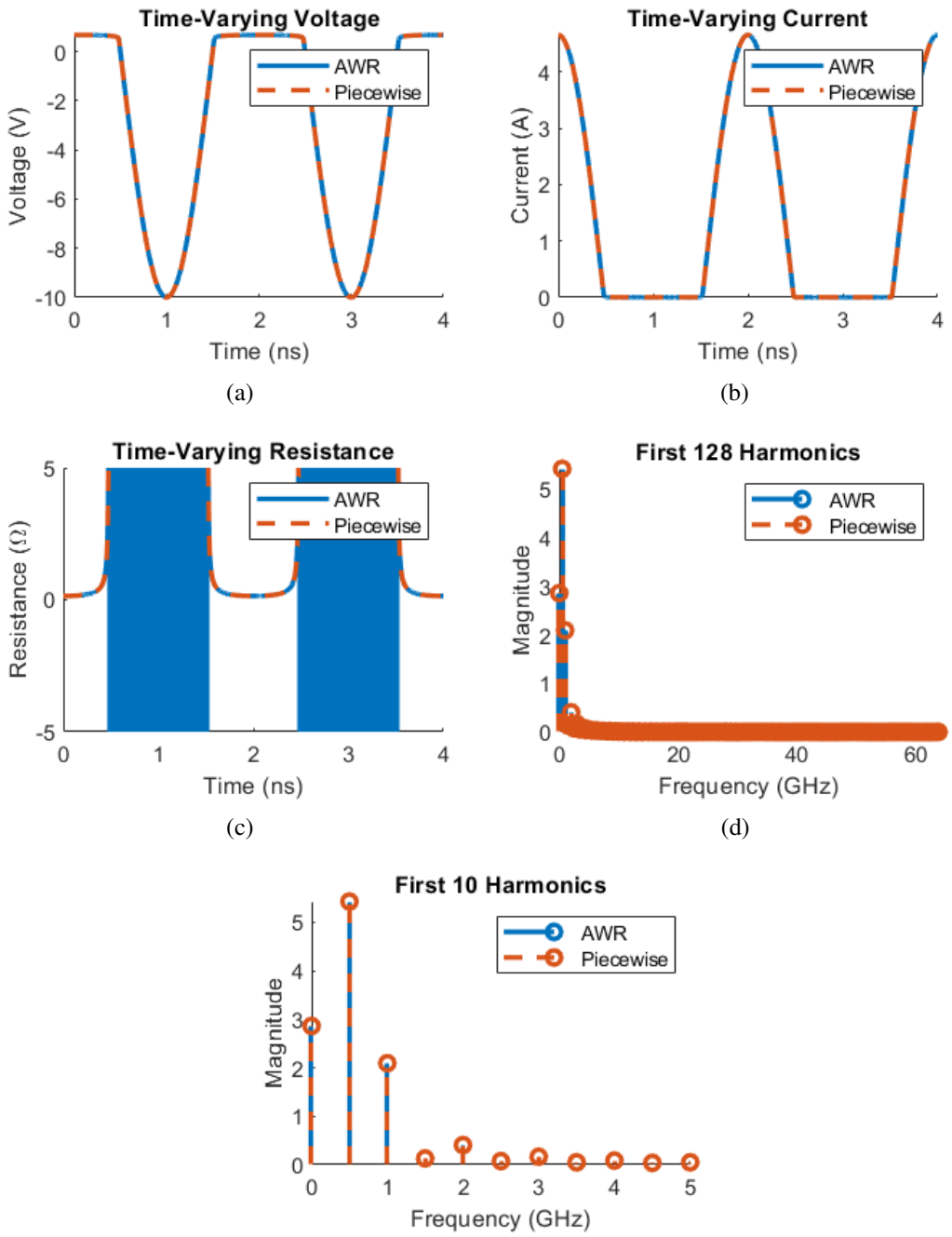

Figure 2.15: Response of a diode in series with a 2 Ω resistor and the voltage source has an amplitude of 10 V at a frequency of 0.5 GHz.

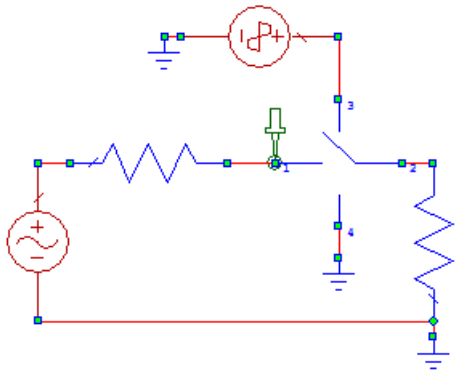

Figure 2.16: Circuit diagram of the series resistors and switch circuit. The voltage and current were measured at the node between the first resistor and the switch.

simulate the switch.

In the implementation of the piecewise harmonic balance method in MATLAB, the nonlinear circuit is analyzed using a function that maps voltage to current in the time domain, as described in Section 2.1.2. Because it is in the time domain that this takes place, it is possible to create a function that changes with time. The change over time must have a period that is harmonically related to the base frequency, but this modification allows harmonic balance to model switches that open and close periodically.

The response of the switch is shown in Figure 2.17. It is important to remember that this response was measured between the switch and the resistor next to the voltage source, which is why the impedance plot shows a 1 Ω resistance and the voltage only shows a 0.5 V drop at the peak. Also, shown in the impedance plot, note that the impedance approaches infinity when the switch opens.

2.3.3 Transistors

The final set of examples cover a MOSFET amplifier, shown in Figure 2.18, biased to different voltages to display linear and nonlinear behavior. The type of transistor amplifier used is a common-source amplifier and utilizes a voltage divider on the gate to control the

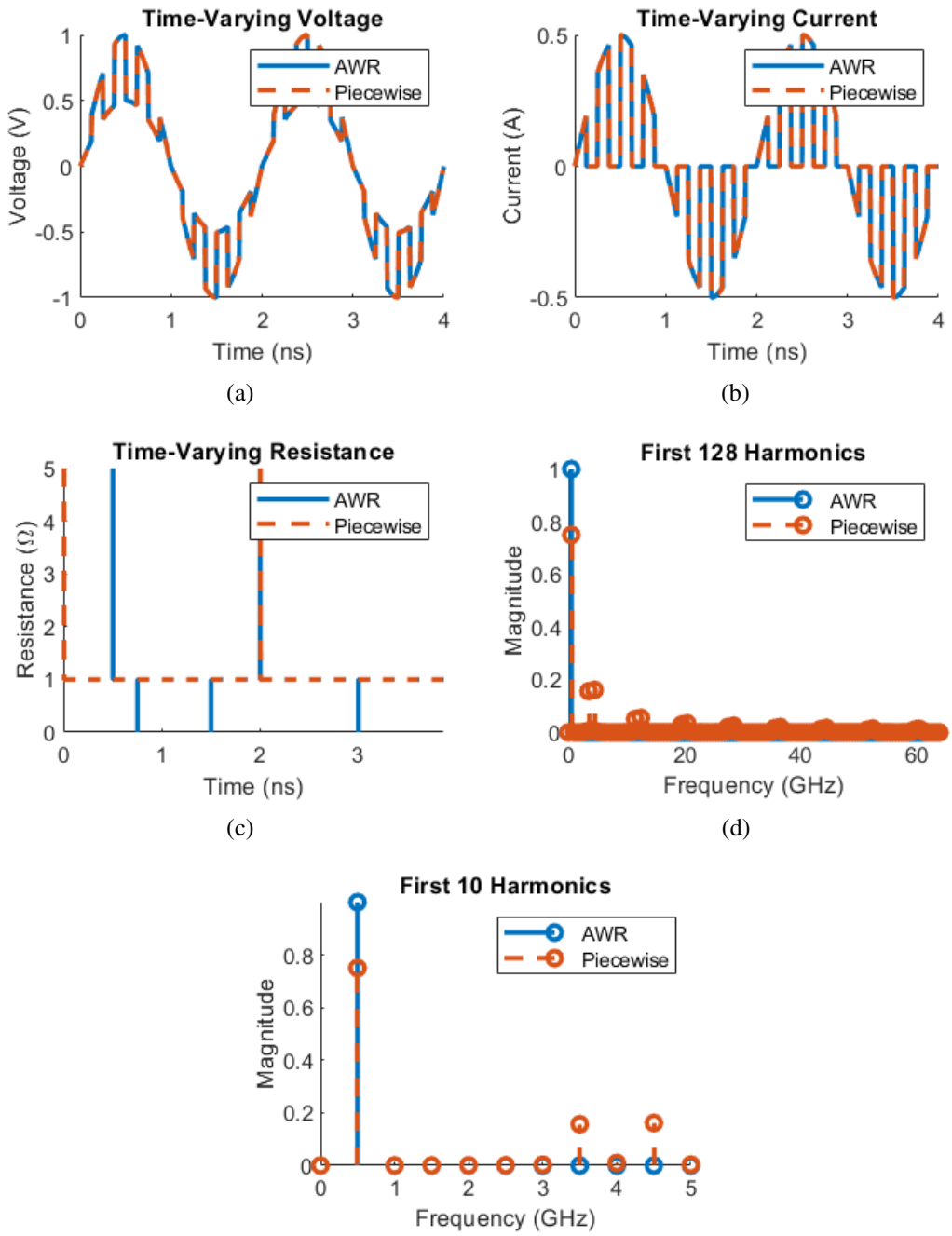

Figure 2.17: Response of a 4 GHz triggered switch in series with two resistors where $R = 1\ \Omega$ and the voltage source has an amplitude of 1 V at a frequency of 0.5 GHz.

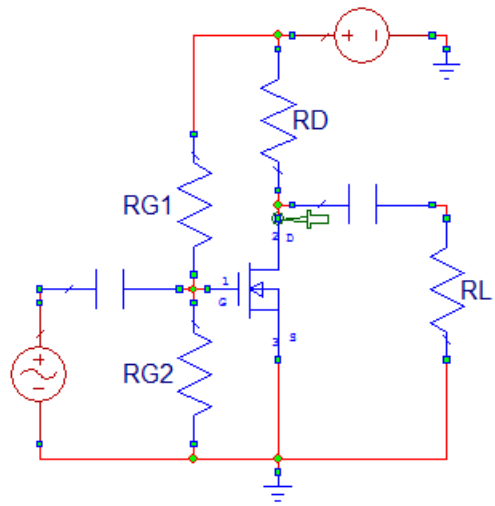

Figure 2.18: Common-source MOSFET amplifier with a biasing voltage divider. The voltage bias on the gate is controlled by changing the grounded gate resistor, $RG2$.

biasing. The magnitude of the current flowing through the MOSFET is directly proportional to the voltage at the gate, but it pulls current through a 10 kΩ resistor and a 15 V DC power source, making the output voltage an amplified signal with a 180° phase shift. The MOSFET has a 1.5 threshold voltage, a trans-conductance parameter of 0.25 mA/V^2, a channel length modulation parameter of 0.02 V^{-1}, and a load resistor of 10 kΩ. The DC biased MOSFET was then modulated with a 0.1 peak voltage source at 0.5 GHz, which was isolated from the DC circuit with 1 F capacitors. While Harmonic Balance works with the full circuit in Figure 2.18, the circuit can also be modeled with the small signal approximation but with added nonlinearities, shown in Figure 2.19. Both of these models will be analyzed when linearly and nonlinearly biased.

2.3.3.1 Linearly Biased Amplifier

The amplifier can be linearly biased by setting $RG1$ and $RG2$ to 10 MΩ and 3 MΩ, respectively. This biasing scheme results in a DC bias of 3.46 V at the gate and results in an almost linear response, as shown in Figure 2.20.

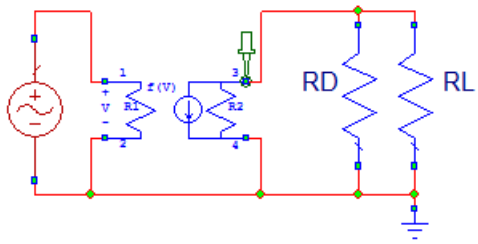

Figure 2.19: Small signal model of the amplifier shown in Figure 2.18. This model assumes no DC bias, but uses a current source that has the parameters of a biased transistor.

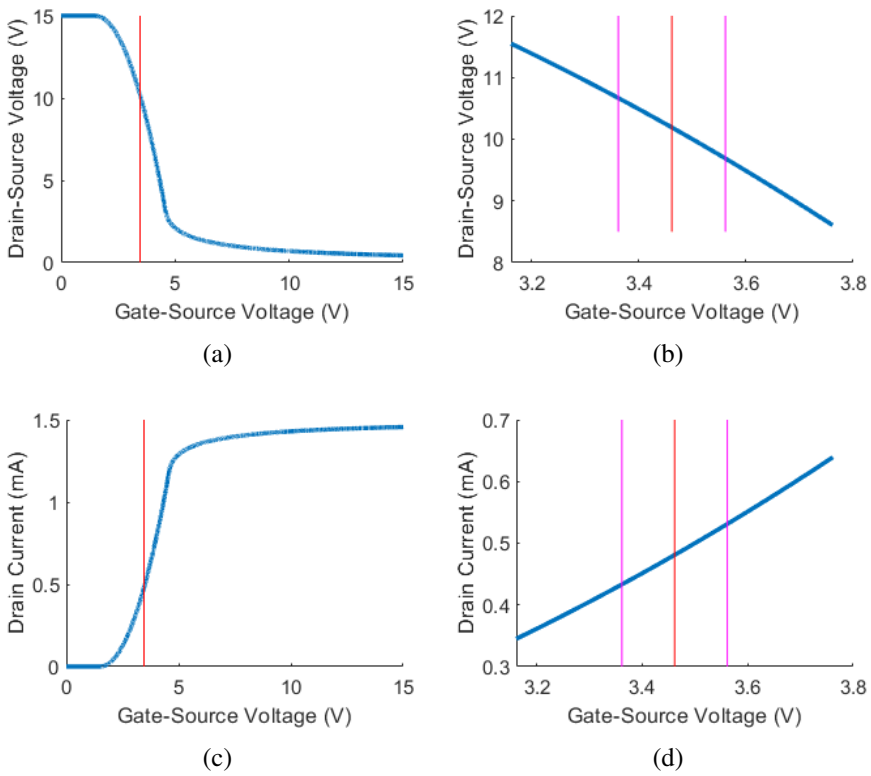

Figure 2.20: Drain current and voltage for given gate voltages. The vertical red line shows the bias voltage for linear operation at 3.46 V, and the two purple lines show the limits of the small signal modulation.

Full Circuit: The response of the linearly biased MOSFET is shown in Figure 2.21. This example is different from the others in that two input ports had to be implemented instead of just one. The current at the drain i_D pulled through a MOSFET in the saturation region is defined as

$$i_D = \frac{1}{2}k_n \left(v_{GS} - V_t\right)^2 \tag{2.39}$$

where k_n and V_t are the transconductance parameter and threshold voltage of the MOSFET respectively and v_{GS} is the DC biased, input sinusoidal voltage at the gate. The amplifier had a gain of about -2.45 V/V but has a large DC bias. This bias is removed on the other side of the 1 F capacitor, but the intent was to show the response of the MOSFET transistor. Additionally, the harmonics in Figure 2.21.d and 2.21.e are overshadowed by the DC component, but the amplitude of the 0.5 GHz components can still be seen.

Modified Small Signal Approximation: The small signal approximation can be useful to obtain a similar response to the full circuit, but without needing both input ports. This method usually assumes a linear response, but it can be modified to still include the non-linear effect from approaching the threshold voltage. With the linear approximation, the equation for the drain current is expanded to

$$i_D = \frac{1}{2}k_n \left(v_{GS} - V_t\right)^2 \tag{2.40}$$

$$= \frac{1}{2}k_n \left(V_{GS} + v_{gs} - V_t\right)^2 \tag{2.41}$$

$$= \frac{1}{2}k_n \left(V_{GS} - V_t\right)^2 + k_n \left(V_{GS} - V_t\right) v_{gs} + \frac{1}{2}k_n v_{gs}^2 \tag{2.42}$$

where V_{GS} is the DC bias between the gate and the source, v_{gs} is the high frequency input signal at the gate, and $v_{GS} = V_{GS} + v_{gs}$ [63]. The first term of (2.42) is the DC component, second is the linear component, and third is the nonlinear component. Usually in small

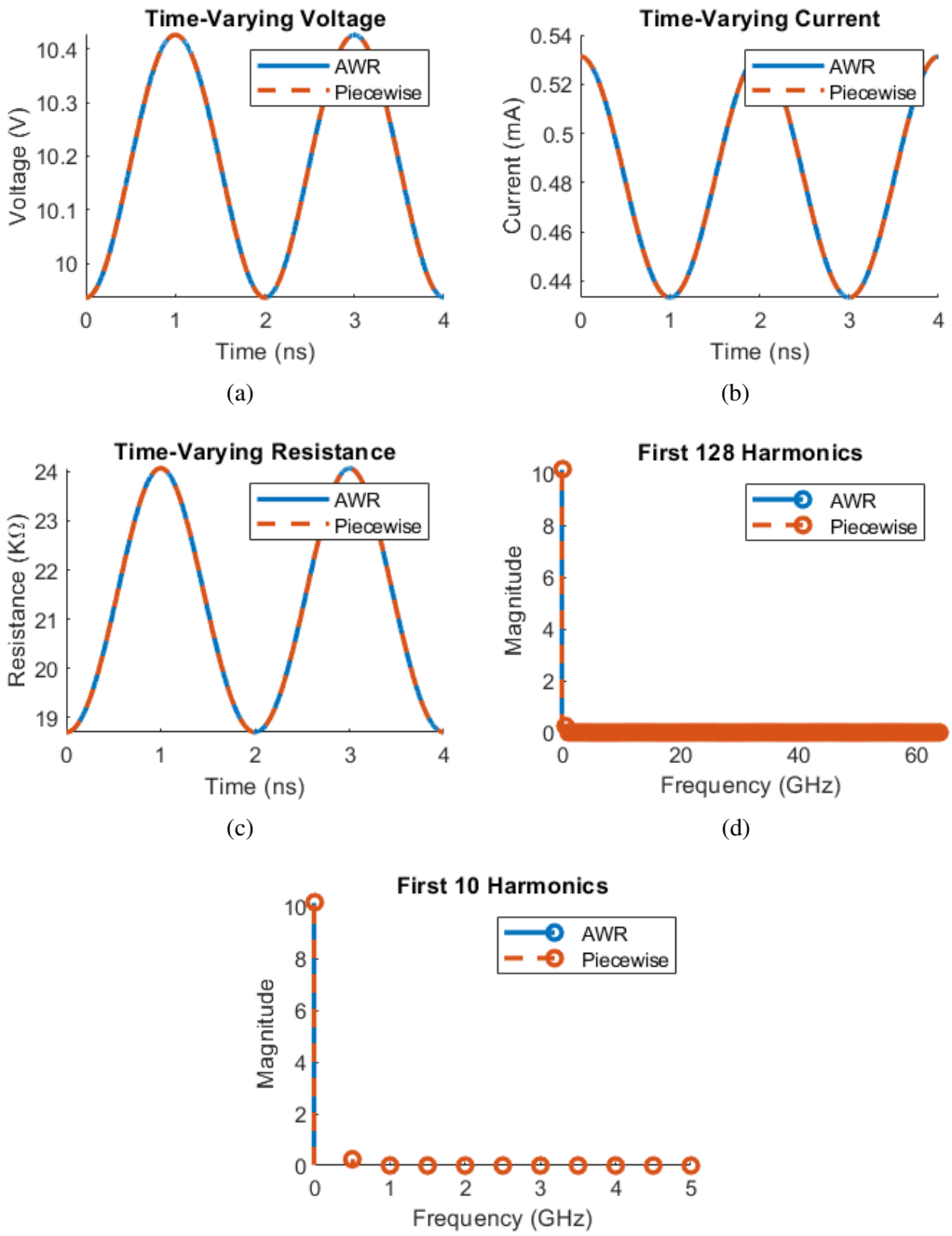

Figure 2.21: Response of a linearly biased MOSFET amplifier. The voltage was amplified by about 2.45 times to achieve a 0.245 V peak.

signal analysis, both the DC component and the nonlinear component are excluded, but here only the DC component will be removed. The response of the small signal model is shown in Figure 2.22. The response is very similar to that of the full circuit analysis, but with the DC offset already removed so the harmonics can be clearly seen.

2.3.3.2 Nonlinearly Biased Amplifier

The amplifier can be nonlinearly biased by setting $RG1$ and $RG2$ to 10 MΩ and 1.2 MΩ, respectively. This biasing scheme results in a DC bias of 1.61 V at the gate and the proximity to the threshold voltage of 1.5 V results in an almost very nonlinear response, as shown in Figure 2.23. Unfortunately, this biasing scheme also leads to a very small gain.

Full Circuit: The response of the nonlinearly biased MOSFET is shown in Figure 2.21. This example also has two ports to power and bias the circuit. The amplifier has a gain of about -0.13 V/V which is significantly smaller than the linear circuit. Again, the harmonics in Figure 2.24.d and 2.24.e are overshadowed by the DC component, and the amplitude of the 0.5 GHz components can barely be seen.

Modified Small Signal Approximation: The small signal approximation was used again to model the transistor. The nonlinear component is much stronger so it is easier to see that the small signal approximation is still valid for highly nonlinear biases. The response of the small signal model is shown in Figure 2.25. Again, the response is very similar to that of the full circuit analysis, but without the DC bias so the harmonics can be seen.

2.3.4 Diode-loaded Dipole Antenna

The previous examples show several cases of nonlinear loads and biasing schemes on simple circuits. In a similar way, an LTI antenna with nonlinear loads can be modeled by

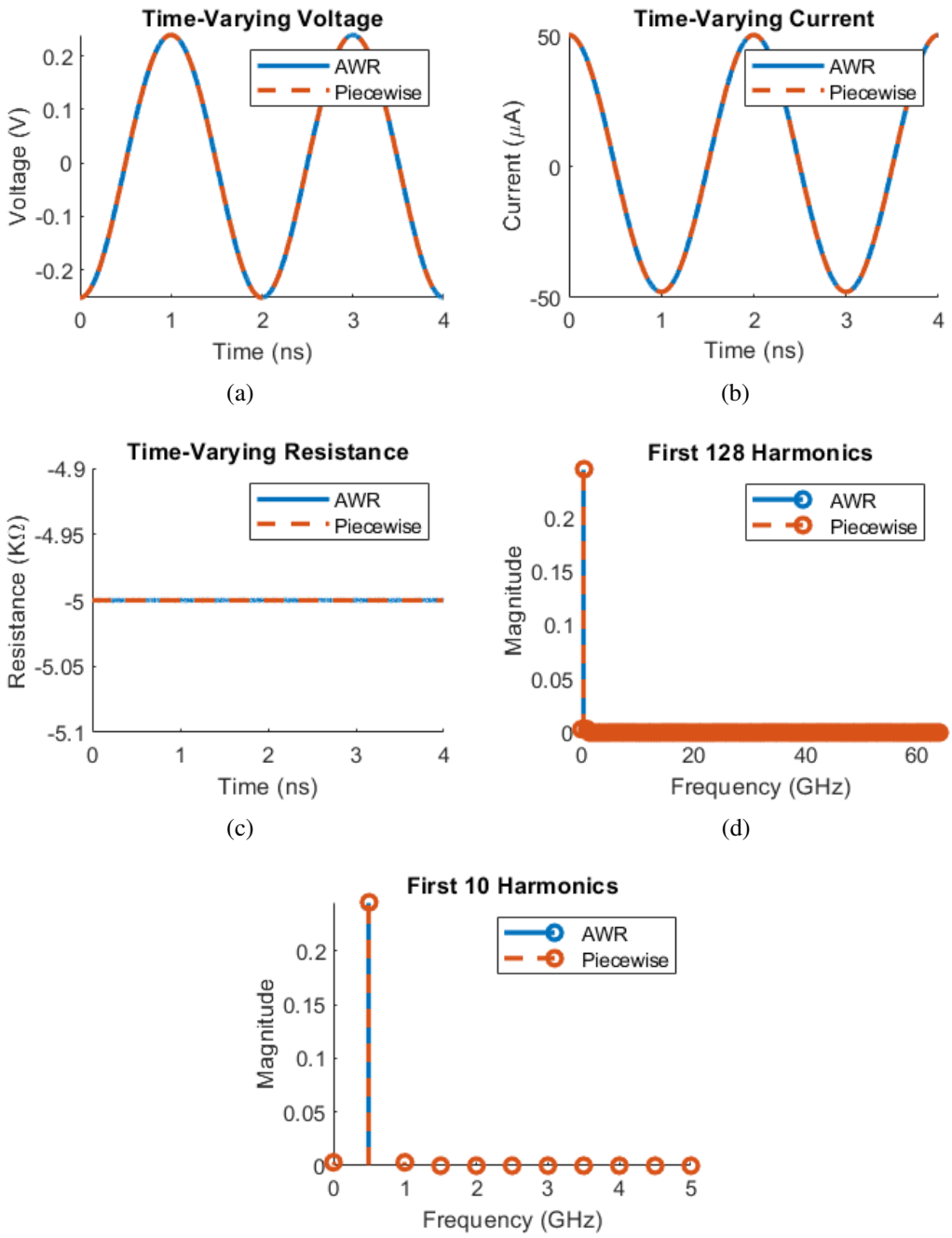

Figure 2.22: Response of a small signal model of the linearly biased MOSFET amplifier. The voltage was amplified by about 2.45 times to achieve a 0.245 V peak.

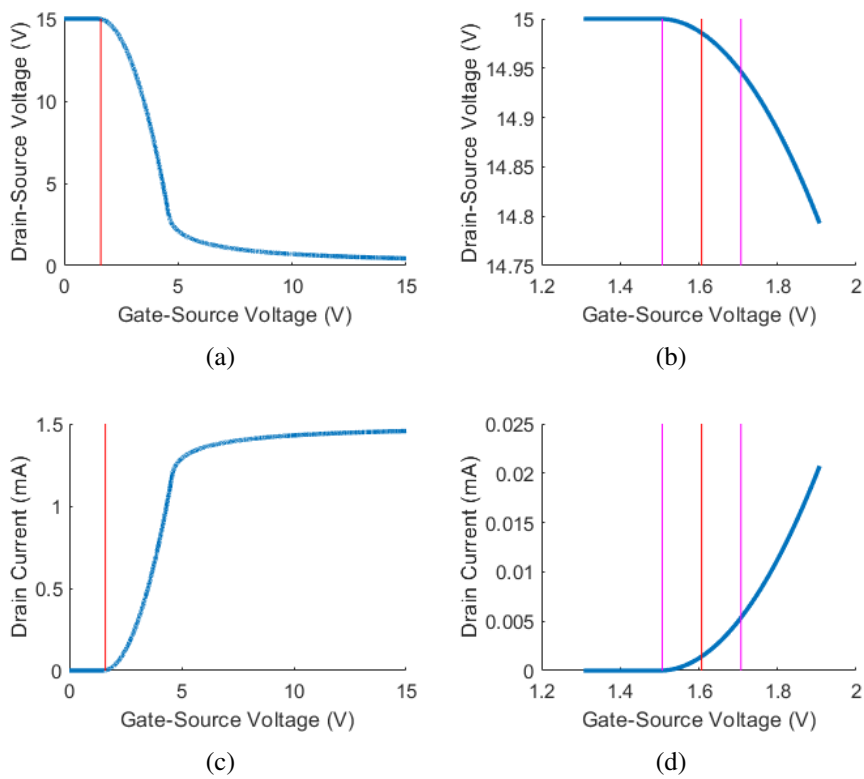

Figure 2.23: Drain current and voltage for given gate voltages. The vertical red line shows the bias voltage for nonlinear operation at 1.61 V, and the two purple lines show the limits of the small signal modulation.

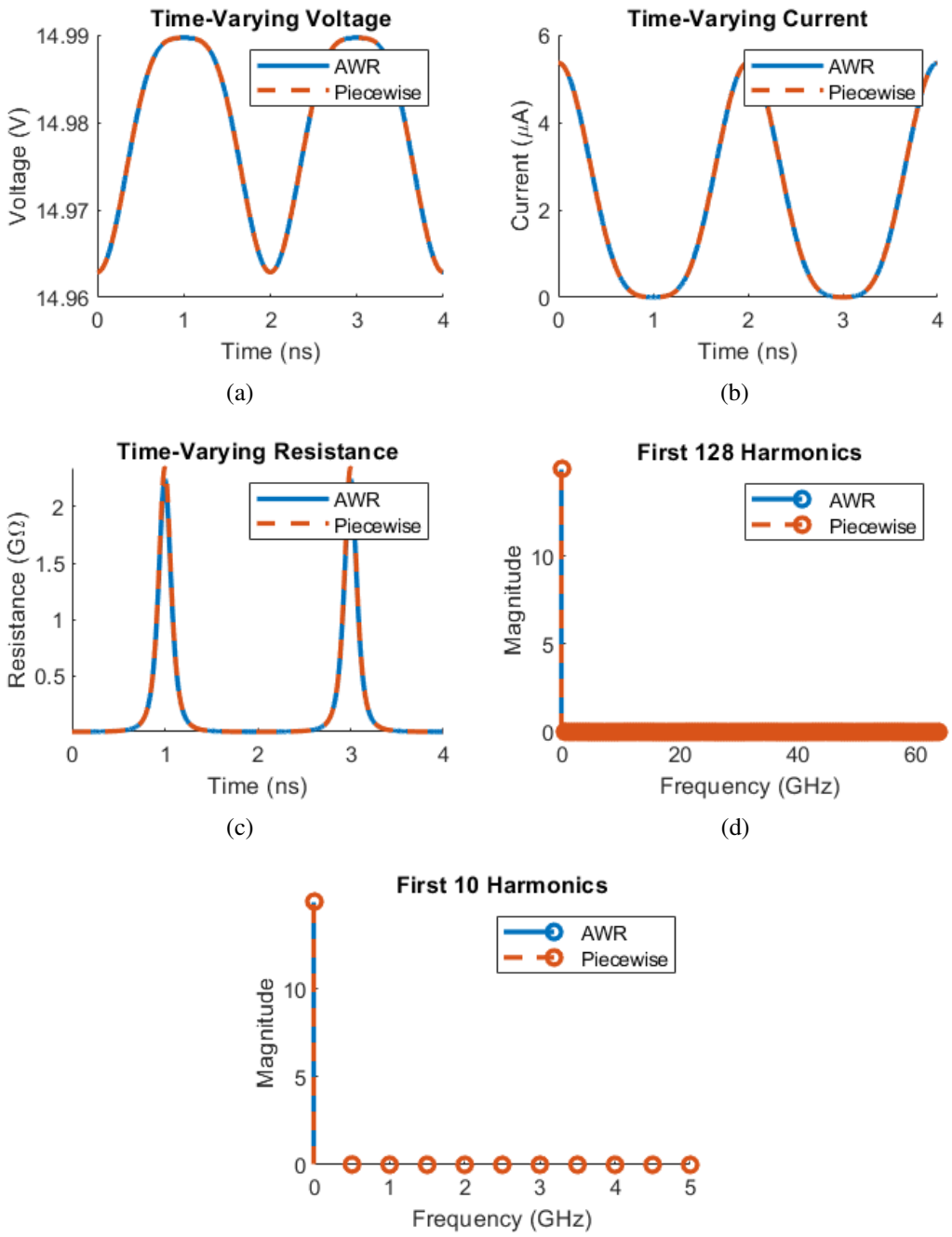

Figure 2.24: Response of a nonlinearly biased MOSFET amplifier. The voltage was amplified by about 0.13 times to achieve a 0.013 V peak.

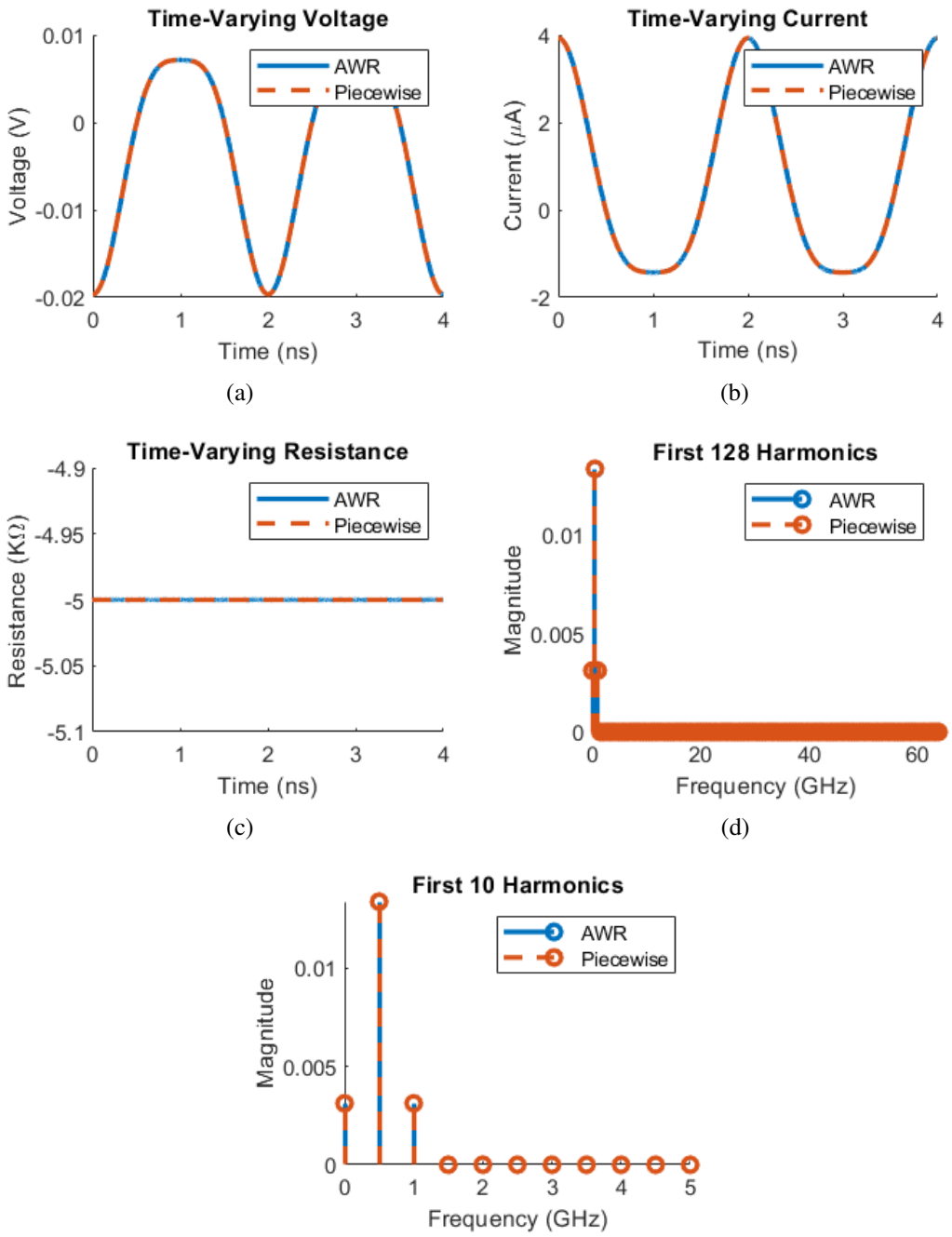

Figure 2.25: Response of a small signal model of the nonlinearly biased MOSFET amplifier. The voltage was amplified by about 0.13 times to achieve a 0.013 V peak.

expanding harmonic balance to a multiport LTI network, as in Section 2.2. For this example, a dipole with a length of 75 mm was loaded with a diode at its center and driven with a plane wave at 2 GHz.

The linear subcircuit consists of the unloaded dipole antenna and is modeled by MoM as an impedance/admittance matrix. The nonlinear subcircuit consists of the single diode load, equivalent to the diode used in Section 2.3.2.1 and evaluated in the time-domain. Using the harmonic balance method with MoM, the currents through the diode load and along the dipole are calculated and shown in Figure 2.26.a and 2.26.b. It can be seen that the time-domain current through the diode agrees with typical diode behavior, where the current is truncated in one direction and flows freely in the other. In Figure 2.26.c, the current on the dipole is used to calculate the total power radiated at each frequency and, in Figure 2.26.d, the backscatter pattern across the elevation angle θ for the first five radiated frequencies.

2.4 Limitations and Advantages

Over the course of the derivation and analysis, a few fundamental advantages and limitations were discussed previously. Here, they are highlighted and brought into a larger context. While the harmonic balance method is useful and can accurately simulate strongly nonlinear structures, defining the areas where the method can be most useful will help direct the path of future research.

2.4.1 Nonlinear Devices

Harmonic balance is an excellent solver for any nonlinear device. It circumvents the limitations of purely time- or frequency-domain solvers by merging them in a hybrid method, allowing for the integration of nonlinear components defined in the time domain with more

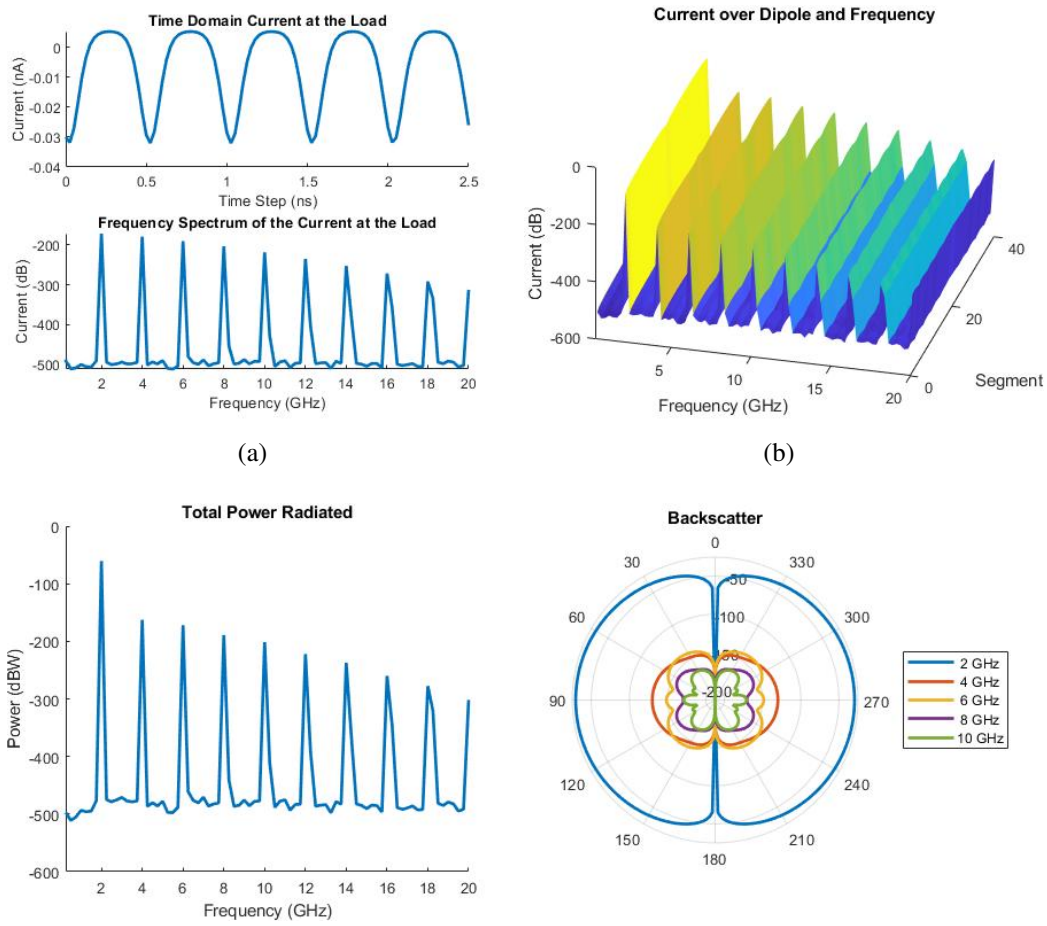

Figure 2.26: Current distribution and radiation characteristics for a 75 mm wire dipole loaded with a diode at its center. The time- and frequency domain current through the diode is shown in (a), and the current distribution across the dipole at each simulated frequency is shown in (b) in a logarithmic scale to show the magnitude at each harmonic. The total power radiated is shown in (c) with the backscatter pattern shown in (d).

conventional LTI devices that are more easily defined in the frequency domain. This gives the added advantage of using a time-domain relationship between voltage and current for the nonlinear component, which is easily obtained.

It is generally assumed in the harmonic balance method that the solution is steady-state and composed of a linear combination of sinusoids, which are multiples of a single base frequency, similar to the Fourier series assumptions. Generally, it is assumed that all inputs and excitations are also harmonics of the base frequency, but this an be overcome by using Large-Signal/Small-Signal analysis or multi-tone harmonic balance. In theory, the number of harmonics used can be large, but this is primarily limited by the efficiency of the minimization function and computational resources.

Finally, the circuit itself is not limited in shape, as long as admittance parameters can be formed of the linear subnetworks with ports in the locations of the nonlinear loading. Every component added to the circuit can either be absorbed into an admittance matrix or modeled with a time-domain equation describing the relationship between voltage and current.

2.4.2 Time-varying Devices

Harmonic balance normally cannot handle any switching or time-varying components, but it is possible with a slight modification to the voltage-current relationship of the device, as mentioned in Section 2.3.2.2. In the implementation of the piecewise harmonic balance method in MATLAB, the nonlinear circuit can be analyzed using a function that maps voltage to current in the time domain. Because it is in the time domain that this takes place, it is possible to create a function that changes with time. The change over time must have a period that is harmonically related to the base frequency. In other words, one period of the base frequency contains an integer multiple of the period of the change over time. This

modification allows harmonic balance to model switches that open and close periodically.

2.5 Concluding Remarks

In this chapter the harmonic balance method was analyzed and combined with MoM, creating a technique that can model nonlinear loading on an arbitrarily shaped structure. This method can be directly expanded for multiple nonlinear loads of any kind. Various examples are presented that demonstrates different nonlinear loading and how they can be implemented with harmonic balance as well as verify its accuracy against other nonlinear circuit solvers.

While this method has limitations, discussed previously in Section 2.4, it remains a versatile nonlinear solver that allows for accurate modeling by using both the frequency and time domain to analyze the LTI and nonlinear subcircuits. Expanding harmonic balance with MoM allows for the simulation of electromagnetic structures with nonlinear components. The next chapters discuss conversion matrices as a method to model time-varying systems and allows for a combination of harmonic balance and conversion matrices to model pumped nonlinearities, briefly discussed in Section 5.5.

Chapter 3

Time-Variant Modeling

Recently, a hybrid method of modeling time-varying electromagnetic structures based on conversion matrices and the method of moments (MoM) has been developed [32], [64]. While time-domain modeling, such as the finite difference time domain method (FDTD), transient circuit co-simulation and time-domain method of moments are accurate and extremely general [12], the direct connection between MoM and the dyadic Green's function makes MoM-based modeling favorable in applications such as modal current analysis [65], [66], automated design synthesis [67]–[69], and the development of fundamental bounds on LTI system performance [70], [71]. Meanwhile, conversion matrices enable the analysis of time-varying structures in the frequency domain by modeling the mixing properties and harmonic generation of time-varying structures as interactions between networked ports, allowing integration with strictly LTI-based solvers. Early combinations of conversion matrices and MoM have focused on sparse loading or the reduction of an antenna to a single lumped impedance, ignoring the potential interaction between multiple or distributed time-varying loads. Conversely, the hybrid conversion matrix / MoM model (CMMoM) preserves the full MoM analysis of electromagnetic structures and provides a framework to efficiently model any number of lumped or distributed loads and the interactions between them [32], [33].

While CMMoM is versatile and can be applied to any electromagnetic object, many of

the fundamental advantages of MoM, such as developing performance bounds, have yet to be explored. In this chapter, key aspects of conversion matrices and the CMMoM model are reviewed before investigating the structure of the resulting impedance matrices in order to determine how a passive time-varying structure affects the impedance and power of an electromagnetic scatterer, as well as extracting a model for the interaction between multiple time-varying loads in the form of an equivalent loading matrix. Additionally, a method of determining fundamental bounds on extincted power and efficiency based on MoM are derived for CMMoM and several case studies are investigated.

3.1 Conversion Matrix Circuit Analysis

Conversion matrices enable frequency-domain modeling of systems with time-varying components by describing the coupling between voltages and currents at multiple frequencies [26]. Their use in circuit design is well documented, but these techniques are rarely applied to electromagnetic scattering problems. The fundamentals of conversion matrix methods on multiport networks are reviewed in preparation for their application to open, distributed electromagnetic systems via MoM.

3.1.1 Lumped Time-Varying Components

When a time-varying voltage is impressed across a time-varying load, the spectral content of the resulting current corresponds to a mixing of the applied voltage with the time-variation of the load. This can be seen by applying the convolution theorem to Ohm's law, as in

$$i(t) = v(t)g(t) \tag{3.1}$$

and

$$I(\omega) = \int_{-\infty}^{\infty} V(\omega - \omega')G(\omega')\mathrm{d}\omega' \tag{3.2}$$

where $i(t)$, $v(t)$, and $g(t)$ are the time-domain current, voltage, and conductance of the load, and $I(\omega)$, $V(\omega)$, and $G(\omega)$ are their Fourier transforms. In an LTI system, the conductance has only a static component $G(\omega) \sim \delta(\omega)$, and the current can only contain frequencies that are present in the voltage excitation. When the conductance $g(t)$ is not static, the resulting current includes sum- and difference-mixing products of the voltage and load frequency content.

The preceding discussion is valid for loads with arbitrary time dependence. If the load's time variation is periodic, it may be represented by a Fourier series as

$$g(t) = \sum_{k=-K}^{K} G_k \mathrm{e}^{\mathrm{j}k\omega_0 t} \tag{3.3}$$

and

$$G(\omega) = \sum_{k=-K}^{K} G_k \delta(\omega - k\omega_0), \tag{3.4}$$

where $g(t)$ is the time-varying conductance of the load, G_k is the kth Fourier coefficient, ω_0 is the fundamental frequency of the time-varying component, and K is large enough to contain sufficient frequency-domain content. Similarly, we may expand the voltage in terms of a series of ω_0 harmonics centered about a reference frequency ω_c,

$$v(t) = \sum_{k=-K}^{K} V_k \mathrm{e}^{\mathrm{j}(\omega_\mathrm{c} + k\omega_0)t} \tag{3.5}$$

and

$$V(\omega) = \sum_{k=-K}^{K} V_k \delta(\omega - \omega_\mathrm{c} - k\omega_0) \tag{3.6}$$

so long as the baseband representation of the driving voltage is periodic in the fundamental

frequency ω_0. If the voltage is not periodic in ω_0, then the excitation can be decomposed into multiple problems with different center frequencies. In this chapter, a single frequency excitation is assumed, where this condition is naturally satisfied as $V_k = 0$ for all $k \neq 0$. As a consequence of centering the harmonics about a reference frequency ω_c, as in (3.6), the negative frequency components of the excitation signal are ignored. Instead we focus on the upper sideband as shown in Fig. 3.1. If desired, contributions from negative frequencies may be calculated by a secondary calculation [26].

Adopting the same expansion and notation for the current $i(t)$, the conductance relationship in (3.2) may be written as

$$I_k = \sum_{\ell=-L}^{L} V_{k-\ell} G_\ell \tag{3.7}$$

and in matrix form as

$$\begin{bmatrix} I_{-K} \\ I_{1-K} \\ \vdots \\ I_K \end{bmatrix} = \begin{bmatrix} G_0 & G_{-1} & \dots & G_{-2K} \\ G_1 & G_0 & \dots & G_{1-2K} \\ \vdots & \vdots & \ddots & \vdots \\ G_{2K} & G_{2K-1} & \dots & G_0 \end{bmatrix} \begin{bmatrix} V_{-K} \\ V_{1-K} \\ \vdots \\ V_K \end{bmatrix} \tag{3.8}$$

or more compactly

$$\hat{\mathbf{I}} = \hat{\mathbf{G}}\hat{\mathbf{V}} \tag{3.9}$$

where $\hat{\mathbf{G}}$ is the conversion matrix representation of the time-varying conductance $g(t)$. This matrix models the modulating effect of the time-varying component, where the kth element of the current vector contains contributions from every $G_p V_q$ product that satisfies $p + q = k$.

An expression similar to (3.8) can be derived using a time-varying resistance, rather

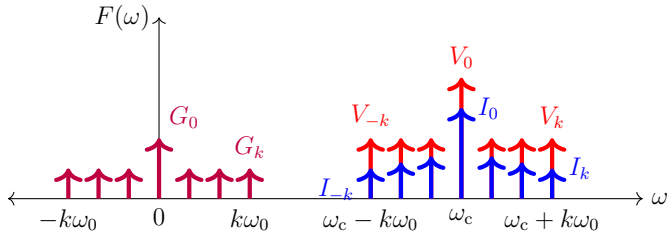

Figure 3.1: Frequency convention used throughout this chapter. Time-varying loads are represented in Fourier series of the fundamental frequency ω_0, e.g., $\{G_k\}$, while current and voltage indexing centers around a modulation frequency ω_c.

than conductance [26]. This illustrates an inverse relationship between resistive and conductive conversion matrices, similar to that of their LTI counterparts,

$$\hat{\mathbf{R}} = \hat{\mathbf{G}}^{-1}. \tag{3.10}$$

Conversion matrices may also be generated for time-varying inductors and capacitors, with the general structure

$$\hat{\mathbf{I}} = \mathrm{j}\hat{\mathbf{\Omega}}\hat{\mathbf{C}}\hat{\mathbf{V}} \qquad \text{and} \qquad \hat{\mathbf{V}} = \mathrm{j}\hat{\mathbf{\Omega}}\hat{\mathbf{L}}\hat{\mathbf{I}} \tag{3.11}$$

where

$$\hat{\mathbf{\Omega}} = \begin{bmatrix} \omega_{-K} & 0 & \dots & 0 \\ 0 & \omega_{1-K} & \dots & 0 \\ \vdots & \vdots & \ddots & \vdots \\ 0 & 0 & \dots & \omega_K \end{bmatrix}, \quad \omega_k = \omega_c + k\omega_0, \tag{3.12}$$

and the matrices $\hat{\mathbf{C}}$ and $\hat{\mathbf{L}}$ are capacitance and inductance conversion matrices of the form of the matrix $\hat{\mathbf{G}}$ in (3.8). The conversion matrices of conductances $\hat{\mathbf{G}}$, resistances $\hat{\mathbf{R}}$, capacitances $\hat{\mathbf{C}}$, and inductances $\hat{\mathbf{L}}$, can be treated as basic lumped components and combined into larger networks by following usual series and parallel circuit rules [26]. For real-

valued time-varying circuit elements, the matrices $\hat{\mathbf{G}}$, $\hat{\mathbf{R}}$, $\hat{\mathbf{L}}$, and $\hat{\mathbf{C}}$ are naturally Hermitian symmetric. However, multiplication of $\hat{\mathbf{C}}$ or $\hat{\mathbf{L}}$ by the frequency matrix $\hat{\mathbf{\Omega}}$ or its inverse, as in (3.11), breaks the Hermitian symmetry of the impedance conversion matrices of time-varying inductive or capacitive elements.

3.1.2 Loaded Multi-port Networks

The time-domain representation of an LTI, N-port network with time-varying resistors on each port may be written as

$$v_\alpha(t) = i_\alpha(t) r_\alpha(t) + \sum_{\beta=1}^{N} z_{\alpha\beta}(t) \star i_\beta(t) \tag{3.13}$$

where $v_\alpha(t)$, $i_\alpha(t)$, and $r_\alpha(t)$ are the time-varying voltage, current, and resistance across port α, and $z_{\alpha\beta}(t)$ is the open-circuit impedance impulse response between ports α and β. This translates to a frequency-domain representation

$$V_\alpha(\omega) = \int_{-\infty}^{\infty} I_\alpha(\omega - \omega') R_\alpha(\omega') \mathrm{d}\omega' + \sum_{\beta=1}^{N} Z_{\alpha\beta}(\omega) I_\beta(\omega) \tag{3.14}$$

where $V_\alpha(\omega)$, $I_\alpha(\omega)$, $R_\alpha(\omega)$, and $Z_{\alpha\beta}(\omega)$ are the frequency-domain forms of the parameters in (3.13).

After manipulations closely resembling those in (3.4) and (3.6), the equation for voltage becomes

$$\begin{aligned} V_\alpha(\omega_c + k\omega_0) = \sum_{\ell=-L}^{L} & I_\alpha(\omega_c + (k-\ell)\omega_0) R_\alpha(\ell\omega_0) \\ & + \sum_{\beta=1}^{N} Z_{\alpha\beta}(\omega_c + k\omega_0) I_\beta(\omega_c + k\omega_0), \end{aligned} \tag{3.15}$$

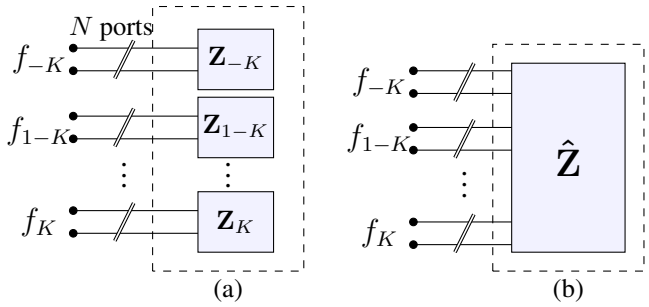

Figure 3.2: Diagram of LTI multiport system (a) and periodically time-varying multiport system (b) as represented by a conversion matrix. Double slash across port symbol denotes N physical ports. Each physical port supports voltages and currents at each of the $2K+1$ harmonic frequencies. An LTI system with $2K+1$ frequencies can be represented by $2K+1$ independent linear systems, or a block diagonal conversion matrix, because there is no conversion between frequencies.

and after including the frequency notation from (3.8) as superscripts, the previous expression may be rewritten as

$$V_\alpha^k = \sum_{\ell=-L}^{L} I_\alpha^{k-\ell} R_\alpha^\ell + \sum_{\beta=1}^{N} Z_{\alpha\beta}^k I_\beta^k. \tag{3.16}$$

Equations of this form can be collected into a matrix form by grouping the port voltages and currents at each frequency. The resulting system of equations reads

$$\begin{bmatrix} \mathbf{V}^{-K} \\ \mathbf{V}^{1-K} \\ \vdots \\ \mathbf{V}^{K} \end{bmatrix} = \begin{bmatrix} \mathbf{R}^0 & \mathbf{R}^{-1} & \dots & \mathbf{R}^{-2K} \\ \mathbf{R}^1 & \mathbf{R}^0 & \dots & \mathbf{R}^{1-2K} \\ \vdots & \vdots & \ddots & \vdots \\ \mathbf{R}^{2K} & \mathbf{R}^{2K-1} & \dots & \mathbf{R}^0 \end{bmatrix} \begin{bmatrix} \mathbf{I}^{-K} \\ \mathbf{I}^{1-K} \\ \vdots \\ \mathbf{I}^{K} \end{bmatrix} + \begin{bmatrix} \mathbf{Z}^{-K} & 0 & \dots & 0 \\ 0 & \mathbf{Z}^{1-K} & \dots & 0 \\ \vdots & \vdots & \ddots & \vdots \\ 0 & 0 & \dots & \mathbf{Z}^{K} \end{bmatrix} \begin{bmatrix} \mathbf{I}^{-K} \\ \mathbf{I}^{1-K} \\ \vdots \\ \mathbf{I}^{K} \end{bmatrix} \tag{3.17}$$

and has a similar structure to the conversion matrices of (3.8), with the key difference that every element within each matrix or vector is replaced by a submatrix or subvector of dimension N. The submatrices and subvectors take the forms

$$\mathbf{R}^k = \begin{bmatrix} R_1^k & 0 & \dots & 0 \\ 0 & R_2^k & \dots & 0 \\ \vdots & \vdots & \ddots & \vdots \\ 0 & 0 & \dots & R_N^k \end{bmatrix}, \tag{3.18a}$$

$$\mathbf{Z}^k = \left[Z_{\alpha\beta}^k\right], \quad \mathbf{V}^k = \left[V_\alpha^k\right], \quad \mathbf{I}^k = \left[I_\alpha^k\right]. \tag{3.18b}$$

Thus, $\mathbf{R}^k$ is a diagonal matrix consisting of the k-th harmonic of the time-varying resistances at all N ports, $\mathbf{Z}^k$ is the open-circuit impedance matrix of the N-port LTI network at the k-th harmonic centered about ω_c, and $\mathbf{V}^k$ and $\mathbf{I}^k$ contain voltages and currents existing on all N ports at the k-th harmonic, as illustrated in Fig. 3.2(b). The system of equations in (3.17) may be expressed in a more compact form as

$$\hat{\mathbf{V}} = \left(\hat{\mathbf{R}} + \hat{\mathbf{Z}}\right)\hat{\mathbf{I}}. \tag{3.19}$$

For the case of purely LTI loading, we have $\hat{\mathbf{R}}^{k\neq 0} = 0$ and the matrices in (3.17) reduce to a block diagonal matrix as shown in Fig. 3.2(a). As a result, the system is represented by $2K+1$ decoupled matrix equations at each harmonic. While reciprocal LTI networks lead to symmetric conversion matrices $\hat{\mathbf{Z}}$, the conversion matrices for real-valued loads are Hermitian symmetric based on the conjugate symmetry of their Fourier representations. Thus, unless loads are selected specifically to have real-valued Fourier spectra, the system conversion matrix $\hat{\mathbf{Z}} + \hat{\mathbf{R}}$ is neither symmetric nor Hermitian. Representations similar to (3.19) may be constructed for arbitrary networks of time-varying resistances, capacitances, and

inductances using the forms in (3.10) and (3.11) along with standard circuit element combination rules [26].

If desired, the multi-port conversion matrix can be grouped by port rather than by frequency [26]. This arrangement would lead to an overall matrix structure that resembled an open-circuit impedance matrix, with each element in the matrix replaced by a small conversion matrix, i.e.,

$$\begin{bmatrix} \hat{\mathbf{V}}_1 \\ \hat{\mathbf{V}}_2 \\ \vdots \\ \hat{\mathbf{V}}_N \end{bmatrix} = \begin{bmatrix} \hat{\mathbf{Z}}_{11} & \hat{\mathbf{Z}}_{12} & \dots & \hat{\mathbf{Z}}_{1N} \\ \hat{\mathbf{Z}}_{21} & \hat{\mathbf{Z}}_{22} & \dots & \hat{\mathbf{Z}}_{2N} \\ \vdots & \vdots & \ddots & \vdots \\ \hat{\mathbf{Z}}_{N1} & \hat{\mathbf{Z}}_{N2} & \dots & \hat{\mathbf{Z}}_{NN} \end{bmatrix} \begin{bmatrix} \hat{\mathbf{I}}_1 \\ \hat{\mathbf{I}}_2 \\ \vdots \\ \hat{\mathbf{I}}_N \end{bmatrix} \tag{3.20}$$

where $\hat{\mathbf{V}}_\alpha$, $\hat{\mathbf{I}}_\alpha$, and $\hat{\mathbf{Z}}_{\alpha\beta}$ are conversion matrix parameters as defined in (3.8), but specific to the α and β ports of the N-port network. The matrices in (3.17) and (3.20) share the same elements, but are re-ordered to emphasize different relationships. While other work in multiport conversion matrices use a port-wise arrangement [26], [72], this work uses the format of (3.17) to facilitate compatibility with standard MoM techniques, as will be discussed in the next section.

3.2 Conversion Matrix / Method of Moments

The previous section derived the equations for conversion matrices on basic circuits and provided a method to combine lumped LTI and time-varying components together. This section directly applies conversion matrices to the method of moments, allowing for the modeling and simulation of time-varying electromagnetic structures [32].

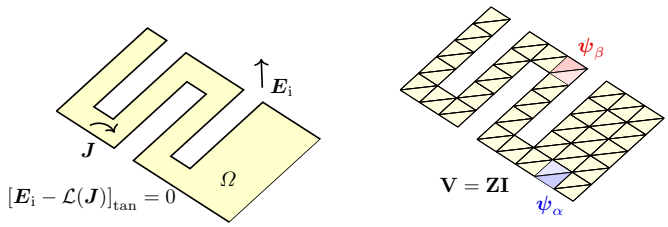

Figure 3.3: Discretization of a structure Ω (left) into finite elements supporting localized basis functions $\{\boldsymbol{\psi}_n\}$ (right). RWG basis functions [74] are depicted, with each basis function centered on one mesh edge and spanning two adjacent triangles.

3.2.1 Formulation

A broad class of LTI electromagnetic scattering problems may be recast as LTI network problems through the use of the method of moments (MoM) [73]. Consider a problem involving a perfectly conducting (PEC) surface Ω supporting surface currents $\boldsymbol{J}$, as shown in the left panel of Fig. 3.3. To solve for the surface currents induced by a monochromatic incident field $\boldsymbol{E}_{\mathrm{i}}$, we may expand the surface current into an appropriate basis $\{\boldsymbol{\psi}_n\}$ in order to convert Maxwell's equations into a matrix form of the electric field integral equation

$$\mathbf{V}(\omega) = \mathbf{Z}(\omega)\mathbf{I}(\omega) \tag{3.21}$$

where $\mathbf{V}$ and $\mathbf{I}$ are vectors containing coefficients related to the incident field and induced current, respectively, ω is the excitation frequency, and $\mathbf{Z}$ is the impedance matrix representing the scattered field operator $\mathcal{L}(\boldsymbol{J})$ [73]. Throughout this chapter, Galerkin testing is applied such that the impedance matrix is transpose symmetric. The frequency dependence of all quantities, to be dropped in all future expressions, explicitly describes the LTI nature of the scatterer and indicates that currents will only exist at the excitation frequency. Induced currents due to multi-tone excitation can be analyzed by direct superposition of weighted monochromatic solutions, i.e., Fourier series or transforms.

3.2.2 Loading

When the chosen basis is sufficiently localized, e.g., when pulse [75], or RWG basis functions [74] are used, the elements of the vectors $\mathbf{V}$ and $\mathbf{I}$ may be interpreted as voltages and currents present at discrete locations, or ports, on the structure, as shown in the right panel of Fig. 3.3. For example, in the case of RWG basis functions, each port corresponds to one edge within the triangularized mesh created from the original structure Ω.

With the aforementioned network interpretation of the electromagnetic scattering problem in Fig. 3.3, lumped loading at any combination of the scatterer's ports is straightforward to model via the addition of a diagonal loading matrix to the impedance matrix $\mathbf{Z}_{\mathrm{L}}$,

$$\mathbf{Z} \rightarrow \mathbf{Z} + \mathbf{Z}_{\mathrm{L}}, \tag{3.22}$$

whose elements are related to the lumped element loading at each port [76]. Loads of finite size spanning multiple basis functions may also be modeled through the use of non-diagonal loading matrices [77]. An identical approach also allows for the modeling of non-PEC surfaces, which may be inhomogeneous and/or anisotropic, characterized by surface impedance Z_{s} through a non-diagonal loading matrix related to the Gram matrix of the chosen basis [70], [76].

3.2.3 Lumped Time-Varying Loads

The techniques outlined in Sections 3.1.2 and 3.2.2 may be combined to model time-varying lumped elements loading any or all ports of a MoM network representation of the structure Ω. The resulting conversion matrix system takes on precisely the same form as (3.17)–(3.19), where $\hat{\mathbf{V}}$ and $\hat{\mathbf{I}}$ are stacked vectors containing fields and currents at all harmonic frequencies, and $\hat{\mathbf{R}}$ and $\hat{\mathbf{Z}}$ are the dynamic (associated with time-varying loading)

and static (associated with the underlying LTI structure) conversion matrices, respectively.

Here we again note that the static conversion matrix $\hat{\mathbf{Z}}$ is block diagonal and contains impedance matrices representing the structure Ω at each harmonic frequency. The individual blocks $\mathbf{R}^k$ of the dynamic loading matrix $\hat{\mathbf{R}}$ are diagonal for localized bases, with off diagonal blocks $\mathbf{R}^{k\neq 0}$ representing Fourier components of each element's time variation. In the special cases when the structure is unloaded or if all loading elements are static, the system becomes LTI and the system conversion matrix becomes block diagonal, reducing to a set of $2K+1$ decoupled matrix equations, each involving only quantities at a single frequency. Generalization to capacitive and inductive loads follows the form of (3.12), and again combinations of LTI and/or time-varying components may be synthesized by standard circuit analysis rules [26].

3.3 Examples

In this section, a selection of example problems solved using the hybridized conversion matrix / method of moments (CMMoM) technique are presented [32]. Like conventional method of moments, the proposed method is capable of modeling a broad range of practical antenna and scattering problems. The examples included here highlight the method's application to scattering, transmission, and reception using structures with lumped time-varying loads.

3.3.1 Scattering from a singly-loaded bowtie dipole

The first examples is a bowtie antenna loaded at its center by a time-varying switch, as shown in the inset of Fig. 3.4. The bowtie length ℓ is $36\,\mathrm{mm}$ and the angle α between the

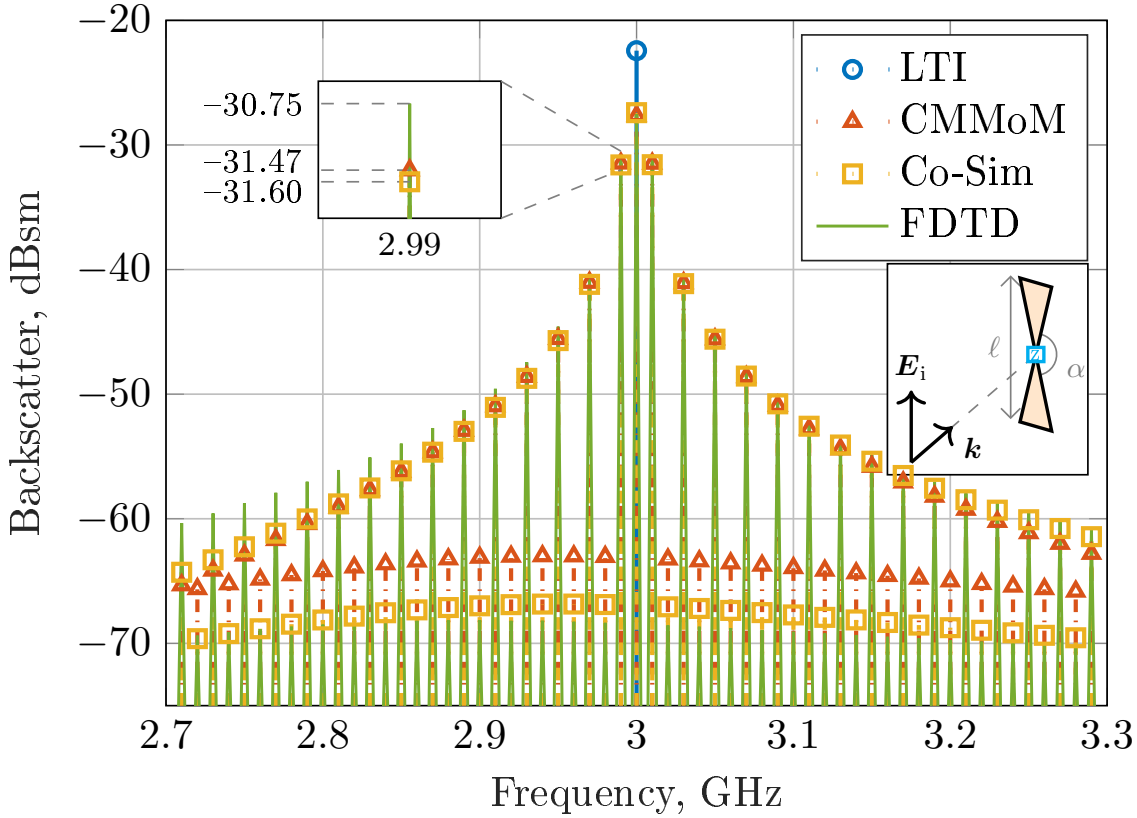

Figure 3.4: Cross-frequency backscatter spectra from CMMoM, transient circuit co-simulation, FDTD, and measurement, compared to backscatter from LTI bowtie. Inset schematic.

two arms is $155°$. The central switch is modeled by

$$R_{\mathrm{L}}(t) = \begin{cases} r_0 & t_{\mathrm{L}}/2 \leq t - nt_{\mathrm{L}} < t_{\mathrm{L}} \\ 0 & \text{else} \end{cases} \tag{3.23}$$

with an off-resistance r_0 of 10 kΩ and switching frequency $f_{\mathrm{L}} = 1/t_{\mathrm{L}}$ of 10 MHz.

The excitation is an incident plane wave from broadside at 3 GHz co-polarized with the long dimension of the bowtie and is defined as

$$\boldsymbol{e}^{\mathrm{inc}}(t, \boldsymbol{r}) = \hat{\boldsymbol{z}} E_0 \sin \omega_{\mathrm{inc}} t, \quad \forall\, \boldsymbol{r} = \hat{\boldsymbol{y}} y + \hat{\boldsymbol{z}} z \tag{3.24}$$

in the plane of the bowtie antenna ($x = 0$) where t is the same time variable shared by the load. Fig. 3.4 shows the monostatic backscatter produced by this system. Note that while the excitation in this example is monochromatic, the scattered fields consist of multiple harmonics due to the time-varying load. Similar to polarization-specific scattering analysis, here we adopt the following notation for multi-harmonic backscatter,

$$\Psi(\omega_{\mathrm{inc}}, \omega_{\mathrm{obs}}) = \lim_{r\to\infty} 4\pi r^2 \frac{|\boldsymbol{E}^{\mathrm{sc}}(\omega_{\mathrm{obs}})|^2}{|\boldsymbol{E}^{\mathrm{inc}}(\omega_{\mathrm{inc}})|^2} \tag{3.25}$$

where $\boldsymbol{E}^{\mathrm{inc}}$ and $\boldsymbol{E}^{\mathrm{sc}}$ are incident and backscattered fields, r is a distance from the scattering object, and ω_{inc} and ω_{obs} are the incident and observation angular frequencies, respectively.

A CMMoM model of the bowtie example structure was constructed with 170 triangles, 220 RWG basis functions, and 201 harmonic frequencies. Fig. 3.4 shows the agreement between CMMoM, a commercial FDTD code [78], and transient circuit co-simulation [79]. CMMoM results from a static bowtie with no time-varying load are also included for comparison. The CMMoM, FDTD, and circuit co-simulation results of the time-varying bowtie model agree within 0.3 dB at the zeroth harmonic (incident frequency) and 0.9 dB at the first-order harmonics. There is larger relative (dB) error in the higher order harmonics, though the linear magnitudes of these differences are relatively small due to the much smaller absolute magnitude of these higher order harmonics.

We observe that the backscatter spectrum contains primarily odd-numbered harmonics of the $500\,\mathrm{MHz}$ square wave switching waveform, which is to be expected since the Fourier series of a square wave contains only odd numbered harmonics. It should be noted that physical systems with linear time-varying loads contain only intermodulation frequencies of the excitation signal and time-varying loading waveform. By definition, CMMoM produces output only at these discrete harmonic frequencies, which are known a priori. Time-domain methods, on the other hand, can produce additional, spurious spectral con-

Table 3.1: Comparison of backscatter (dBsm) data from Fig. 3.4

	Static	Time-varying				
	$k = 0$	-2	-1	0	1	2
Co-sim	-21.5	-66.9	-31.6	-27.4	-31.6	-67.2
CMMOM	-21.5	-63.0	-31.5	-27.7	-31.5	-63.3
FDTD	-21.1	-68.4	-30.7	-27.5	-30.8	-68.6

tent due to transient and windowing effects.

Figure 3.5 shows the normalized backscattered power as a function of declination angle θ due to an excitation field incident from $\theta = 90°$. The pattern of the reflected field for each harmonic has the shape of a center-fed dipole, with nulls in endfire directions and peaks at broadside. The magnitude of each harmonic pattern at broadside corresponds to the peak values in Fig. 3.4 and the values listed in Table 3.1.

3.3.2 Harmonic generation in a multiply-loaded transmit system

The second example is a square wire loop antenna loaded on opposite sides by two sinusoidally-varying time-varying loads, selected either as time-varying resistors or time-varying capacitors. The loop has a side length ℓ of 82.8 mm and a radius of 1 mm. The time-varying loads are defined by

$$R_{\mathrm{L}}(t) = R_0 \left(1 + \gamma \cos \omega_L t\right), \tag{3.26}$$

and

$$C_{\mathrm{L}}(t) = C_0 \left(1 + \gamma \cos \omega_L t\right), \tag{3.27}$$

where

$$R_0 = 150\,\Omega, \quad C_0 = 5\,\mathrm{pF}, \tag{3.28}$$

and the frequency of the loads is set to $f_L = \omega_L/(2\pi) = 30\,\mathrm{MHz}$. The modulation coefficient γ prevents the resistance and capacitance from reaching zero, which would lead

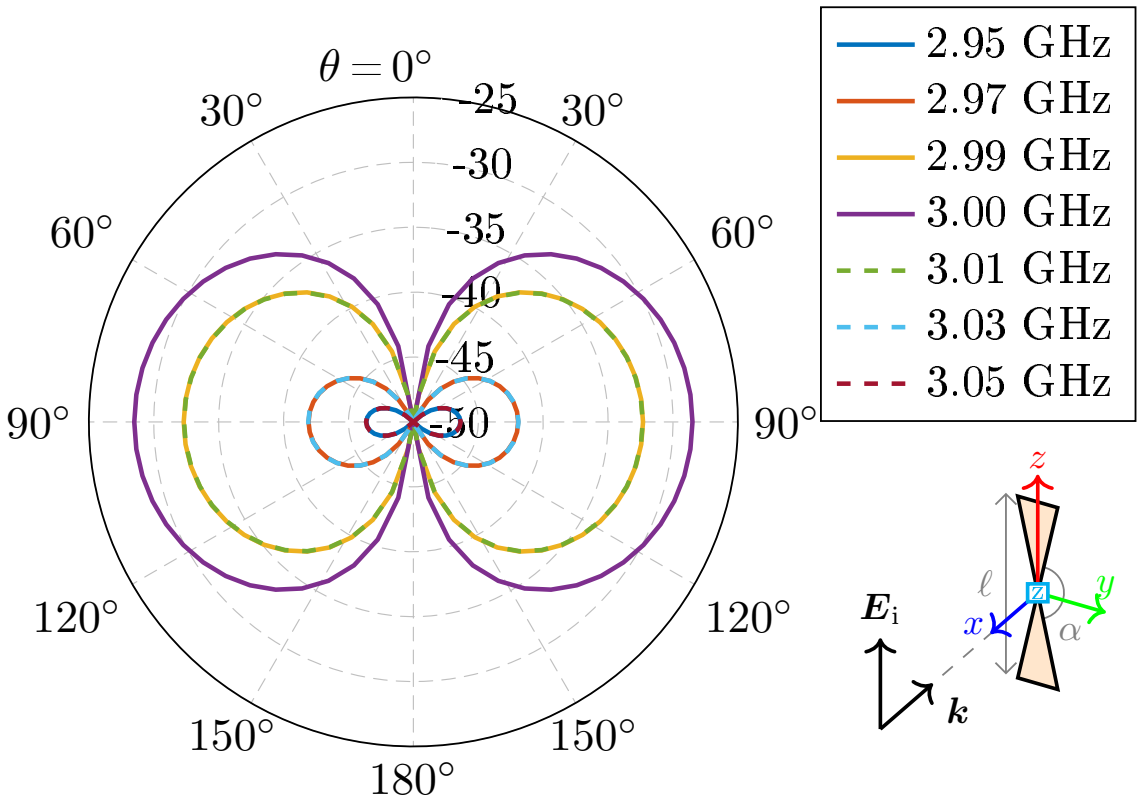

Figure 3.5: Normalized backscattered power (dBsm) of the bowtie example from CM-MoM vs. declination angle θ in the xz plane for the frequencies of greatest returned power.

to divergent Fourier representations of the conductance and elastance. In this example, the modulation coefficient γ is set to 0.95. The excitation is a voltage gap feed at $1\,\mathrm{GHz}$ located next to one of the loads and defined as

$$v^{\mathrm{inc}}(t) = V_0 \cos \omega_{\mathrm{inc}} t \tag{3.29}$$

where $V_0 = 1\ \mathrm{V}$ and t is the same time variable shared by the loads. The voltage source location, as well as the locations of the resistive and capacitive loads, are shown in Fig. 3.6.

The CMMoM model of the square loop is constructed with 66 rooftop basis functions with 191 harmonic frequencies. The radiated electric field in the direction normal to the loop for a $1\,\mathrm{GHz}$ excitation is shown in Fig. 3.6. Similar to the bowtie example, the excitation frequency is modulated by the load frequency to produce harmonics, but in this case both even and odd harmonics are prominent because of the sinusoidal load waveform. The capacitive loads show more radiated power compared to the resistive loads, which are lossy by nature.

3.4 Rederiving Basic Network Relations with CMMoM

Incorporating time-varying devices into other LTI structures typically defined in the frequency domain, such as transmission lines, can be done by modifying the governing equations with conversion matrices. Similar to the derivation of CMMoM, parameters must be reconstructed from the base voltage and current distributions defined in conversion matrices and accounting for any cross-frequency terms. This section describes a loaded transmission line and shows the calculation of several key parameters when it is loaded with a time-varying element. The model of the loaded transmission line is shown in Figure 3.7.

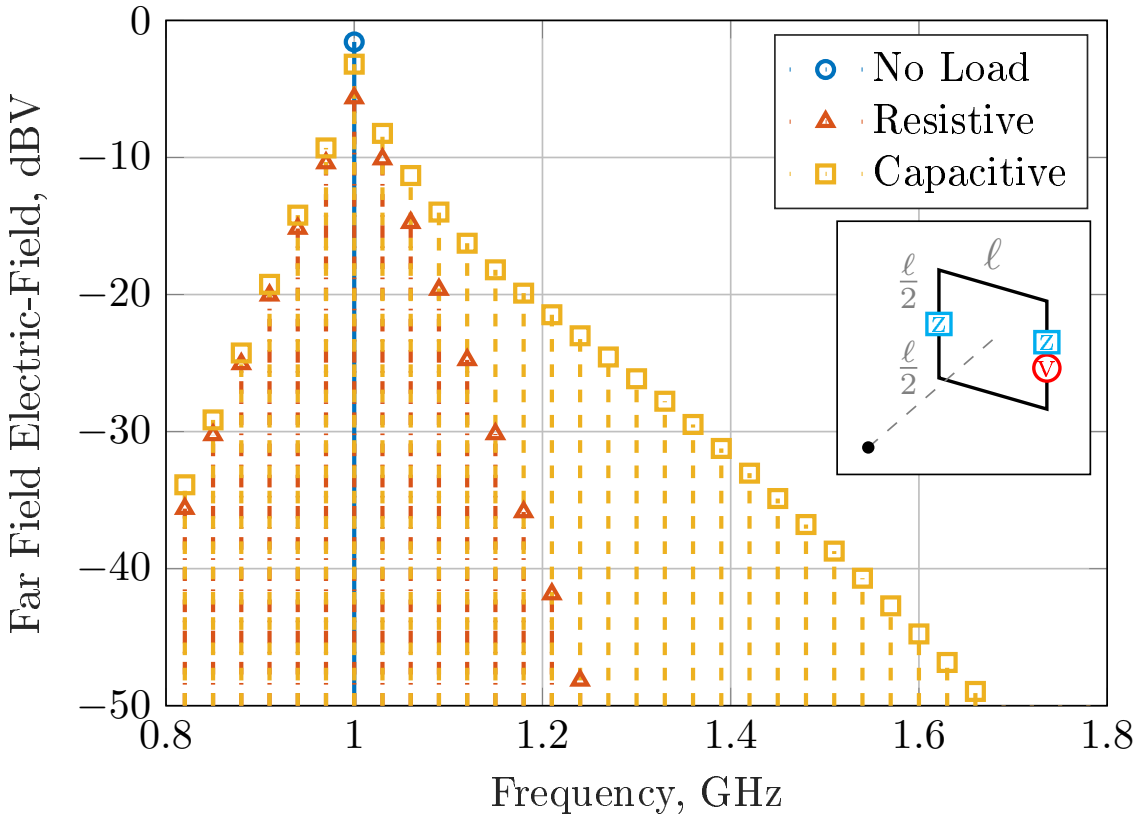

Figure 3.6: CMMoM calculation of broadside radiated electric fields from a transmitting square loop loaded with two time-varying resistive or capacitive loads. Load (blue) and voltage source (red) locations are shown on the inset schematic.

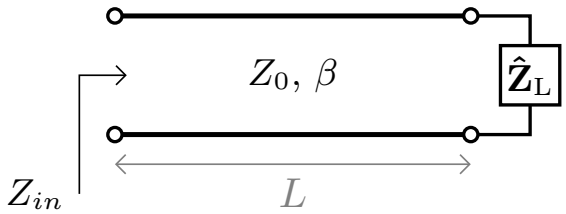

Figure 3.7: Diagram of a transmission line of length L, characteristic impedance Z_0, and propagation constant β that is loaded with a time-varying impedance $\hat{\mathbf{Z}}_{\mathrm{L}}$.

3.4.1 Loading

The load on the transmission line can be a single time-varying element or an effective input impedance from a combination of LTI elements with one or more time-varying components combined into a single conversion matrix, as discussed in Section 3.1.1. This section uses a generalized time-varying load $\hat{\mathbf{Z}}_{\mathrm{L}}$, which is a single port conversion matrix with a structure similar to (3.8).

3.4.2 Reflection Coefficient

This derivation for transmission line equations is very similar to any transmission line set up, but here matrices are used in place of scalars. Beginning with a conversion matrix representation of voltage, impedance, and current defined as

$$\hat{\mathbf{V}} = \hat{\mathbf{Z}}_{in}\hat{\mathbf{I}}, \tag{3.30}$$

the voltage and current vectors are replaced as the sum of two propagating waves: toward the load $\hat{\mathbf{V}}^{+}$, $\hat{\mathbf{I}}^{+}$ and away from the load $\hat{\mathbf{V}}^{-}$, $\hat{\mathbf{I}}^{-}$ so that the equation becomes

$$\hat{\mathbf{V}}^{+} + \hat{\mathbf{V}}^{-} = \hat{\mathbf{Z}}_{in}\left(\hat{\mathbf{I}}^{+} - \hat{\mathbf{I}}^{-}\right). \tag{3.31}$$

On a transmission line, the voltage and current waves are related by the characteristic impedance of the line $\hat{\mathbf{Z}}_0$, letting us define the previous equation in terms of voltage only as

$$\hat{\mathbf{V}}^{+} + \hat{\mathbf{V}}^{-} = \hat{\mathbf{Z}}_{in}\hat{\mathbf{Z}}_0^{-1}\left(\hat{\mathbf{V}}^{+} - \hat{\mathbf{V}}^{-}\right). \tag{3.32}$$

The reflection coefficient $\hat{\mathbf{\Gamma}}$ defines the relationship between the magnitudes of the forward and backward waves at the load location as

$$\hat{\mathbf{V}}^{-} = \hat{\mathbf{\Gamma}}\hat{\mathbf{V}}^{+} \tag{3.33}$$

and can be calculated by analyzing (3.32) at the location of the load, where $\hat{\mathbf{Z}}_{in} = \hat{\mathbf{Z}}_{\mathrm{L}}$, so that

$$\hat{\mathbf{V}}^{+} + \hat{\mathbf{V}}^{-} = \hat{\mathbf{Z}}_{\mathrm{L}}\hat{\mathbf{Z}}_{0}^{-1}\left(\hat{\mathbf{V}}^{+} - \hat{\mathbf{V}}^{-}\right) \tag{3.34}$$

which, by solving for $\hat{\mathbf{V}}^{-}$ becomes

$$\hat{\mathbf{V}}^{-} = \left(\hat{\mathbf{Z}}_{0}^{-1} + \hat{\mathbf{Z}}_{\mathrm{L}}^{-1}\right)^{-1}\left(\hat{\mathbf{Z}}_{0}^{-1} - \hat{\mathbf{Z}}_{\mathrm{L}}^{-1}\right)\hat{\mathbf{V}}^{+} \tag{3.35}$$

and, by combining the previous equations, we can calculate the reflection coefficient as

$$\hat{\mathbf{\Gamma}} = \left(\hat{\mathbf{Z}}_{0}^{-1} + \hat{\mathbf{Z}}_{\mathrm{L}}^{-1}\right)^{-1}\left(\hat{\mathbf{Z}}_{0}^{-1} - \hat{\mathbf{Z}}_{\mathrm{L}}^{-1}\right). \tag{3.36}$$

Similarly, the transmission coefficient $\hat{\mathbf{T}}$ can be calculated with

$$\hat{\mathbf{V}}^{+} + \hat{\mathbf{V}}^{-} = \hat{\mathbf{V}}^{\mathrm{T}} \tag{3.37}$$

where $\hat{\mathbf{V}}^{\mathrm{T}} = \hat{\mathbf{T}}\hat{\mathbf{V}}^{+}$ is the transmitted voltage wave, resulting in

$$\hat{\mathbf{T}} = \hat{\mathbf{I}} + \hat{\mathbf{\Gamma}}. \tag{3.38}$$

3.4.3 Input Impedance

The relationship between forward and backward traveling waves on the transmission line at a distance of L from the load can then be calculated using the reflection coefficient as

$$\hat{\mathbf{V}}^{-} = \hat{\mathbf{\Phi}}\hat{\mathbf{\Gamma}}\hat{\mathbf{\Phi}}\hat{\mathbf{V}}^{+} \tag{3.39}$$

where $\hat{\mathbf{\Phi}}$ is a phase shift term that accounts for the phase of the wave as it travels down the transmission line, reflects off of the load, and travels back. It is defined as

$$\hat{\mathbf{\Phi}} = \begin{bmatrix} \mathrm{e}^{-j\beta_1 L} & 0 & \dots & 0 \\ 0 & \mathrm{e}^{-j\beta_2 L} & \dots & 0 \\ \vdots & \vdots & \ddots & \vdots \\ 0 & 0 & \dots & \mathrm{e}^{-j\beta_N L} \end{bmatrix} \tag{3.40}$$

where β_n is the propagation constant at the n-th frequency. The new equation becomes

$$\hat{\mathbf{V}}^{+} + \hat{\mathbf{\Phi}}\hat{\mathbf{\Gamma}}\hat{\mathbf{\Phi}}\hat{\mathbf{V}}^{+} = \hat{\mathbf{Z}}_{in}\hat{\mathbf{Z}}_0^{-1}\left(\hat{\mathbf{V}}^{+} - \hat{\mathbf{\Phi}}\hat{\mathbf{\Gamma}}\hat{\mathbf{\Phi}}\hat{\mathbf{V}}^{+}\right) \tag{3.41}$$

and can be reduced to

$$\left(\hat{\mathbf{1}} + \hat{\mathbf{\Phi}}\hat{\mathbf{\Gamma}}\hat{\mathbf{\Phi}}\right)\hat{\mathbf{V}}^{+} = \hat{\mathbf{Z}}_{in}\hat{\mathbf{Z}}_0^{-1}\left(\hat{\mathbf{1}} - \hat{\mathbf{\Phi}}\hat{\mathbf{\Gamma}}\hat{\mathbf{\Phi}}\right)\hat{\mathbf{V}}^{+} \tag{3.42}$$

then

$$\hat{\mathbf{1}} + \hat{\mathbf{\Phi}}\hat{\mathbf{\Gamma}}\hat{\mathbf{\Phi}} = \hat{\mathbf{Z}}_{in}\hat{\mathbf{Z}}_0^{-1}\left(\hat{\mathbf{1}} - \hat{\mathbf{\Phi}}\hat{\mathbf{\Gamma}}\hat{\mathbf{\Phi}}\right) \tag{3.43}$$

and finally rearranged to

$$\left(\hat{\mathbf{1}} + \hat{\mathbf{\Phi}}\hat{\mathbf{\Gamma}}\hat{\mathbf{\Phi}}\right)\left(\hat{\mathbf{1}} - \hat{\mathbf{\Phi}}\hat{\mathbf{\Gamma}}\hat{\mathbf{\Phi}}\right)^{-1}\hat{\mathbf{Z}}_0 = \hat{\mathbf{Z}}_{in} \tag{3.44}$$

which gives a matrix representation of the open-circuit impedance looking into a time-varying loaded transmission line.

3.5 Concluding Remarks

In this chapter a hybridized conversion matrix / MoM (CMMoM) technique capable of modeling periodically time-varying linear loads on arbitrarily shaped structures is presented. We formulate the method for multiple lumped time-varying loads. Numerical results from several examples demonstrate the flexibility of the proposed method and verify its accuracy against general purpose time-domain solvers.

The hybridized CMMoM method allows flexible frequency-domain analysis of a wide class of structures, but is not without limitations. First, while this method can be applied to small-signal analysis of nonlinear loads operated under locally linear conditions, it cannot model large-signal nonlinear effects. Second, very large distributed time-varying structures with large numbers of harmonics quickly lead to systems of equations requiring enormous computational effort to solve. Despite these limitations, the method has a variety of uses in the modeling of electromagnetic problems ranging from direct antenna modulation to spatiotemporally modulated materials and allows for a versatile method solving time-varying electromagnetic structures.

Chapter 4

Parametric Amplifiers

In previous chapters, methods of analyzing non-LTI components on electromagnetic structures has been presented, but there has not been much discussion of how these components might be implemented in a realized system. For insight into potential non-LTI antenna design, we turn to parametric amplifiers which have been used since the 1950s. Parametric amplifiers are a class of low noise amplifiers that add power to a system by transferring energy from an oscillating resonator [80]–[82]. They use the harmonic generation property of a time-varying varactor or nonlinear diode to store and discharge energy from a resonator to "pump" power into the excitation frequency. Parametric amplifier analysis typically takes the form of a time-domain method or a matrix method reminiscent of the conversion matrix method presented in Chapter 3. In order to get insight into how time-varying antennas can be effectively designed, we looked to how they have been used and re-derived some fundamental equations of parametric amplifiers.

4.1 Configurations

Parametric amplifiers can take several forms, but they are mostly variations of a series or shunt configuration, shown in Figure 4.1 and 4.2 respectively. Both configurations and their design equations are derived below.

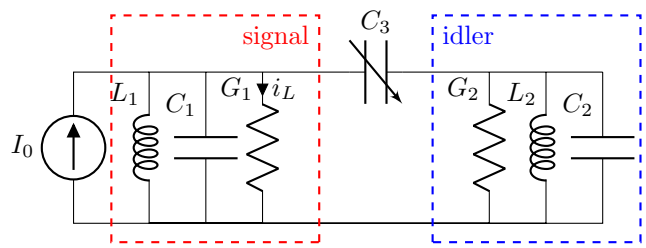

Figure 4.1: Basic design of a parametric amplifier.

4.1.1 Series Configuration

A parametric amplifier uses three primary frequencies: the signal frequency ω_1, the idler frequency ω_2, and the frequency of the time-varying load ω_3. These frequencies are related by $\omega_1 - \omega_3 = \omega_2$. Let us define a time-varying capacitance with the equation

$$C_3(t) = C \sin \omega_3 t \tag{4.1}$$

and with the Fourier coefficients

$$C_- = -\mathrm{j}0.5C, \quad C_0 = 0, \quad C_+ = \mathrm{j}0.5C \tag{4.2}$$

with a fundamental frequency of ω_3. The conversion matrix of the time-varying capacitor is then

$$\hat{\mathbf{C}}_3 = \begin{bmatrix} 0 & C_+ \\ C_- & 0 \end{bmatrix} \tag{4.3}$$

and by evaluating the matrix at frequencies ω_1 and ω_2, the resulting admittance and impedance conversion matrices become

$$\hat{\mathbf{Y}}_3 = \mathrm{j}\hat{\mathbf{\Omega}}\hat{\mathbf{C}}_3 = \begin{bmatrix} 0 & \mathrm{j}\omega_1 C_+ \\ \mathrm{j}\omega_2 C_- & 0 \end{bmatrix} \tag{4.4}$$

and

$$\hat{\mathbf{Z}}_3 = \hat{\mathbf{Y}}_3^{-1} = \frac{1}{\omega_1\omega_2|C_+|^2}\begin{bmatrix} 0 & -\mathrm{j}\omega_1 C_+ \\ -\mathrm{j}\omega_2 C_- & 0 \end{bmatrix} = \begin{bmatrix} 0 & \frac{1}{\mathrm{j}\omega_2 C_-} \\ \frac{1}{\mathrm{j}\omega_1 C_+} & 0 \end{bmatrix} \tag{4.5}$$

and can be treated as a lumped time-varying circuit component and interacts with the other subcircuits of the parametric amplifier.

The series configuration of the parametric amplifier puts the time-varying element in series with the other subcircuits, as shown in Figure 4.1. The idler subcircuit consisting of a shunt resistor G_2, inductor L_2, and capacitor C_2 is designed to have a very high quality factor and resonate at the idler frequency ω_2 so that it is a short at all frequencies except ω_2. This results in an impedance conversion matrix of

$$\hat{\mathbf{Z}}_{\text{idler}} \approx \begin{bmatrix} \frac{1}{G_2+\mathrm{j}\omega_1 C_2-\frac{\mathrm{j}}{\omega_1 L_2}} & 0 \\ 0 & \frac{1}{G_2+\mathrm{j}\omega_2 C_2-\frac{\mathrm{j}}{\omega_2 L_2}} \end{bmatrix} \approx \begin{bmatrix} 0 & 0 \\ 0 & \frac{1}{G_2} \end{bmatrix}. \tag{4.6}$$

Similarly, the signal subcircuit consisting of a shunt resistor G_1, inductor L_1, and capacitor C_1 and only resonates at the signal frequency ω_1 and has an impedance conversion matrix of

$$\hat{\mathbf{Z}}_{\text{signal}} \approx \begin{bmatrix} \frac{1}{G_1+\mathrm{j}\omega_1 C_1-\frac{\mathrm{j}}{\omega_1 L_1}} & 0 \\ 0 & \frac{1}{G_1+\mathrm{j}\omega_2 C_1-\frac{\mathrm{j}}{\omega_2 L_1}} \end{bmatrix} \approx \begin{bmatrix} \frac{1}{G_1} & 0 \\ 0 & 0 \end{bmatrix}. \tag{4.7}$$

Combing the conversion matrices in series, the conversion matrix of the time-varying capacitor and idler subcircuit works out to

$$\hat{\mathbf{Z}}_{3,\text{idler}} = \hat{\mathbf{Z}}_{\text{idler}} + \hat{\mathbf{Z}}_3 = \begin{bmatrix} 0 & \frac{1}{\mathrm{j}\omega_2 C_-} \\ \frac{1}{\mathrm{j}\omega_1 C_+} & \frac{1}{G_2} \end{bmatrix} \tag{4.8}$$

and is now the input impedance looking toward the time-varying capacitor and the idler subcircuit from the signal subcircuit. Since the signal subcircuit looks like a short circuit

at the idler frequency (and every frequency other than the signal frequency ω_1), the input impedance presented by the time-varying element and idler circuit at the signal frequency can be found using MoM impedance matrix identities as

$$Z_{\text{in}}(\omega_1) = Z_{11} - \frac{Z_{12}Z_{21}}{Z_{22}} = \frac{G_2}{\omega_1\omega_2|C_+|^2} \tag{4.9}$$

and the input admittance as

$$Y_{\text{in}}(\omega_1) = \frac{1}{Z_{\text{in}}(\omega_1)} = \frac{\omega_1\omega_2|C_+|^2}{G_2}. \tag{4.10}$$

For amplification to occur, it is necessary for the input admittance/impedance to be negative, which can only occur when ω_2 is negative, so $\omega_1 < \omega_3$. Evaluating the circuit for $C = 0.0302\,\text{pF}$, $G_1 = 0.02\,\Omega^{-1}$, $G_2 = 10^{-6}\,\Omega^{-1}$, $\omega_1 = (2\pi)\,2\,\text{GHz}$, $\omega_2 = -(2\pi)\,1\,\text{GHz}$, and $\omega_3 = (2\pi)\,3\,\text{GHz}$ results in an input admittance at ω_1 of

$$Y_{\text{in}}(\omega_1) = -0.018 \tag{4.11}$$

Combining the input admittance with the signal subcircuit results in cancellation of most of the signal subcircuit conductance, leading to amplification of the signal. The total input admittance/impedance is then

$$Y_{\text{total}}(\omega_1) = 0.002 \tag{4.12}$$

and, given an excitation of $1\,\text{A}$, results in a current at the load of

$$I_L = V_L G_1 = \frac{I_0}{Y_{\text{total}}} G_1 = 10.0\,\text{A}. \tag{4.13}$$

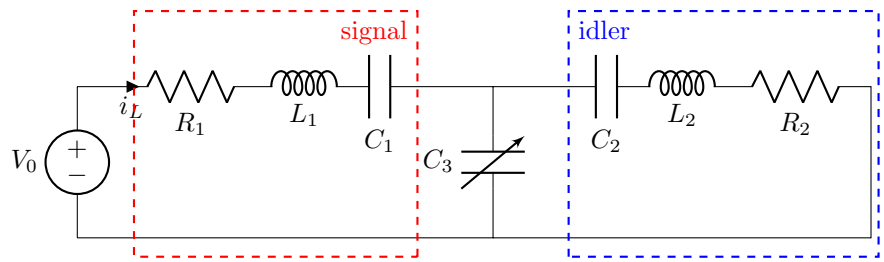

Figure 4.2: Shunt configuration of a parametric amplifier.

4.1.2 Shunt Configuration

Another potential parametric amplifier design is realized by placing the time-varying capacitor in shunt instead of series [83], [84]. For the previous series configuration, the overlying theory is that the two filters only allow a voltage to exist at their frequency, and the time-varying capacitor connects the two. In the shunt configuration shown in Figure 4.2, the opposite is true. The time-varying capacitor splits two filters, each only allowing a current to exist at their frequency. The circuit as a whole can be thought of as two loops of current, with the time-varying capacitor in the middle.

Similar to the previous design, the goal is to make the input impedance of the second loop to be near the negative resistance of the load.

As before in (4.1)-(4.4), we define the admittance conversion matrix of the time-varying capacitor as

$$\hat{\mathbf{Y}}_3 = \begin{bmatrix} 0 & \mathrm{j}\omega_1 C_+ \\ \mathrm{j}\omega_2 C_- & 0 \end{bmatrix} \tag{4.14}$$

and there is no need to convert to an equivalent conversion matrix impedance yet.

The idler and signal subcircuits series resonators, shown in the red and blue boxes of Figure 4.2, but are still designed to resonate at ω_2 and ω_1, respectively. They have an

admittance conversion matrix of

$$\hat{\mathbf{Y}}_{\text{idler}} \approx \begin{bmatrix} \frac{1}{R_2+\mathrm{j}\omega_1 L_2-\frac{\mathrm{j}}{\omega_1 C_2}} & 0 \\ 0 & \frac{1}{R_2+\mathrm{j}\omega_2 L_2-\frac{\mathrm{j}}{\omega_2 C_2}} \end{bmatrix} \approx \begin{bmatrix} 0 & 0 \\ 0 & \frac{1}{R_2} \end{bmatrix} \tag{4.15}$$

and

$$\hat{\mathbf{Y}}_{\text{signal}} \approx \begin{bmatrix} \frac{1}{R_1+\mathrm{j}\omega_1 L_1-\frac{\mathrm{j}}{\omega_1 C_1}} & 0 \\ 0 & \frac{1}{R_1+\mathrm{j}\omega_2 L_1-\frac{\mathrm{j}}{\omega_2 C_1}} \end{bmatrix} \approx \begin{bmatrix} \frac{1}{R_1} & 0 \\ 0 & 0 \end{bmatrix}. \tag{4.16}$$

The conversion matrix of the combined admittance of the idler and time-varying capacitor then becomes

$$\hat{\mathbf{Y}}_{3,\text{idler}} = \hat{\mathbf{Y}}_{\text{idler}} + \hat{\mathbf{Y}}_3 = \begin{bmatrix} 0 & \mathrm{j}\omega_1 C_+ \\ \mathrm{j}\omega_2 C_- & \frac{1}{R_2} \end{bmatrix} \tag{4.17}$$

looking toward the time-varying load and the idler subcircuit from the signal subcircuit. Since the signal subcircuit looks like an open circuit at the idler frequency, the input impedance presented by the time varying element and idler circuit at the signal frequency is

$$Y_{\text{in}}(\omega_1) = Y_{11} - \frac{Y_{12}Y_{21}}{Y_{22}} = \omega_1\omega_2 R_2 |C_+|^2 \tag{4.18}$$

which, when evaluated at $C = 0.0336\,\text{pF}$, $R_1 = 50\,\Omega$, $R_2 = 10^{-6}\,\Omega$, $\omega_1 = (2\pi)\,2\,\text{GHz}$, $\omega_2 = -(2\pi)\,1\,\text{GHz}$, and $\omega_3 = (2\pi)\,3\,\text{GHz}$ results in an input admittance and impedance at ω_1 of

$$Y_{\text{in}}(\omega_1) = -0.0222, \quad Z_{\text{in}}(\omega_1) = -45.0 \tag{4.19}$$

Combining the input impedance/admittance with the signal subcircuit results in cancellation of most of the signal subcircuit conductance, leading to amplification of the signal.

The total input admittance/impedance is then

$$Y_{\text{total}}(\omega_1) = 0.2, \quad Z_{\text{total}}(\omega_1) = 5 \tag{4.20}$$

and, given an excitation of $1\,\text{V}$, results in a voltage at the load of

$$V_L = I_L R_L = Y_{\text{total}} V_0 R_L = 10.00\,\text{V} \tag{4.21}$$

4.2 Realistic Time-varying Capacitor

The ideal time-varying capacitor in (4.1) assumes a capacitor can have both positive and negative capacitance, but actual capacitors cannot have a negative capacitance. Instead, a more realistic time-varying capacitance can be modeled with

$$C_3(t) = C\left(1 + b \sin \omega_L t\right) \tag{4.22}$$

where $b < 1$. Without changing the parametric amplifier design, the input impedance looking toward the time-varying capacitor and the idler subcircuit from the signal subcircuit cannot be negative, keeping the signal from being amplified. One solution, as shown in [85], is to add a tuning circuit in series with the time-varying capacitor, such as the one shown in Figure 4.3. This tuning circuit should be designed so that it cancels out the diagonal of the capacitor conversion matrix.

For example, the capacitance conversion matrix of the time-varying capacitor defined in (4.22) is

$$\hat{\mathbf{C}}_3 = \begin{bmatrix} C_0 & C_+ \\ C_- & C_0 \end{bmatrix} \tag{4.23}$$

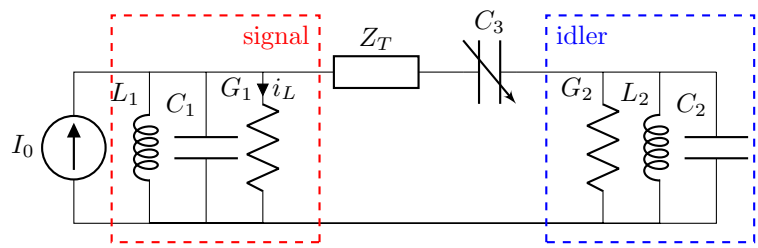

Figure 4.3: Tuning circuit Z_T shown in series with the time-varying capacitance C_3.

with the Fourier coefficients

$$C_- = -\mathrm{j}0.5bC, \quad C_0 = C, \quad C_+ = \mathrm{j}0.5bC \tag{4.24}$$

and a fundamental frequency of ω_3. By evaluating the matrix at frequencies ω_1 and ω_2 as before, the resulting admittance and impedance conversion matrices become

$$\hat{\mathbf{Y}}_3 = \mathrm{j}\hat{\mathbf{\Omega}}\hat{\mathbf{C}}_3 = \begin{bmatrix} \mathrm{j}\omega_1 C_0 & \mathrm{j}\omega_1 C_+ \\ \mathrm{j}\omega_2 C_- & \mathrm{j}\omega_2 C_0 \end{bmatrix} \tag{4.25}$$

and

$$\hat{\mathbf{Z}}_3 = \hat{\mathbf{Y}}_3^{-1} = \frac{1}{\omega_1\omega_2(C_0^2 - |C_+|^2)} \begin{bmatrix} -\mathrm{j}\omega_2 C_0 & \mathrm{j}\omega_1 C_+ \\ \mathrm{j}\omega_2 C_- & -\mathrm{j}\omega_1 C_0 \end{bmatrix}. \tag{4.26}$$

Then, the tuning circuit should have the impedance conversion matrix

$$\hat{\mathbf{Z}}_T = \frac{1}{\omega_1\omega_2(C_0^2 - |C_+|^2)} \begin{bmatrix} \mathrm{j}\omega_2 C_0 & 0 \\ 0 & \mathrm{j}\omega_1 C_0 \end{bmatrix} \tag{4.27}$$

so that the combined impedance of the time-varying capacitor and the tuning circuit becomes

$$\hat{\mathbf{Z}}_3 + \hat{\mathbf{Z}}_T = \frac{1}{\omega_1\omega_2(C_0^2 - |C_+|^2)} \begin{bmatrix} 0 & \mathrm{j}\omega_1 C_+ \\ \mathrm{j}\omega_2 C_- & 0 \end{bmatrix} \tag{4.28}$$

and can be used in the same way as the ideal time-varying capacitance in (4.5). It is important to realize that while the tuning circuit Z_T must be able to tune the time-varying capacitor at both ω_1 and ω_2 and some bandwidth around them, it does not need to tune the frequencies between them. In other words, if $\omega_1 = (2\pi)\,2\,\mathrm{GHz}$ and $\omega_2 = -(2\pi)\,1\,\mathrm{GHz}$ with a $100\,\mathrm{MHz}$ bandwidth, then the tuning circuit must only tune the time-varying capacitor for the $100\,\mathrm{MHz}$ bandwidth around $\omega_1 = (2\pi)\,2\,\mathrm{GHz}$ and $\omega_2 = (2\pi)\,1\,\mathrm{GHz}$.

Much of the rest of the derivation for the parametric amplifier with a realistic capacitor is the same as before, but the input admittance at ω_1 looking toward the time-varying capacitor and the idler subcircuit from the signal subcircuit changes to

$$Y_{\mathrm{in}}(\omega_1) = \frac{\omega_1\omega_2(C_0^2 - |C_+|^2)^2}{G_2|C_+|^2} \tag{4.29}$$

forcing a change in parameters, but can be used without other modifications.

4.3 Parametric Amplifier-Based Antenna Designs

With the two configurations of parametric amplifiers derived above, there are a few insights and basic antenna design schemes that can be directly applied. This section describes a few of them and their basic concepts so that they can be expanded upon in future research.

4.3.1 Amplifier

The first design is a direct application of a parametric amplifier onto an antenna. This would provide amplification directly on the antenna, instead of later in the receive chain, which could bypass the loss in an antenna, or cable loss between the antenna and a low-noise amplifier, and provide a better signal-to-noise ratio. Additionally, as shown in Section 4.2, a tuning circuit needs to be added to a time-varying capacitance to cancel out the static reac-

tance. The static reactance could instead be used to help tune the antenna, either allowing a simpler tuning circuit to be used or removing its need entirely.

4.3.2 Merging with an LTI System

The previous chapters show that conversion matrices and harmonic balance can be used to implement non-LTI components into an LTI system. Conversion matrices can be further applied to form an equivalent impedance matrix of a time-varying system, but eventually the time-varying device will need to be merged with an LTI system. Parametric amplifiers accomplish this by implementing the signal filter, shown as the red box in Figures 4.1, 4.2, and 4.3. This allows us to terminate the harmonics that are not desired and think of the antenna with a customary input impedance [15], [86].

4.3.3 Frequency Conversion

The final design scheme is a common variation on the typical parametric amplifier design. In the series configuration in Figure 4.1, the output of the amplifier is generally taken off of the signal filter conductance G_1, which results in an amplified signal at the excitation frequency. If the output is instead taken off of the idler filter conductance G_2, then the signal is converted to the harmonic frequency and used as the output signal, instead of being used to amplify the excitation frequency. If this configuration is implemented on an antenna, then an incoming signal can be mixed to a different frequency before propagating through the receive chain.

4.4 Concluding Remarks

This chapter analyzes parametric amplifiers as an example implementation of a time-varying component and gains insight from the different subcircuits and configurations. The conver-

sion matrix method presented in Chapter 3 was used to analyze the amplifier structure in order to extract design equations and establish the need for the tuning circuit and model its effect on the time-varying capacitor. Additionally, several antenna designs based on parametric amplifier configurations were identified to guide further research in this area. The next chapter seeks to expand on this insight and develop further design methods.

Chapter 5

Non-LTI Antenna Design

Previously, Chapters 2 and 3 derived different solvers that can be used to analyze antennas with non-LTI components and Chapter 4 discussed a few applications of time-varying components that give insight into how non-LTI components may be used. This chapter expands on the previous discussions and derives several design equations that highlight the effect that a non-LTI component has on an antenna, including the effect on impedance, extincted power, and matching. It then concludes with a discussion on performance bounds and realized non-LTI components.

5.1 CMMoM Design Equations

From the notation derived in Section 3.1, we can define a CMMoM impedance matrix $\hat{\mathbf{Z}}$ of a time-varying antenna as

$$\hat{\mathbf{V}} = \hat{\mathbf{Z}}\hat{\mathbf{I}} \tag{5.1}$$

where $\hat{\mathbf{V}}$ and $\hat{\mathbf{I}}$ are the voltage and current on each port of the impedance matrix as defined in (3.17). Let us now sort and partition the block frequencies into driven and non-driven frequencies as

$$\hat{\mathbf{Z}} = \begin{bmatrix} \hat{\mathbf{Z}}^{\mathrm{aa}} & \hat{\mathbf{Z}}^{\mathrm{ab}} \\ \hat{\mathbf{Z}}^{\mathrm{ba}} & \hat{\mathbf{Z}}^{\mathrm{bb}} \end{bmatrix} \tag{5.2}$$

so that

$$\begin{bmatrix} \hat{\mathbf{V}}^{\mathrm{a}} \\ \hat{\mathbf{V}}^{\mathrm{b}} \end{bmatrix} = \begin{bmatrix} \hat{\mathbf{Z}}^{\mathrm{aa}} & \hat{\mathbf{Z}}^{\mathrm{ab}} \\ \hat{\mathbf{Z}}^{\mathrm{ba}} & \hat{\mathbf{Z}}^{\mathrm{bb}} \end{bmatrix} \begin{bmatrix} \hat{\mathbf{I}}^{\mathrm{a}} \\ \hat{\mathbf{I}}^{\mathrm{b}} \end{bmatrix} \tag{5.3}$$

where $\hat{\mathbf{Z}}^{\mathrm{aa}}$ are the driven frequencies, $\hat{\mathbf{Z}}^{\mathrm{bb}}$ are the non-driven frequencies, and $\hat{\mathbf{Z}}^{\mathrm{ab}}$, $\hat{\mathbf{Z}}^{\mathrm{ba}}$ are the cross-frequency terms of the time-varying loading between frequencies of a and b. Additionally let us set the voltage excitation to be a single tone at $k = 0$ so that the excitation frequency $\omega_{ex} = \omega_c$ from (3.6). Using the quadratic form of (5.3), the voltage-current relationship over the equivalent network can be written out as

$$\hat{\mathbf{V}}^{\mathrm{a}} = \hat{\mathbf{Z}}^{\mathrm{aa}}\hat{\mathbf{I}}^{\mathrm{a}} + \hat{\mathbf{Z}}^{\mathrm{ab}}\hat{\mathbf{I}}^{\mathrm{b}} \tag{5.4}$$

and

$$\hat{\mathbf{V}}^{\mathrm{b}} = \hat{\mathbf{Z}}^{\mathrm{ba}}\hat{\mathbf{I}}^{\mathrm{a}} + \hat{\mathbf{Z}}^{\mathrm{bb}}\hat{\mathbf{I}}^{\mathrm{b}} \tag{5.5}$$

resulting in equations for current of

$$\hat{\mathbf{I}}^{\mathrm{a}} = \left(\hat{\mathbf{Z}}^{\mathrm{aa}} - \hat{\mathbf{Z}}^{\mathrm{ab}}(\hat{\mathbf{Z}}^{\mathrm{bb}})^{-1}\hat{\mathbf{Z}}^{\mathrm{ba}}\right)^{-1} \left(\hat{\mathbf{V}}^{\mathrm{a}} - \hat{\mathbf{Z}}^{\mathrm{ab}}(\hat{\mathbf{Z}}^{\mathrm{bb}})^{-1}\hat{\mathbf{V}}^{\mathrm{b}}\right) \tag{5.6}$$

and

$$\hat{\mathbf{I}}^{\mathrm{b}} = (\hat{\mathbf{Z}}^{\mathrm{bb}})^{-1}\hat{\mathbf{Z}}^{\mathrm{ba}} \left(\hat{\mathbf{Z}}^{\mathrm{aa}} - \hat{\mathbf{Z}}^{\mathrm{ab}}(\hat{\mathbf{Z}}^{\mathrm{bb}})^{-1}\hat{\mathbf{Z}}^{\mathrm{ba}}\right)^{-1} \left(\hat{\mathbf{Z}}^{\mathrm{ab}}(\hat{\mathbf{Z}}^{\mathrm{bb}})^{-1}\hat{\mathbf{V}}^{\mathrm{b}} - \hat{\mathbf{V}}^{\mathrm{a}}\right) + (\hat{\mathbf{Z}}^{\mathrm{bb}})^{-1}\hat{\mathbf{V}}^{\mathrm{b}} \tag{5.7}$$

for a given voltage excitation $\begin{bmatrix} \hat{\mathbf{V}}^{\mathrm{a}} & \hat{\mathbf{V}}^{\mathrm{b}} \end{bmatrix}^{\mathrm{T}}$. These expressions for current can be further simplified as

$$\hat{\mathbf{I}}^{\mathrm{a}} = \left(\hat{\mathbf{Z}}^{\mathrm{aa}} - \hat{\mathbf{Z}}^{\mathrm{ab}}(\hat{\mathbf{Z}}^{\mathrm{bb}})^{-1}\hat{\mathbf{Z}}^{\mathrm{ba}}\right)^{-1} \hat{\mathbf{V}}^{\mathrm{a}} \tag{5.8}$$

and

$$\hat{\mathbf{I}}^{\mathrm{b}} = -(\hat{\mathbf{Z}}^{\mathrm{bb}})^{-1}\hat{\mathbf{Z}}^{\mathrm{ba}}\left(\hat{\mathbf{Z}}^{\mathrm{aa}} - \hat{\mathbf{Z}}^{\mathrm{ab}}(\hat{\mathbf{Z}}^{\mathrm{bb}})^{-1}\hat{\mathbf{Z}}^{\mathrm{ba}}\right)^{-1}\hat{\mathbf{V}}^{\mathrm{a}} \tag{5.9}$$

because the frequencies of b are not driven, or $\hat{\mathbf{V}}^{\mathrm{b}} = 0$.

The previous two equations show how a voltage excitation on one frequency maps to currents on the same frequency as well as other harmonic frequencies in the presence of a time-varying load. While there are many interesting phenomena that could be analyzed by expanding the equation for the current at the generated harmonics, this sections focuses on the current produced at excitation frequencies, which is required for the analysis in Section 5.2.1.

In the case of an LTI antenna, or other structure, loaded with time-varying elements, an expression for an equivalent load can be derived. First, the impedance matrix of the time-varying antenna in (5.1) is redefined as

$$\hat{\mathbf{Z}} = \hat{\mathbf{Z}}_{\mathrm{U}} + \hat{\mathbf{Z}}_{\mathrm{TV}} = \begin{bmatrix} \hat{\mathbf{Z}}_{\mathrm{U}}^{\mathrm{aa}} & \hat{\mathbf{0}} \\ \hat{\mathbf{0}} & \hat{\mathbf{Z}}_{\mathrm{U}}^{\mathrm{bb}} \end{bmatrix} + \begin{bmatrix} \hat{\mathbf{Z}}_{\mathrm{TV}}^{\mathrm{aa}} & \hat{\mathbf{Z}}_{\mathrm{TV}}^{\mathrm{ab}} \\ \hat{\mathbf{Z}}_{\mathrm{TV}}^{\mathrm{ba}} & \hat{\mathbf{Z}}_{\mathrm{TV}}^{\mathrm{bb}} \end{bmatrix} \tag{5.10}$$

which has a similar structure to (3.17). Inspecting the structure of $\hat{\mathbf{Z}}^{\mathrm{ab}}$ and $\hat{\mathbf{Z}}^{\mathrm{ba}}$ in the above equation and (3.18b), it can be observed that they consist of diagonal submatrices with nonzero elements only where a time-varying load is placed on the structure. By sorting the frequency blocks $\hat{\mathbf{Z}}_{\mathrm{U}}^{\mathrm{xy}}$ and $\hat{\mathbf{Z}}_{\mathrm{TV}}^{\mathrm{xy}}$ by unloaded and loaded sections as in

$$\hat{\mathbf{Z}}_{\mathrm{U}}^{\mathrm{xy}} = \begin{bmatrix} \hat{\mathbf{Z}}_{\mathrm{U},uu}^{\mathrm{xy}} & \hat{\mathbf{Z}}_{\mathrm{U},ul}^{\mathrm{xy}} \\ \hat{\mathbf{Z}}_{\mathrm{U},lu}^{\mathrm{xy}} & \hat{\mathbf{Z}}_{\mathrm{U},ll}^{\mathrm{xy}} \end{bmatrix} \qquad \text{and} \qquad \hat{\mathbf{Z}}_{\mathrm{TV}}^{\mathrm{xy}} = \begin{bmatrix} \hat{\mathbf{0}} & \hat{\mathbf{0}} \\ \hat{\mathbf{0}} & \hat{\mathbf{Z}}_{\mathrm{TV},ll}^{\mathrm{xy}} \end{bmatrix} \tag{5.11}$$

where $\hat{\mathbf{Z}}_{uu}^{\mathrm{xy}}$ and $\hat{\mathbf{Z}}_{ll}^{\mathrm{xy}}$ correspond to the unloaded and loaded submatrices of the xy frequency

block and $\hat{\mathbf{Z}}^{\mathrm{xy}}_{ul}$ and $\hat{\mathbf{Z}}^{\mathrm{xy}}_{lu}$ are the cross-impedance terms between them, (5.8) can be written as

$$\hat{\mathbf{I}}^{\mathrm{a}} = \left(\hat{\mathbf{Z}}^{\mathrm{aa}}_{\mathrm{U}} + \begin{bmatrix} \hat{\mathbf{0}} & \hat{\mathbf{0}} \\ \hat{\mathbf{0}} & \hat{\mathbf{Z}}^{\mathrm{aa}}_{\mathrm{TV},ll} - \hat{\mathbf{Z}}^{\mathrm{ab}}_{\mathrm{TV},ll} \hat{\mathbf{Y}}^{\mathrm{bb}}_{ll} \hat{\mathbf{Z}}^{\mathrm{ba}}_{\mathrm{TV},ll} \end{bmatrix} \right)^{-1} \hat{\mathbf{V}}^{\mathrm{a}} \tag{5.12}$$

where

$$\hat{\mathbf{Y}}^{\mathrm{bb}}_{ll} = \left(\hat{\mathbf{Z}}^{\mathrm{bb}}_{\mathrm{U},ll} + \hat{\mathbf{Z}}^{\mathrm{bb}}_{\mathrm{TV},ll} - \hat{\mathbf{Z}}^{\mathrm{bb}}_{\mathrm{U},lu} (\hat{\mathbf{Z}}^{\mathrm{bb}}_{\mathrm{U},uu})^{-1} \hat{\mathbf{Z}}^{\mathrm{bb}}_{\mathrm{U},ul} \right)^{-1}, \tag{5.13}$$

resulting in an expression for the total effect of the time-varying loading of

$$\hat{\mathbf{Z}}^{\mathrm{aa}}_{\mathrm{TV},total} = \hat{\mathbf{Z}}^{\mathrm{aa}}_{\mathrm{TV},ll} - \hat{\mathbf{Z}}^{\mathrm{ab}}_{\mathrm{TV},ll} \hat{\mathbf{Y}}^{\mathrm{bb}}_{ll} \hat{\mathbf{Z}}^{\mathrm{ba}}_{\mathrm{TV},ll} \tag{5.14}$$

where the effect of the generated harmonics b on the driven frequencies a takes the form of an equivalent complex loading $\hat{\mathbf{Z}}^{\mathrm{ab}}_{\mathrm{TV},ll} \hat{\mathbf{Y}}^{\mathrm{bb}}_{ll} \hat{\mathbf{Z}}^{\mathrm{ba}}_{\mathrm{TV},ll}$ with the static loading of $\hat{\mathbf{Z}}^{\mathrm{aa}}_{\mathrm{TV},ll}$.

Note that the impedance matrix at the excitation frequencies remains unchanged by the loading except for the specific locations that have a time-varying structure, and the equivalent load is determined by the time-varying structure's static component $\hat{\mathbf{Z}}^{\mathrm{aa}}_{\mathrm{TV},ll}$, the harmonic content $\hat{\mathbf{Z}}^{\mathrm{ab}}_{\mathrm{TV},ll}$, $\hat{\mathbf{Z}}^{\mathrm{ba}}_{\mathrm{TV},ll}$, and by the admittance of the scatterer at harmonic frequencies that arise due to the time-varying loading $\hat{\mathbf{Y}}^{\mathrm{bb}}_{ll}$.

Some of the implications and design insight of the equivalent loading is difficult to extract without making assumptions about the load and the generated harmonics. In the next few sections, several assumptions will be made that will reduce the impedance matrix of the time-varying system. The insight gained from these assumptions can then be brought back to the full expression and utilized there.

5.1.1 Single Time-Varying Load

If it is assumed that the time-varying loading consists of a single time-varying load, then (5.12) reduces to

$$\hat{\mathbf{I}}^{\mathrm{a}} = \left(\hat{\mathbf{Z}}_{\mathrm{U}}^{\mathrm{aa}} + \begin{bmatrix} \hat{\mathbf{0}} & \hat{\mathbf{0}} \\ \hat{\mathbf{0}} & Z_{\mathrm{TV},ll}^{\mathrm{aa}} - \sum_{\mathrm{b}} \frac{Z_{\mathrm{TV},ll}^{\mathrm{ab}} Z_{\mathrm{TV},ll}^{\mathrm{ba}}}{Z_{in}^{\mathrm{bb}}} \end{bmatrix} \right)^{-1} \hat{\mathbf{V}}^{\mathrm{a}} \tag{5.15}$$

where Z_{in}^{bb} is the input impedance to the antenna at the location of the time-varying load, calculated similarly to (5.13) as

$$Z_{in}^{\mathrm{bb}} = \frac{1}{Y_{ll}^{\mathrm{bb}}} = Z_{\mathrm{U},ll}^{\mathrm{bb}} + Z_{\mathrm{TV},ll}^{\mathrm{bb}} - \hat{\mathbf{Z}}_{\mathrm{U},lu}^{\mathrm{bb}} (\hat{\mathbf{Z}}_{\mathrm{U},uu}^{\mathrm{bb}})^{-1} \hat{\mathbf{Z}}_{\mathrm{U},ul}^{\mathrm{bb}}. \tag{5.16}$$

This shows that the effect of each harmonic is added to the effect of the others. Then, if there is a desired behavior in one harmonic, it must be balanced against the other harmonics that are generated. This strategy is implemented later in Section 5.3.

5.1.2 Interaction Between Multiple Loads

If more than one time-varying load is placed on a scatterer, the $\hat{\mathbf{Z}}^{bb}$ matrix cannot be reduced to an input impedance as it was for a single load. Here, it is assumed that there are two time-varying loads located at m and n. Referring back to (5.12), the effective load of two

time-varying loads becomes

$$\hat{\mathbf{Z}}^{\mathrm{aa}}_{\mathrm{TV},ll} - \hat{\mathbf{Z}}^{\mathrm{ab}}_{ll}\hat{\mathbf{Y}}^{\mathrm{bb}}_{ll}\hat{\mathbf{Z}}^{\mathrm{ba}}_{ll} = \begin{bmatrix} \hat{\mathbf{Z}}^{\mathrm{aa}}_{mm} & 0 \\ 0 & \hat{\mathbf{Z}}^{\mathrm{aa}}_{nn} \end{bmatrix} - \begin{bmatrix} \hat{\mathbf{Z}}^{\mathrm{ab}}_{mm} & 0 \\ 0 & \hat{\mathbf{Z}}^{\mathrm{ab}}_{nn} \end{bmatrix} \begin{bmatrix} \hat{\mathbf{Y}}^{\mathrm{bb}}_{mm} & \hat{\mathbf{Y}}^{\mathrm{bb}}_{mn} \\ \hat{\mathbf{Y}}^{\mathrm{bb}}_{nm} & \hat{\mathbf{Y}}^{\mathrm{bb}}_{nn} \end{bmatrix} \begin{bmatrix} \hat{\mathbf{Z}}^{\mathrm{ba}}_{mm} & 0 \\ 0 & \hat{\mathbf{Z}}^{\mathrm{ba}}_{nn} \end{bmatrix} \tag{5.17}$$

$$= \begin{bmatrix} \hat{\mathbf{Z}}^{\mathrm{aa}}_{mm} - \hat{\mathbf{Z}}^{\mathrm{ab}}_{mm}\hat{\mathbf{Y}}^{\mathrm{bb}}_{mm}\hat{\mathbf{Z}}^{\mathrm{ab}}_{mm} & -\hat{\mathbf{Z}}^{\mathrm{ab}}_{mm}\hat{\mathbf{Y}}^{\mathrm{bb}}_{mn}\hat{\mathbf{Z}}^{\mathrm{ab}}_{nn} \\ -\hat{\mathbf{Z}}^{\mathrm{ab}}_{nn}\hat{\mathbf{Y}}^{\mathrm{bb}}_{nm}\hat{\mathbf{Z}}^{\mathrm{ba}}_{mm} & \hat{\mathbf{Z}}^{\mathrm{aa}}_{nn} - \hat{\mathbf{Z}}^{\mathrm{ab}}_{nn}\hat{\mathbf{Y}}^{\mathrm{bb}}_{nn}\hat{\mathbf{Z}}^{\mathrm{ab}}_{nn} \end{bmatrix} \tag{5.18}$$

where $\hat{\mathbf{Y}}^{\mathrm{bb}}_{mn}$ is the loaded admittance between ports m and n.

By observation, the main diagonal of the loading matrix above is equivalent to the equations derived for single time-varying loads, where the phase is solely dependent on the admittance of the scatterer at the harmonic frequency $\hat{\mathbf{Y}}^{\mathrm{bb}}_{ll}$. However, the off-diagonal elements' phase can be completely controlled by the relative phase of the two time-varying loads, allowing for more versatility than single time-varying loads can provide. Utilizing the off-diagonal loading may allow for more efficient tuning of scatterers.

5.2 Power Transfer and Loss

Now that an equivalent impedance matrix of a time-varying antenna has been derived, it can be used to design the time-varying aspect to improve the antenna and evaluate its performance. Specifically, here the power, loss, and efficiency of a time-varying antenna is analyzed and circuit models are used to determine where the power is lost or transferred in the antenna.

5.2.1 Extincted Power

One fundamental metric that is easily obtained from MoM-based models is the extincted power P_{ext}, which contains the sum of all power absorbed and scattered by the system. Extincted power is a measure of how much power from a given lumped source or incident-wave excitation interacts with the scatterer in any way, and increasing this quantity can indicate an improvement in performance. Extincted power is expressed in terms of the MoM current $\mathbf{I}$ and voltage $\mathbf{V}$ as [73]

$$P_{ext} = \frac{1}{2}\Re\left\{\mathbf{V}^{\mathrm{H}}\mathbf{I}\right\}. \tag{5.19}$$

Expanding this definition to CMMoM and partitioning the network as in (5.3), the expression becomes

$$P_{ext} = \frac{1}{2}\Re\left\{\begin{bmatrix}(\hat{\mathbf{V}}^{\mathrm{a}})^{\mathrm{H}} & (\hat{\mathbf{V}}^{\mathrm{b}})^{\mathrm{H}}\end{bmatrix}\begin{bmatrix}\hat{\mathbf{I}}^{\mathrm{a}}\\ \hat{\mathbf{I}}^{\mathrm{b}}\end{bmatrix}\right\} \tag{5.20}$$

and

$$P_{ext} = \frac{1}{2}\Re\left\{(\hat{\mathbf{V}}^{\mathrm{a}})^{\mathrm{H}}\hat{\mathbf{I}}^{\mathrm{a}} + (\hat{\mathbf{V}}^{\mathrm{b}})^{\mathrm{H}}\hat{\mathbf{I}}^{\mathrm{b}}\right\} = \frac{1}{2}\Re\left\{(\hat{\mathbf{V}}^{\mathrm{a}})^{\mathrm{H}}\hat{\mathbf{I}}^{\mathrm{a}}\right\}. \tag{5.21}$$

Using (5.12) to write $\hat{\mathbf{I}}^{a}$ in terms of $\hat{\mathbf{V}}^{a}$ and assuming that $\hat{\mathbf{V}}^{\mathrm{b}} = 0$ as before, the extincted power becomes

$$P_{ext} = \frac{1}{2}\Re\left\{(\hat{\mathbf{V}}^{\mathrm{a}})^{\mathrm{H}}\left(\hat{\mathbf{Z}}^{\mathrm{aa}} - \hat{\mathbf{Z}}^{\mathrm{ab}}(\hat{\mathbf{Z}}^{\mathrm{bb}})^{-1}\hat{\mathbf{Z}}^{\mathrm{ba}}\right)^{-1}\hat{\mathbf{V}}^{\mathrm{a}}\right\} \tag{5.22}$$

and in the case of time-varying loading, the extincted power simplifies to

$$P_{ext} = \frac{1}{2}\Re\left\{(\hat{\mathbf{V}}^{\mathrm{a}})^{\mathrm{H}}\left(\hat{\mathbf{Z}}_{\mathrm{U}}^{\mathrm{aa}} + \begin{bmatrix} \hat{\mathbf{0}} & \hat{\mathbf{0}} \\ \hat{\mathbf{0}} & \hat{\mathbf{Z}}_{\mathrm{TV},ll}^{\mathrm{aa}} - \hat{\mathbf{Z}}_{\mathrm{TV},ll}^{\mathrm{ab}}\hat{\mathbf{Y}}_{ll}^{\mathrm{bb}}\hat{\mathbf{Z}}_{\mathrm{TV},ll}^{\mathrm{ba}} \end{bmatrix}\right)^{-1}\hat{\mathbf{V}}^{\mathrm{a}}\right\} \tag{5.23}$$

where the equivalent loading matrix can be analyzed as in Sections 5.1.1 and 5.1.2. In order to maximize the extincted power of a passive system, it is necessary to cancel the non-Hermitian part of the impedance matrix, which results in an imaginary P_{ext}, while minimizing the losses and keeping the real part as small as possible. This is typically achieved with a tuning circuit and a network of capacitors and inductors, but it may be possible to accomplish it with a passive, time-varying component instead.

5.2.2 LTI Antenna Circuit Model

Now that the power extincted by the time-varying antenna has been calculated, the question remains as to what the antenna does with that power. Depending on the time-varying loading and the antenna, there could be more power lost using a time-varying component than power converted to something useful. As previously shown in section 5.1.1, the antenna can be made to resonate at the excitation frequency using a time-varying antenna, but much of its power is lost to the time-varying resistor. This section seeks to expand on the model of the time-varying loading and further develop expressions for how the power is used. For this derivation, a square loop antenna is configured to receive power from a plane wave excitation using a port with a characteristic impedance Z_c located on one side. In general, this configuration can be represented with an equivalent circuit model, such as the one shown in Figure 5.1. The power delivered to the load Z_c can be calculated with

$$P_c = (1 - |\Gamma|^2)P_{in} \tag{5.24}$$

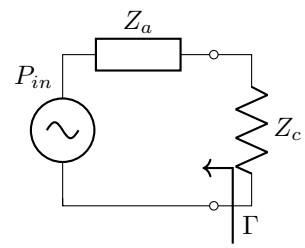

Figure 5.1: Equivalent circuit model of single-port antenna loaded with a port impedance Z_c. The antenna has an input impedance Z_a and input power P_{in} that change with the frequency and excitation as a function of the antenna geometry.

where Γ is the reflection coefficient between the antenna and the load and the power input to the antenna P_{in} can be calculated using the extincted power expression from the previous section, as

$$P_{in} = \frac{1}{2}\Re\left\{\hat{\mathbf{V}}^{\mathrm{H}}\hat{\mathbf{I}}\right\} = \frac{1}{2}\Re\left\{\hat{\mathbf{V}}^{\mathrm{H}}\hat{\mathbf{Z}}^{-1}\hat{\mathbf{V}}\right\}. \tag{5.25}$$

Similarly, the reflection coefficient Γ can be calculated with the impedances on either side of the boundary with

$$\Gamma = \frac{Z_c - Z_a^*}{Z_c + Z_a} \tag{5.26}$$

where Z_a is the input impedance to the antenna at the location of the port.

At low frequencies, the reactance of the loop antenna can be much greater than its resistance, leading to little power reaching the load Z_c due to the impedance mismatch. One common solution is to add a capacitor or inductor to the load to offset the reactance of the antenna, forcing a resonance at the operating frequency, as shown in Figure 5.2. With the added component, the expression for the reflection coefficient and power must change. Instead,

$$\Gamma = \frac{Z_{tot} - Z_a^*}{Z_{tot} + Z_a} \tag{5.27}$$

and

$$P_{tot} = (1 - |\Gamma|^2)P_{in} \tag{5.28}$$

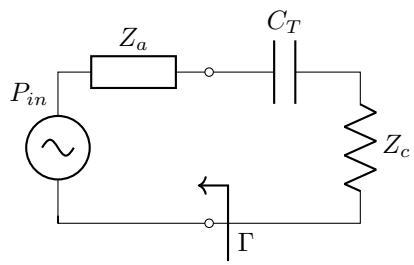

Figure 5.2: Equivalent circuit model of single-port antenna loaded with a tuning capacitance C_T and a port impedance Z_c. The added capacitance forces the antenna to resonate at the excitation frequency. The antenna has an input impedance Z_a and input power P_{in} that change with the frequency and excitation as a function of the antenna geometry.

where Z_{tot} is the total impedance of the load defined as

$$Z_{tot} = Z_c + Z_T \tag{5.29}$$

with $Z_T = R_T + \frac{1}{\mathrm{j}\omega C_T}$ and R_T is the series resistance of the tuning capacitor and C_T is its capacitance. Finally, the power across Z_c can be found with

$$P_c = \Re\{Z_c\}|I|^2 \tag{5.30}$$

where I is the current through the total load Z_{tot} calculated with

$$|I|^2 = \frac{P_{tot}}{\Re\{Z_{tot}\}}. \tag{5.31}$$

As a special note, in the case of a lossless tuning element ($R_T = 0$), then $P_c = P_{tot}$, and in the case of perfect tuning to create a matched load, $P_c = P_{in}$.

5.2.3 TV Antenna Circuit Model

In a similar way, the power in a time-varying structure can be calculated. The equivalent circuit for the power relations for an antenna loaded with a time-varying component is

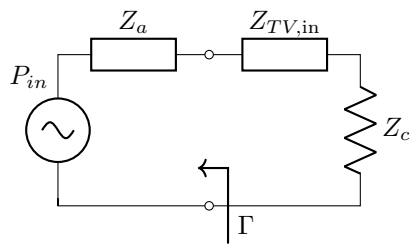

Figure 5.3: Equivalent circuit model of single-port antenna loaded with a port impedance Z_c and a time-varying component with an input impedance $Z_{TV,\text{in}}$. The time-varying component takes the place of the capacitor in Figure 5.2 and forces the antenna to resonate at a broad range of frequencies around the excitation frequency. The antenna has an input impedance Z_a and input power P_{in} that change with the frequency and excitation as a function of the antenna geometry.

shown in Figure 5.3 and is similar to the circuit of the reactively-tuned antenna of the previous section. This model can be used to accurately determine the effect of the time-varying element on the circuit once its input impedance is found at the excitation frequency, but it provides no insight as to what might be happening at the generated harmonic frequency or whether the power is simply being dissipated as heat. To that end, the derivation continues with the conversion matrix of the element.

For this example, the time-varying element is restricted to only generate a single harmonic so that its conversion matrix becomes

$$\hat{\mathbf{Z}}_{TV} = \begin{bmatrix} Z_{TV}^{00} & Z_{TV}^{01} \\ Z_{TV}^{10} & Z_{TV}^{11} \end{bmatrix} \tag{5.32}$$

where the superscripts 0 and 1 refer to the excitation frequency and the generated harmonic, respectively. This matrix implies that the time-varying element can be modeled as a two-port network connecting the antenna at the excitation frequency to the antenna at the generated harmonic. The circuit model of the loaded antenna can then be expanded with the new realization of the time-varying element, shown in Figure 5.4. Note that the notation for the antenna impedance has changed to add a superscript 0 or 1 to represent

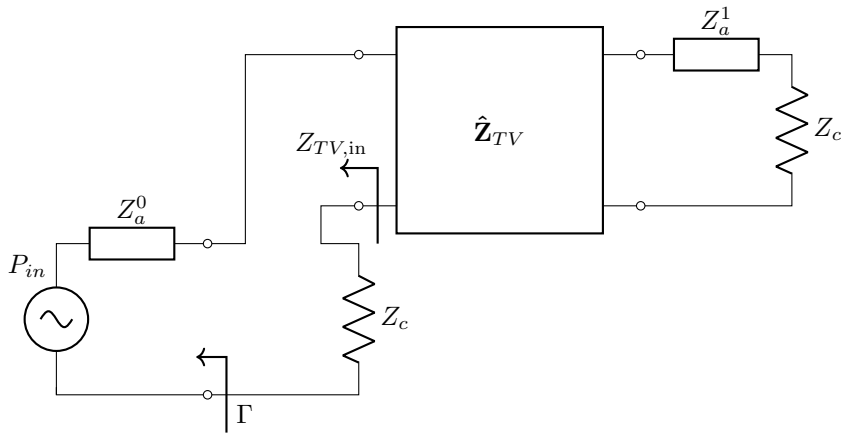

Figure 5.4: Equivalent circuit model of single-port antenna loaded with a port impedance Z_c and a time-varying component $\hat{\mathbf{Z}}_{TV}$. The time-varying component has been expanded into an equivalent two-port network and the antenna impedance at the harmonic frequency Z_a^1. The antenna has an input impedance Z_a^0 and input power P_{in} that change with the frequency and excitation as a function of the antenna geometry.

the impedance at the excitation frequency or the generated harmonic, respectively. Now it can be seen that the time-varying element acts as a coupler between the antenna circuit at the excitation frequency 0 and the antenna circuit at the generated harmonic 1. The port impedance Z_c has been included in the harmonic circuit here, but a filter could have been implemented to remove it at the harmonic frequency so that no power from the generated harmonic would be accepted by the port. Additionally, the input impedance of the time-varying element $Z_{TV,\text{in}}$ is shown to be the input impedance of the two-port network $\hat{\mathbf{Z}}_{TV}$ loaded with the equivalent circuit at the harmonic $Z_a^1 + Z_c$.

Expanding further on the model, we can represent the two-port network using dual resistors and dependent voltage sources in series on each port, shown in Figure 5.5. The model can now be analyzed as two separate, but interdependent, circuits. The input impedance of the time-varying load at the excitation frequency can be calculated as

$$Z_{TV,\text{in}} = Z_{TV}^{00} - \frac{Z_{TV}^{01} Z_{TV}^{10}}{Z_{TV}^{11} + Z_a^1 + Z_c} \tag{5.33}$$

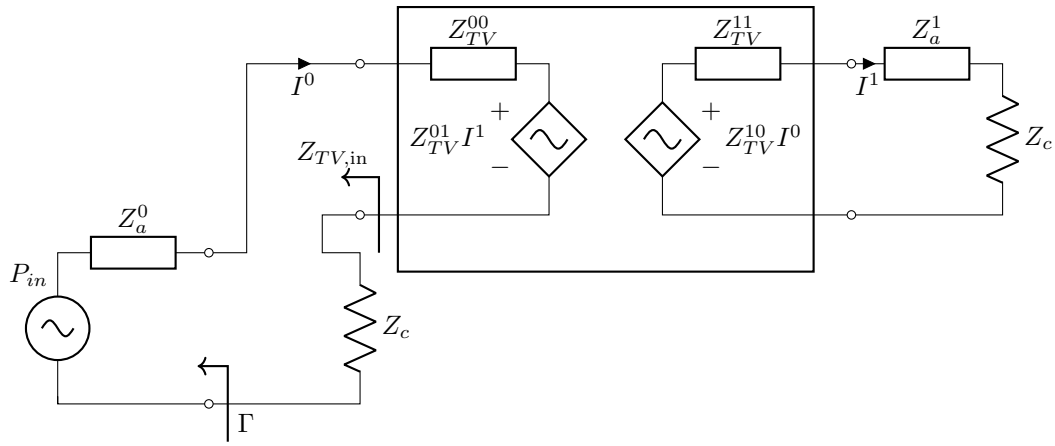

Figure 5.5: Equivalent circuit model of single-port antenna loaded with a port impedance Z_c and a time-varying component $\hat{\mathbf{Z}}_{TV}$. The time-varying component has been fully expanded into a dependent source model with the parameters from the time-varying component in (5.32). The antenna has an input impedance Z_a^0 and input power P_{in} that change with the frequency and excitation as a function of the antenna geometry.

which corresponds to the calculated effective load impedance from Section 5.1.1. Using the equations for power in Section 5.2.2, the expression for power across the port impedance Z_c at the excitation frequency can be calculated as

$$P_c^0 = P_{in}\left(1 - |\Gamma|^2\right) \frac{\Re\{Z_c\}}{\Re\{Z_c + Z_{TV,\text{in}}\}} \tag{5.34}$$

and similarly, the power across the port impedance Z_c at the harmonic frequency can be found with the current at the excitation circuit as

$$P_c^1 = P_{in}\left(1 - |\Gamma|^2\right) \frac{\Re\{Z_c\}}{\Re\{Z_c + Z_{TV,\text{in}}\}} \left| \frac{Z_{TV}^{10}}{Z_{TV}^{11} + Z_a^1 + Z_c} \right|^2 . \tag{5.35}$$

Other useful power expressions are the power lost to the time-varying element and the power radiated at the generated harmonic frequency. Power radiated at the harmonic frequency can be found using the real part of the antenna impedance at the harmonic frequency, assuming a lossless antenna. Similar to the equation for power across the port

impedance Z_c at the harmonic frequency, the power radiated at the harmonic can be written as

$$P_{rad}^1 = P_{in}\left(1-|\Gamma|^2\right)\frac{\Re\{Z_a^1\}}{\Re\{Z_c+Z_{TV,\text{in}}\}}\left|\frac{Z_{TV}^{10}}{Z_{TV}^{11}+Z_a^1+Z_c}\right|^2. \tag{5.36}$$

The power loss can then be determined with

$$P_{loss} = P_{tot} - \left(P_c^0 + P_c^1 + P_{rad}^1\right) \tag{5.37}$$

$$= P_{in}\frac{(1-|\Gamma|^2)}{\Re\{Z_c+Z_{TV,\text{in}}\}}\left(\Re\{Z_{TV,\text{in}}\} - \left|\frac{Z_{TV}^{10}}{Z_{TV}^{11}+Z_a^1+Z_c}\right|^2\Re\{Z_c+Z_a^1\}\right) \tag{5.38}$$

and efficiency using

$$\eta = \frac{P}{P_{in}}. \tag{5.39}$$

By comparing (5.33) and (5.38), it can be determined that the loss in the antenna is proportional to $\Re\{Z_{TV}^{00}\}$ and should be minimized to increase the efficiency of the antenna.

These power quantities have been derived for an antenna with the time-varying load $\hat{\mathbf{Z}}_L$ and the receive port Z_c located at the same location on the antenna and with a single generated harmonic. If they are located on different parts of the antenna, similar power quantities can be derived using the CMMoM method described in Chapter 3 and reducing the MoM impedance matrix of the antenna to a two-port matrix for the locations of the time-varying load and the receive port. If multiple harmonics are used, the two-port representation of the time-varying load becomes a 1+K port system, where K is the number of generated harmonics. Each of the additional ports is then loaded with mirrors of the excitation circuit evaluated at each of the harmonic frequencies. For example, a time-varying element on an antenna with K harmonics would have an input impedance of

$$Z_{TV,\text{in}} = Z_{TV}^{00} - \sum_{k=1}^{K}\frac{Z_{ll}^{0\text{k}}Z_{ll}^{\text{k}0}}{Z_{TV}^{\text{kk}}+Z_a^k+Z_c}. \tag{5.40}$$

5.3 Impedance Matching

It has been previously determined that a time-varying load can utilize the characteristics of an antenna at a generated harmonic frequency to produce a reactance. Now this property is utilized in order to attempt to replicate the tuning of the ideal reactance in Section 5.2.2 with a time-varying load.

Canceling the reactance allows a resonant structure at the excitation frequency, but the solution may have a narrow band. In order to achieve a broadband match using a complex load, the load must have the opposite reactance as the unloaded antenna over a broad spectrum of frequencies.

As shown in (5.33), the effective reactance of the time-varying load does not only depend on the time-varying element, but also the input impedance of the antenna at the generated harmonics. Using the natural resonances of the unloaded antenna, a time-varying element can be designed to utilize the antenna's impedance at other frequencies to tune the impedance at the excitation frequency.

Consider the loop antenna in Figure 5.6. It has a lumped port excitation on one side with a natural resonant frequency at 3 GHz. If this antenna needs to be used at 100 MHz or a similarly low frequency, the reactance of the antenna must be canceled to be used effectively. Let us assume we can use a sinusoidally time-varying resistor defined by

$$r_L(t) = r_0 \left(1 + |\gamma| \cos(\omega_0 t + \angle\gamma)\right) \tag{5.41}$$

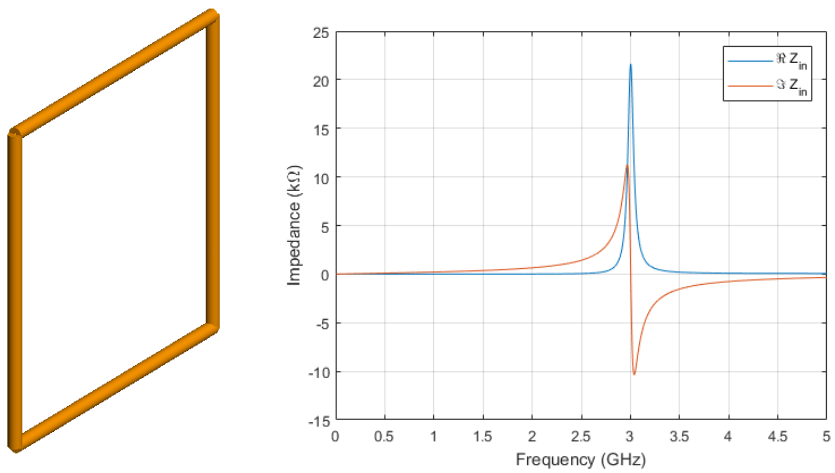

(a) Loop Antenna (b) Input Impedance

Figure 5.6: A square loop antenna with a side length of 12mm and driven by a lumped port excitation on one side. Its input impedance is shown in (b) and has a resonance at 3 GHz.

resulting in a conversion matrix of

$$\hat{\mathbf{R}}_L = r_0 \begin{bmatrix} 1 & \gamma/2 & 0 & \dots & 0 \\ \gamma^*/2 & 1 & \gamma/2 & \dots & 0 \\ 0 & \gamma^*/2 & 1 & \dots & 0 \\ \vdots & \vdots & \vdots & \ddots & \vdots \\ 0 & 0 & 0 & \dots & 1 \end{bmatrix} \tag{5.42}$$

where r_0 is a real, positive constant and γ is a complex number with $|\gamma| < 1$ defined as the modulation coefficient. This specific load type was chosen because it does not add any power to the system, as a negative $r(t)$ or a time-varying reactance would. From the effective input impedance (5.33), the time-varying resistor defined above can be implemented to use the 3 GHz resonance with a lower frequency excitation. For this antenna, a resistor with a magnitude of $r_0 = 860\,\Omega$ was used with $\gamma = 0.9$ and a pumping frequency of 3 GHz.

Shown in Figure 5.7.a, the reactance of the time-varying resistor almost entirely cancels

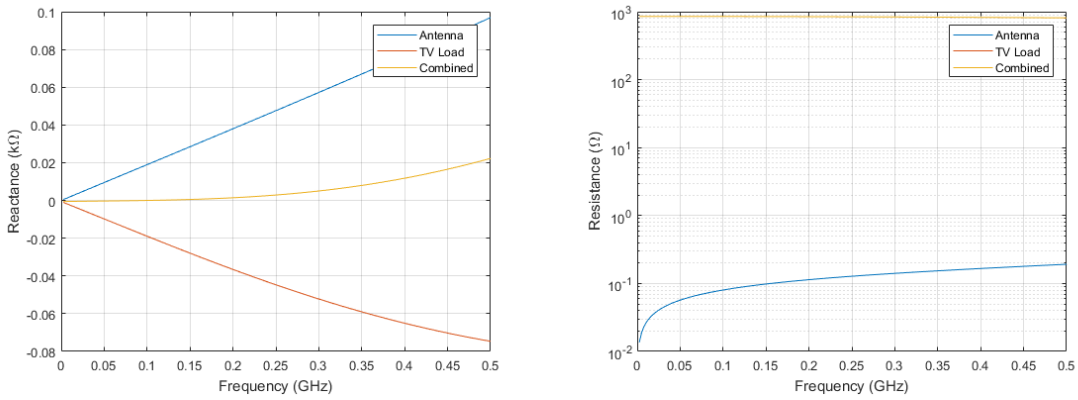

(a) Reactance

(b) Resistance

Figure 5.7: The square loop antenna from Figure 5.6 now tuned with a time-varying resistor at the excitation port. The time-varying resistor had a magnitude of $r_0 = 860\ \Omega$ and a frequency of 3 GHz. The reactance has been canceled for the lower frequencies as shown in (a), but the efficiency has been greatly reduced by the resistance of the load, shown in (b).

the reactance of the loop antenna for frequencies lower than 200 MHz, with a gradual increase at higher frequencies. But a time-varying resistor has a conversion matrix with a diagonal with a large real part, as shown in (5.42), that severely increases the loss of the antenna, shown in (5.38), and creating a large mismatch between the antenna and the effective load. Figure 5.7.b shows the comparison between the unloaded resistance of the antenna and the time-varying resistor. Figures 5.8, 5.9, and 5.10 show the power quantities for $Z_c = \Re\{Z_a^1\}$, $50\ \Omega$, and r_0, respectively, for the cases of the unloaded antenna from Figure 5.1, the antenna tuned with a capacitor from Figure 5.2, and the antenna tuned with a time-varying resistor from Figure 5.5. Note that for $Z_c = \Re\{Z_a^1\}$ and $50\ \Omega$ in Figures 5.8 and 5.9, the tuned case out-performs the unloaded and time-varying load cases. However when $Z_0 = r_0$, the time-varying load improves the average power received, though the tuned case still has a higher peak at the excitation.

One way to help mitigate the high impedance of the time-varying element is to allow more harmonics to be generated. Using a switching resistance instead of a sinusoidally

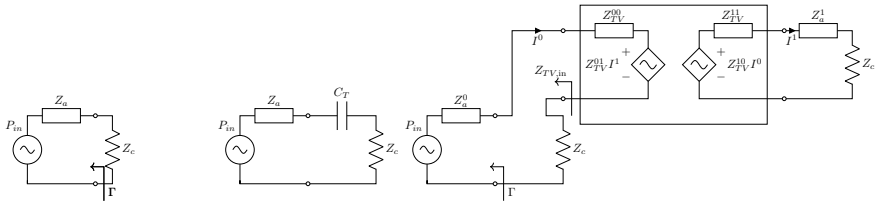

(a) Loading case

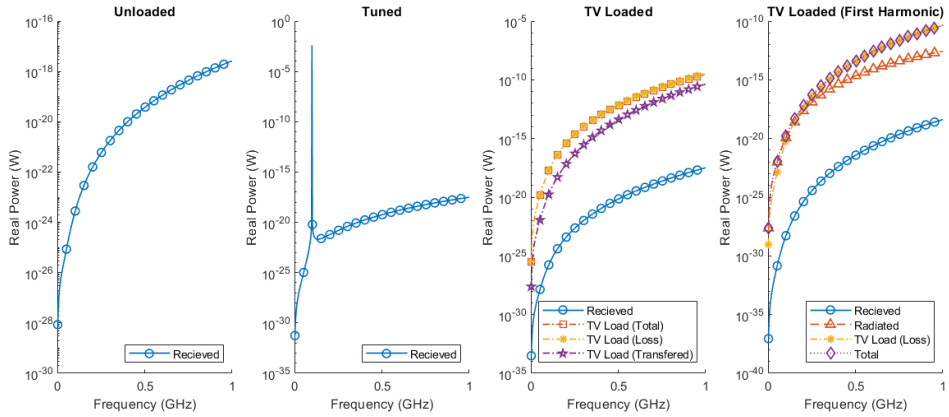

(b) Power quantities

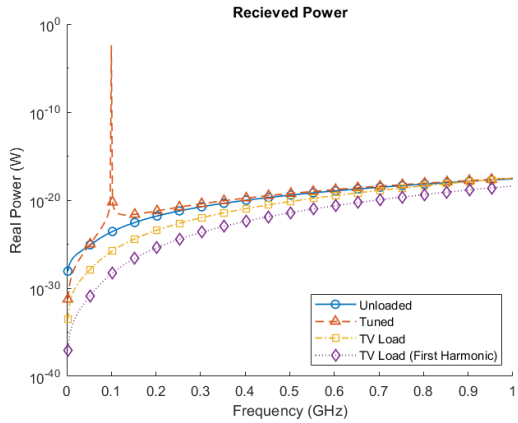

(c) Power recieved for each loading case

Figure 5.8: Power quantities on the square loop antenna from Figure 5.6 tuned with a sinusoidally time-varying resistor at the excitation port. The time-varying resistor had a magnitude of $r_0 = 860\ \Omega$ and a frequency of 3 GHz with one negative harmonic used and the port impedance Z_c is equal to the resistance of the antenna. The different power quantities derived in Section 5.2 are shown in (b) for different loading types and the power received by the port impedance Z_c is compared in (c).

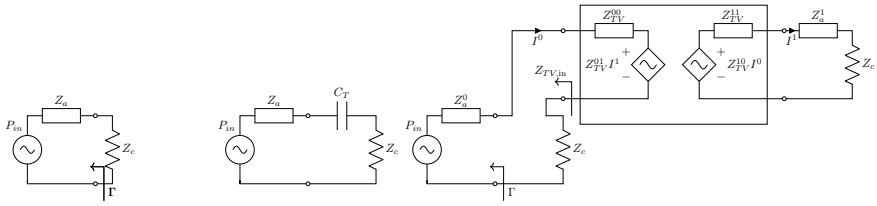

(a) Loading case

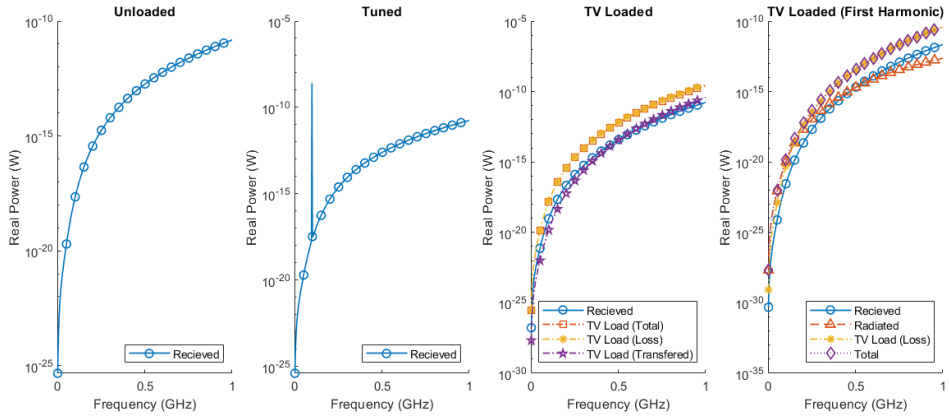

(b) Power quantities

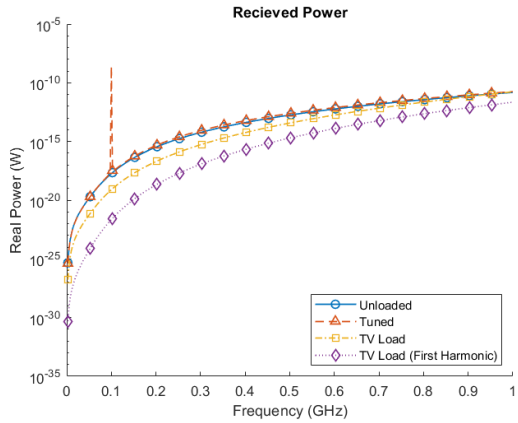

(c) Power recieved for each loading case

Figure 5.9: Power quantities on the square loop antenna from Figure 5.6 tuned with a sinusoidally time-varying resistor at the excitation port. The time-varying resistor had a magnitude of $r_0 = 860\ \Omega$ and a frequency of 3 GHz with one negative harmonic used and the port impedance Z_c is equal to $50\ \Omega$. The different power quantities derived in Section 5.2 are shown in (b) for different loading types and the power received by the port impedance Z_c is compared in (c).

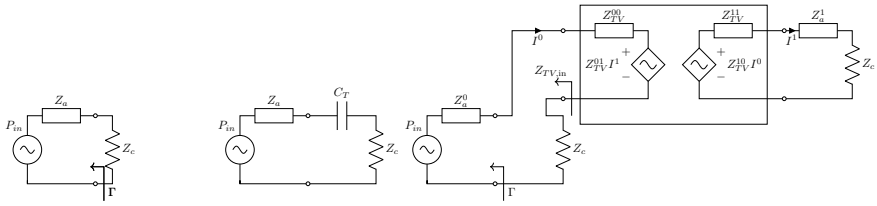

(a) Loading case

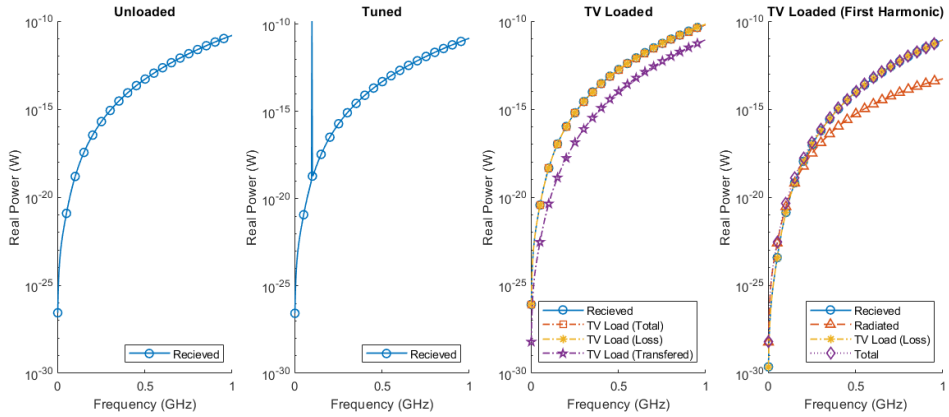

(b) Power quantities

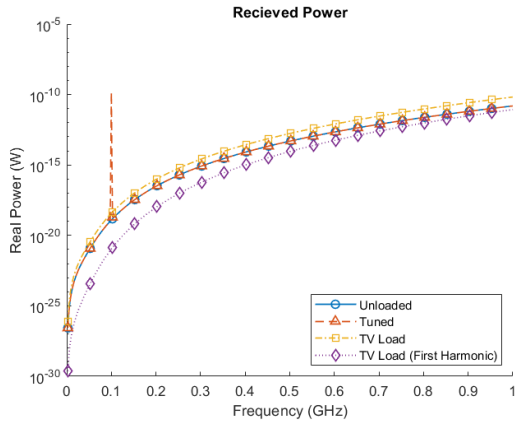

(c) Power recieved for each loading case

Figure 5.10: Power quantities on the square loop antenna from Figure 5.6 tuned with a sinusoidally time-varying resistor at the excitation port. The time-varying resistor had a magnitude of $r_0 = 860\ \Omega$ and a frequency of 3 GHz with one negative harmonic used and the port impedance Z_c is equal to the magnitude of the time-varying resistor. The different power quantities derived in Section 5.2 are shown in (b) for different loading types and the power received by the port impedance Z_c is compared in (c).

varying resistor and using 10 negative harmonics allowed the cancellation of the reactance of the loop with a magnitude of $r_0 = 687\ \Omega$, which reduces the loss by a small amount. Figures 5.11, 5.12, and 5.13 show the power quantities for $Z_c = \Re\{Z_a^1\}$, $50\ \Omega$, and r_0, respectively, for the cases of the unloaded antenna from Figure 5.1, the antenna tuned with a capacitor from Figure 5.2, and the antenna tuned with a switching time-varying resistance from Figure 5.5. Similar to the sinusoidal resistance, the tuned case receives more power at the excitation frequency of 100 MHz, with the time-varying load receiving a higher average power for $Z_c = r_0$. Additionally, compared to the sinusoidal resistance, the switching resistance shows a slight increase in total received power, due to the reduction in loss.

It is possible to circumvent the loss of efficiency entirely by using a time-varying capacitor instead of a resistor. The time-varying capacitor has a very small $\Re\{Z_{TV}^{00}\}$ from (5.33), reducing the loss significantly. Additionally, as shown in Chapter 4, a time-varying capacitor can be tuned to reduce its effect on the system and amplify the incoming signal. Using the method shown here, it may also be possible to use it as a matching network for an antenna, allowing an effective means of broadband impedance matching and amplification.

5.4 Bounds on Performance Metrics

While the design equations and matrix manipulations in previous sections have provided insight into how a scatterer could be loaded with a time-varying structure and how one might be utilized, discovering what kind of scatterer would benefit from time-varying loads is also of importance. It has been shown for other MoM problems that currents on a given structure can be optimized for different performance metrics subject to a set of constraints using Lagrange multipliers [71], [87]. By analyzing the optimal current distributions, insight can be gained into how a particular kind of antenna can be designed. However, before these bounds can be used, they need to be expanded with conversion matrices and computed with

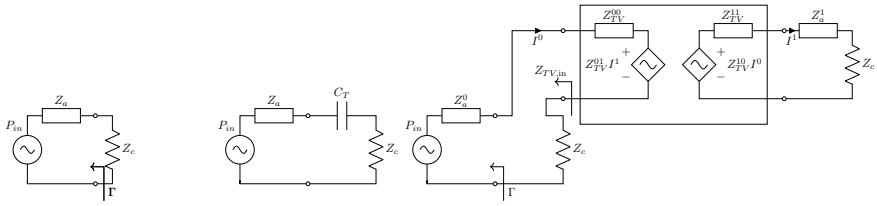

(a) Loading case

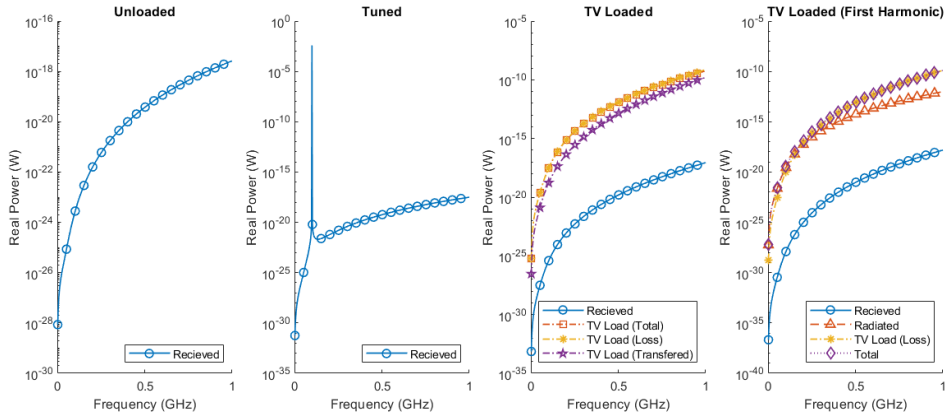

(b) Power quantities

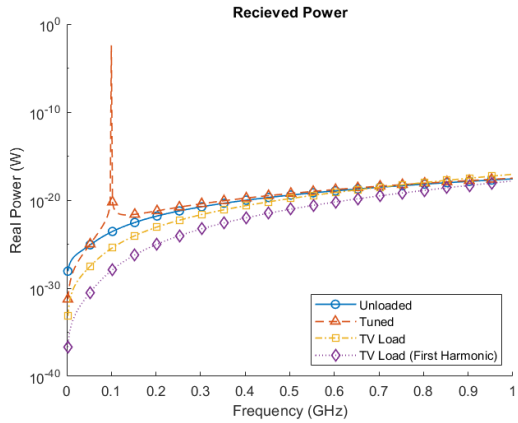

(c) Power recieved for each loading case

Figure 5.11: Power quantities on the square loop antenna from Figure 5.6 tuned with a switching time-varying resistor at the excitation port. The time-varying resistor had a magnitude of $r_0 = 687\ \Omega$ and a frequency of 3 GHz with 10 negative harmonics used and the port impedance Z_c is equal to the resistance of the antenna. The different power quantities derived in Section 5.2 are shown in (b) for different loading types and the power received by the port impedance Z_c is compared in (c).

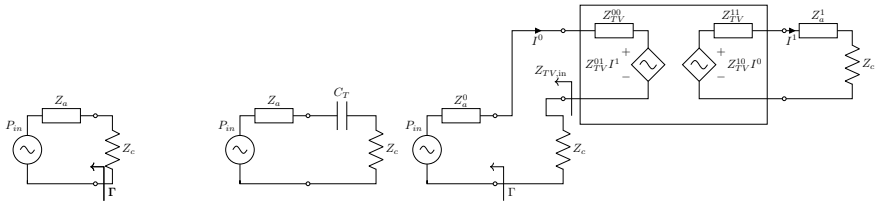

(a) Loading case

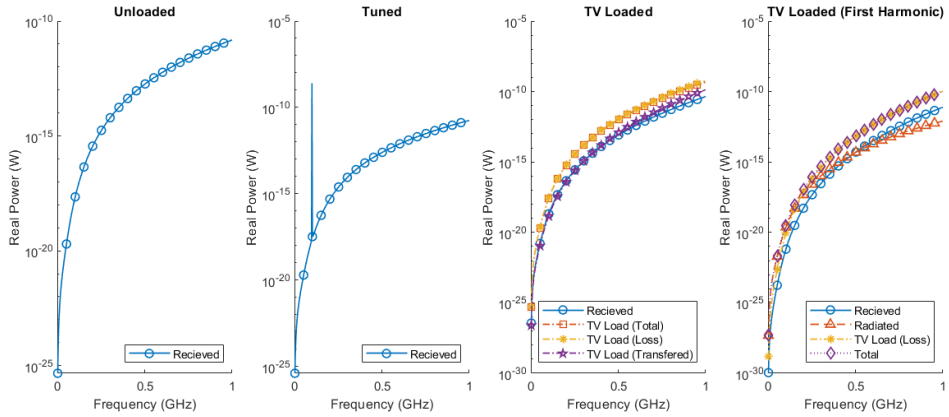

(b) Power quantities

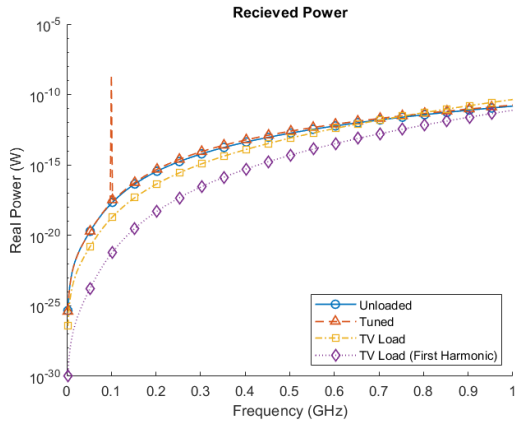

(c) Power recieved for each loading case

Figure 5.12: Power quantities on the square loop antenna from Figure 5.6 tuned with a switching time-varying resistor at the excitation port. The time-varying resistor had a magnitude of $r_0 = 687\ \Omega$ and a frequency of 3 GHz with 10 negative harmonics used and the port impedance Z_c is equal to $50\ \Omega$. The different power quantities derived in Section 5.2 are shown in (b) for different loading types and the power received by the port impedance Z_c is compared in (c).

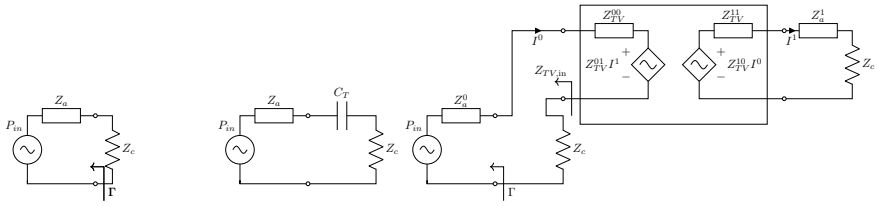

(a) Loading case

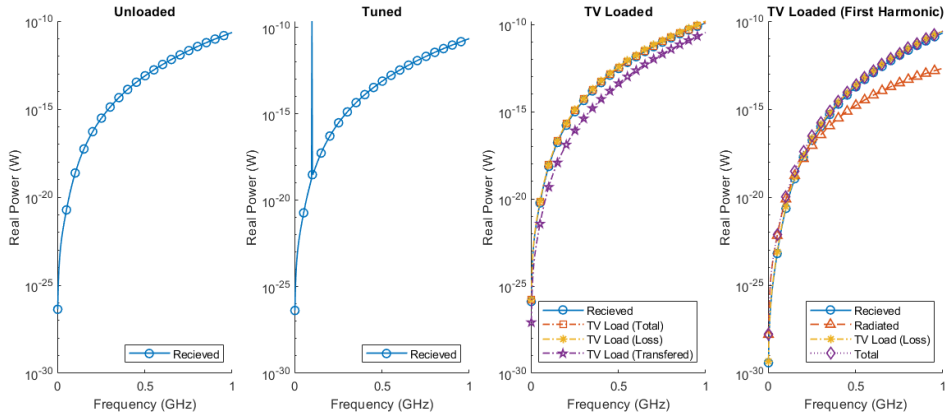

(b) Power quantities

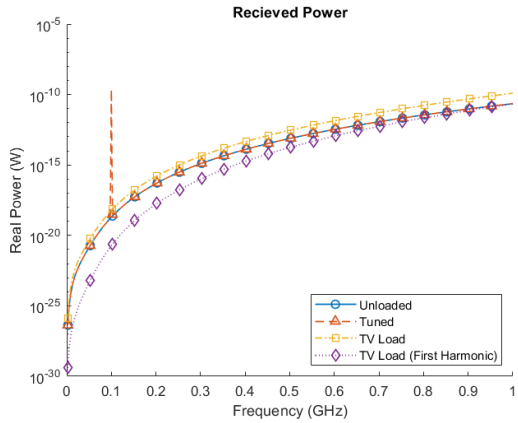

(c) Power recieved for each loading case

Figure 5.13: Power quantities on the square loop antenna from Figure 5.6 tuned with a switching time-varying resistor at the excitation port. The time-varying resistor had a magnitude of $r_0 = 687\ \Omega$ and a frequency of 3 GHz with 10 negative harmonics used and the port impedance Z_c is equal to the magnitude of the time-varying resistor. The different power quantities derived in Section 5.2 are shown in (b) for different loading types and the power received by the port impedance Z_c is compared in (c).

new constraints.

5.4.1 Perfectly Tuned Structures - R Bound

The first bound explored here, the R bound [87], finds an upper limit on the extincted power of a scatterer for a given excitation, assuming it can be perfectly tuned with lossless components. The bound was originally set up to maximize the extincted power P_{ext} with the constraint that all power had to come from the excitation and that power was conserved. In matrix form, this translates to

$$\begin{aligned} \text{maximize} \quad & \Re\left\{\mathbf{I}^{\mathrm{H}}\mathbf{V}\right\} \\ \text{subject to} \quad & \mathbf{I}^{\mathrm{H}}\mathbf{R}\mathbf{I} - \Re\left\{\mathbf{I}^{\mathrm{H}}\mathbf{V}\right\} = 0 \end{aligned} \tag{5.43}$$

where $\mathbf{V}$ is the excitation voltage, $\mathbf{I}$ is the resulting current vector on the scatterer, $\mathbf{R} = \Re\{\mathbf{Z}\}$, and $\mathbf{Z}$ is the MoM impedance matrix. Expanding this bound with conversion matrices requires converting each of the MoM matrices to CMMoM, as well as including another bound that restricts power from being created at a non-driven frequency, so that the new constraints for a time-varying scatterer with one generated harmonic at $k = 1$ become

$$\begin{aligned} \text{maximize} \quad & \Re\left\{\hat{\mathbf{I}}^{\mathrm{H}}\hat{\mathbf{V}}\right\} \\ \text{subject to} \quad & \hat{\mathbf{I}}^{\mathrm{H}}\hat{\mathbf{R}}^{0}\hat{\mathbf{I}} - \Re\left\{\hat{\mathbf{I}}^{\mathrm{H}}\hat{\mathbf{V}}\right\} = 0 \\ & \hat{\mathbf{I}}^{\mathrm{H}}\hat{\mathbf{R}}^{1}\hat{\mathbf{I}} = 0 \end{aligned} \tag{5.44}$$

where $\hat{\mathbf{R}}^0$ and $\hat{\mathbf{R}}^1$ are matrices containing the rows for an excitation at $k = 0$ and $k = 1$, respectively, and zeros elsewhere so that $\hat{\mathbf{R}}^0 + \hat{\mathbf{R}}^1 = \hat{\mathbf{R}}$. Solving this bound using Lagrange multipliers produces a solution of

$$P_{ex}^{opt} = \hat{\mathbf{V}}^{\mathrm{H}}\hat{\mathbf{R}}^{-1}\hat{\mathbf{V}} \tag{5.45}$$

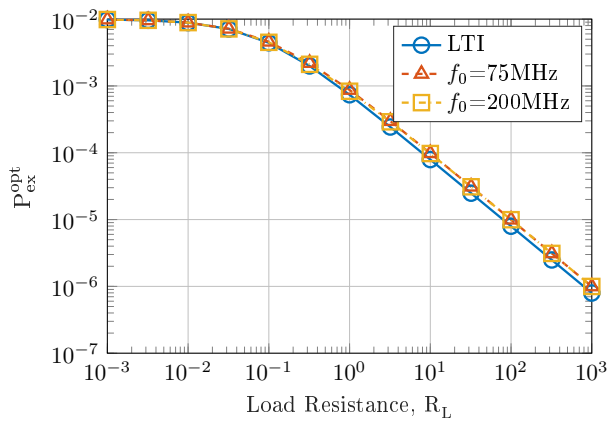

Figure 5.14: Optimal extincted power P_{ex}^{opt} using the R bound for a sphere of radius $a = 1$ cm at 100 MHz with a surface resistance $R_s = 0.01\ \Omega$. Results shown for the LTI case of a static load resistance and two different load frequencies f_0.

where P_{ex}^{opt} is the upper bound for extincted power. The R bound for CMMoM has been analyzed over a couple of cases, shown in Figure 5.14. Some improvement is seen when harmonics are present on the scatterer, but for the perfectly-tuned case, it is better to have a low-loss system, even if the loss is time-varying.

5.4.2 Efficiency Bound

One of the benefits from time-varying passive components is that they produce reactive power that can be used to tune scatterers. This final bound looks for an optimal utilization of this property by optimizing for efficiency and requiring that the scatterer is self-resonant. Specifically, the bound minimizes power loss for a specified radiated power, while maintaining no reactive power. For an LTI MoM scatterer, the constraints take the form

$$\begin{aligned} \text{minimize} \quad & \mathbf{I}^{\mathrm{H}}\mathbf{R}_{\Omega}\mathbf{I} \\ \text{subject to} \quad & \mathbf{I}^{\mathrm{H}}\mathbf{R}_{r}\mathbf{I} = 1 \\ & \mathbf{I}^{\mathrm{H}}\mathbf{X}\mathbf{I} = 0 \end{aligned} \tag{5.46}$$

where $\mathbf{R}_\Omega$ is the loss matrix, $\mathbf{R}_r$ is the radiation matrix, and $\mathbf{X}$ is the reactance matrix defined so that $\mathbf{R}_\Omega + \mathbf{R}_r + \mathrm{j}\mathbf{X} = \mathbf{Z}$. Note that the load in this case is purely resistive, and is contained inside the loss matrix as $\mathbf{R}_\Omega = \mathbf{R}_s + \mathbf{R}_L$ where $\mathbf{R}_s$ is the surface resistance of the structure. As before, expanding this bound to CMMoM requires some modification. The expression for power loss in nearly unchanged so that it takes into account power lost at all frequencies, but the radiated power and reactive power now contain a selection matrix $\hat{\mathbf{S}}$ to specify the radiation and reactance of the excitation frequency, so that

$$\begin{aligned} \text{minimize} \quad & \hat{\mathbf{I}}^{\mathrm{H}}\hat{\mathbf{R}}_\Omega\hat{\mathbf{I}} \\ \text{subject to} \quad & \hat{\mathbf{I}}^{\mathrm{H}}\hat{\mathbf{S}}\hat{\mathbf{R}}_r\hat{\mathbf{I}} = 1 \\ & \hat{\mathbf{I}}^{\mathrm{H}}\hat{\mathbf{S}}\hat{\mathbf{X}}\hat{\mathbf{I}} = 0 \end{aligned} \tag{5.47}$$

where the reactance matrix is redefined as

$$\hat{\mathbf{S}}\hat{\mathbf{X}} = \Im\left\{\hat{\mathbf{S}}\hat{\mathbf{Z}}\right\} + \frac{1}{2\mathrm{j}}\left(\hat{\mathbf{S}}\hat{\mathbf{R}}_L - \hat{\mathbf{R}}_L^{\mathrm{H}}\hat{\mathbf{S}}\right) \tag{5.48}$$

to take into account the reactive power produced by the time-varying load. The solution to this bound is more difficult to calculate and requires optimization functions to complete with the final expression of

$$P_\Omega^{opt} = \max_\nu \min eig\left(\hat{\mathbf{R}}_\Omega - \nu\hat{\mathbf{S}}\hat{\mathbf{X}}, \hat{\mathbf{S}}\hat{\mathbf{R}}_r\right) \tag{5.49}$$

where P_Ω^{opt} is the minimum bound for power loss. The maximum efficiency bound of the system η^{opt} can then be calculated with $\eta^{opt} = (1 + P_\Omega^{opt})^{-1}$.

The efficiency bound for CMMoM has been analyzed over a couple of cases, shown in Figures 5.15. In the case of a low loss structure ($R_s = 0.01\ \Omega$), we can draw a similar conclusion as before, that it is better to remove any source of loss, even if it is time-varying.

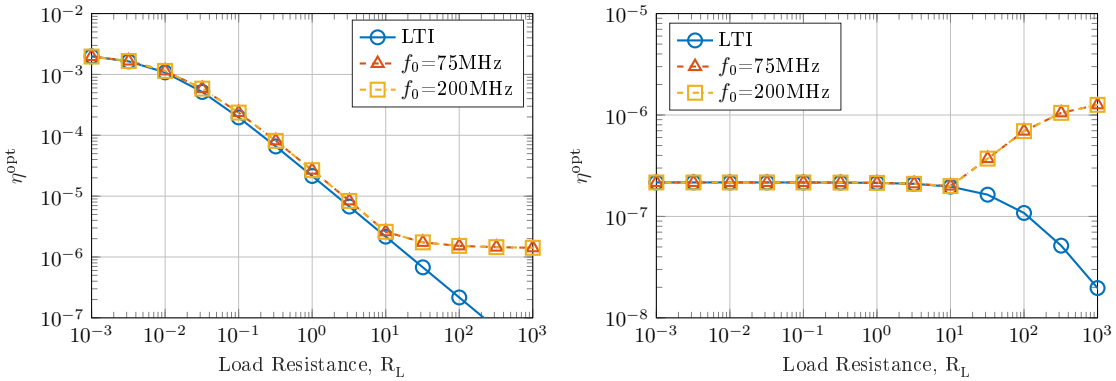

Figure 5.15: Efficiency bound for a sphere of radius $a = 1$ cm at 100 MHz with a surface resistance $R_s = 0.01\ \Omega$ (left) and $R_s = 100\ \Omega$ (right). Results shown for the LTI case of a static load resistance and two different load frequencies f_0.

However, in a high-loss structure ($R_s = 100\ \Omega$), we see an increase in efficiency with the addition of time-varying loading.

5.5 Realized Non-LTI Antenna Challenges

The previous sections and chapters have assumed that a nonlinear or time-varying component and load an electromagnetic structure could be obtained without difficulty or supporting components. In reality, non-LTI components are difficult to implement with a specific magnitude, nonlinearity, or frequency. This section discusses a few methods of realizing specific non-LTI components and the difficulties related to each.

5.5.1 Realized Components

There are a few high-speed switches available for purchase such as the ADG901/902 from Analog Devices which can be controlled with a voltage waveform to trigger their switching. These types of switches come in two varieties, reflective and absorptive, which determine how they treat the incoming signal in the open state. Reflective switches present an open-circuit impedance, leading to a high reflection, while an absorptive switch shorts to a $50\ \Omega$

load to keep a constant VSWR. In applications specific to this work, these switches allow for a reconfigurable design for the switching frequency, but it can only switch up to 20 MHz and cannot change the open-switch resistance, limiting its application.

A more versatile implementation uses a MOSFET or a varactor with a voltage bias and pumping circuit to realize a non-LTI resistance or capacitance, respectively [63]. Shown in Section 2.3, MOSFETs and varactors can be biased to operate in a nonlinear region, allowing for a configurable design. Additionally, if an external pumping voltage is applied to the bias of the MOSFET or varactor, each can be reduced to a time-varying component using large-signal/small-signal analysis from [26]. This method assumes the pumping voltage on the nonlinear component is significantly larger than the signal, allowing the pumped nonlinear component to be analyzed separately using the harmonic balance method from Chapter 2. The solution from harmonic balance can then be used as a time-varying component in a conversion matrix analysis because the small incoming signal will not have a large effect on the pumped component.

5.5.2 Non-LTI Measurements

Antenna measurements typically rely on LTI assumptions to accurately and rapidly extract the impedance, gain, and behavior of a device. Instruments drive the antenna with a single frequency at a time and measure the response at those frequencies, assuming there is no power generated at the non-driven frequencies. This approach works if there are no significant generated harmonic frequencies or if the driven frequency is the only interest. If the frequencies generated by the non-LTI behavior must be measured, another approach is necessary. Shown in [88], one method is to use a single-tone excitation and measure the response of a large bandwidth, and then change the excitation if a sweep is required. In this case, special calibration is required, often including cross-frequency terms as derived

in [88].

5.6 Concluding Remarks

This chapter discusses several applications of non-LTI antennas such as power, impedance matching, and performance bounds based on the conversion matrix method from Chapter 3 and the parametric amplifier discussion from Chapter 4. The conversion matrix of the time-varying system was analyzed by partitioning the matrix into driven and generated frequencies to enable analysis of input impedance and extincted power, and the time-varying components were analyzed as networks to calculate the power transfer.

While this chapter concludes the analysis and derivation of design equations for this dissertation, this is not a closed topic. Several possible models were derived here to model the effectiveness of a time-varying component, allowing conventional design techniques to be utilized. These models came from a direct application of CMMoM to design problems of impedance and power, and demonstrate the versatility and usefulness of analyzing time-varying structures in this way.

Chapter 6

Conclusions and Future Work

6.1 Conclusions

Interest into non-LTI antennas and other devices continues to grow as we seek to push beyond the capabilities and bounds of LTI systems. In order to accelerate the design of future non-LTI antennas, a versatile model must be established that enables the derivation of fundamental properties leading to rapid antenna design and analysis. To that end, harmonic balance and conversion matrices were combined with MoM, enabling the simulation and modeling of non-LTI electromagnetic structures.

Harmonic Balance

Harmonic balance is a well-known nonlinear circuit solver that uses a hybrid method to accurately model LTI and nonlinear components in the frequency or time domain. When expanded with MoM in Chapter 2, an antenna with nonlinear elements can effectively be solved for a given excitation. It was additionally shown that, with a modification, harmonic balance can be used to simulate periodically time-varying components as well, allowing harmonic balance to solve any non-LTI antenna.

Despite the versatility of harmonic balance, there is little insight that can be gained from its solution. This is due to the nature of nonlinear components where the response

depends nonlinearly on the magnitude of the excitation, removing the ability to model the device in the frequency domain. However, if nonlinearities are pumped with an external source, harmonic balance can be used to convert the nonlinear components into equivalent time-varying components with large-signal/small-signal analysis.

CMMoM

Conversion matrix-method of moments (CMMoM), derived in Chapter 3 is a recently-developed technique that combines conversion matrices and MoM to model periodically time-varying linear loads on an antenna. Due to the linearity inherent in both of the methods, their combination allows for the analysis of different frequencies as "ports" on the antenna allowing common frequency-domain methods to be applied. This connection can be directly utilized to derive equations for input impedance, reflection coefficient, and power that are important parameters in antenna design. Two different antenna designs with time-varying components were simulated with CMMoM to demonstrate its versatility and accuracy in comparison to common time-domain solvers.

Preliminary Designs

While CMMoM can accurately model time-varying scatterers, it is not immediately apparent how to derive design principles or fundamental bounds of the system. As a starting point, Chapter 4 analyzed different configurations of parametric amplifiers to determine how time-varying components have been used previously. The parametric amplifier design equations were re-derived using conversion matrices and established a need for a tuning circuit. Additionally, preliminary designs of time-varying antennas based on parametric amplifiers were established for future work.

In Chapter 5, the CMMoM matrix of the time-varying antenna was reduced in order to determine the effect of a time-varying load on an antenna. This included an analysis

of extincted power, power transferred to harmonic frequencies, and the input impedance at the antennas excitation. Additionally, a time-varying resistor was implemented to tune an antenna at the excitation frequency using the generated harmonics, but it was shown to generate too much loss to be an effective match. It was theorized that using a time-varying capacitor instead could provide a more efficient match, or amplify the signal if desired. Finally, several performance bounds were derived by optimizing over a set of constraints, providing an opportunity for future work.

6.2 Future Work

The work in this dissertation has opened up other opportunities for research on this topic, often outlining preliminary designs of antennas that utilize non-LTI loads. Additionally, there are topics that have been uncovered in this work, but need additional study to understand. This section specifies many of the future areas of research planned after this dissertation.

6.2.1 Combination of Harmonic Balance and CMMoM

Harmonic balance and CMMoM are presented in this work as two independent non-LTI solvers that focus on nonlinear and time-varying devices, respectively. The only overlap between them is when harmonic balance converts a pumped nonlinearity into an equivalent time-varying component for use in a conversion matrix analysis. However, the admittance matrix $\underline{\mathbf{Y}}$ in (2.11) of the harmonic balance method is similar in structure to the multiport impedance conversion matrix $\hat{\mathbf{Z}}$ in (3.20). This implies that the two methods could be combined in some way, enabling a versatile solution that can solve nonlinearities and time-varying components simultaneously.

6.2.2 Interactions between Time-Varying Components

Section 5.1.2 derives the equivalent loading on an antenna with two time-varying components, showing that the off-diagonal loading is present with multiple time-varying loads. Furthermore, the phase of the off-diagonal loading can be entirely controlled by varying the relative phase between the two loads. This suggests that an additional parameter can be utilized to improve the performance of an antenna so that distributed time-varying loads can be designed with a specified phase distribution, potentially expanding the capability of the system. Further research in this area will determine possible designs utilizing this property.

6.2.3 Antenna Designs

Throughout this work, particularly in Chapters 4 and 5, preliminary antenna designs that focus on a particular non-LTI characteristic were described for future work. Section 4.3 describes two antenna designs based on parametric amplifier configurations, including frequency conversion and an amplifier implementation. The frequency conversion design is further supported by the circuit model in Section 5.2.3, where the power transferred to a harmonic frequency is directly calculated. Section 5.3 continues with the circuit model and implements a basic time-varying resistor to tune the resonance of a loop antenna and suggests that using a time-varying capacitor would provide better performance.

6.2.4 Fundamental Bounds

Several fundamental bounds for antennas with a time-varying resistance were derived for a sphere in Section 5.4, including the R bound and the efficiency bound. Other bounds could be derived to assist in antenna design, such as the Z bound, which is similar to the R bound on extincted power, but does not assume a perfectly tuned structure. This allows the

tuning capability of a time-varying load, shown in Section 5.3, to be utilized to improve the antenna performance.

6.2.5 Data Integrity and Capacity

One goal in RF system design is the removal or mitigation of distortion or large sources of noise. However in many of the methods described in this work, non-LTI properties have intentionally been added to distort the incoming signal in specific ways. The intentional nature of the non-LTI properties may allow for a simple mitigation through signal analysis or matched filtering, but it has not yet been determined how data is distorted by a non-LTI antenna or how it can be mitigated. This must be investigated before non-LTI antennas can be used for communication.

6.3 Scientific Impact

As shown in the previous section, the work in this dissertation has opened up several new avenues of research with multiple planned articles based on the research done here. This section will describe the scientific contribution this work has made and list out the different publications and conferences that are planned or have already occurred. The publications and conferences over my academic career will be listed as well.

6.3.1 Dissertation Contributions

This work on non-LTI antenna modeling has provided several scientific contributions. First, two different methods of analyzing non-LTI antennas were established and tested. Each covers a different field, nonlinearities or time-variance, but are combined with MoM enabling them to solve a wide range of problems.

Parametric amplifiers were re-derived with conversion matrices, allowing for more versatility in their design and emphasizing the need for tuning circuits in their implementation. In the process, insight was gained on how to utilize time-varying structures in a system and several preliminary antenna designs were created.

The extincted power and the power transferred to the harmonic frequencies was derived using a partitioned CMMoM matrix. The derivation created an equivalent circuit model of a time-varying load and highlighted the effect it can have on an antenna. Additionally, a model for tuning an antenna was created based on the resulting input impedance.

Lastly, performance bounds for extincted power and efficiency, previously derived for MoM, were modified to allow for the multi-frequency structure of CMMoM. These bounds can help determine whether a given antenna structure can benefit from time-varying loading and provide an upper limit to the antenna's performance.

6.3.2 Publications and Conferences

Finally, this section details the publications and conferences over the course of my academic career to date. It includes work started at the undergraduate level up to the current work presented here.

6.3.2.1 Non-LTI Antenna Modeling

For the work in this dissertation, two conferences have been attended in the past two years and six articles are planned, including one that has already been submitted and is currently under review.

Articles - Accepted

- Bass, S., Cook A., Schab K., Kerby-Patel K., and Ruyle J., "Conversion matrix

method of moments for time-varying electromagnetic analysis," IEEE Transactions on Antennas and Propagation, Under Review. Estimated 2022.

Articles - Planned

- Bass, S., Kerby-Patel K., and Ruyle J., "On the theory of frequency-domain modeling of nonlinear loads on antennas," In Progress. Estimated 2022.
- Bass, S. and Schab, K., Correction to "Time-varying metamaterials based on graphene-wrapped microwires: Modeling and potential applications," In Progress. Estimated 2022.
- Bass, S., Kerby-Patel K., and Ruyle J., "Network relations between time-varying structures using conversion matrices," In Progress. Estimated 2023.
- Bass, S., Kerby-Patel K., and Ruyle J., "Conversion matrix analysis of parametric amplifiers for use in non-LTI antenna design," In Progress. Estimated 2023.
- Bass, S., Schab K., Kerby-Patel K., and Ruyle J., "Fundamental bounds of time-varying antennas using CMMoM," In Progress. Estimated 2024.

Conferences

- Bass, S., "Analyzing antennas with non-LTI loads using MoM". In 2020 Sixth Annual Intelligence Community Academic Research Symposium (ICARS), Sept. 2020.
- Bass, S., Schab, K., Kerby-Patel K., and Ruyle, J., "Investigation of electrically small antennas with time-varying elements to improve performance," in Proc. 2021 Antenna Applications Symposium, Allerton Park, Monticello, IL, Sept. 2021.

6.3.2.2 Unrelated Work

Conferences and articles unrelated to the work in this dissertation are listed here. There has been one article published with three conference submissions. An additional article is in process, nearing completion.

Articles - Published

- Bass, S., Ruyle, J., "Adaptation of Babinet's principle for complementary antennas in a dielectric half-space," IEEE Antennas and Wireless Propagation Letters, 18.2 (2019): 333-337.

Articles - In Progress

- Bass, S. and Ruyle J., "Frequency and pattern reconfigurable slot array utilizing ring resonator end loads," In Progress. Estimated 2022.

Conferences

- Bass, S., Hennessy, B., Szolc, L., and Ruyle, J., "Analysis of circularly polarized annular slot antennas to determine reconfiguration mechanism," in Proc. 2014 Antenna Applications Symposium, Allerton Park, Monticello, IL, Sept. 2014.
- Bass, S., Szolc, L., and Ruyle, J., "Investigation of pattern reconfigurability using three-element loaded slot array," in Proc. 2015 Antenna Applications Symposium, Allerton Park, Monticello, IL, Sept. 2015.
- Bass, S. and Ruyle, J., "Investigation of analytical solution for radiated fields of slot Yagi-Uda array through mutual coupling analysis". In 2017 IEEE International Symposium on Antennas and Propagation and USNC-URSI Radio Science Meeting, APSURSI 2017. Institute of Electrical and Electronics Engineers Inc.

References

[1] L. J. Chu, "Physical limitations of omni-directional antennas," *Journal of Applied Physics*, vol. 19, no. 12, pp. 1163–1175, 1948.

[2] H. A. Wheeler, "Fundamental limitations of small antennas," *Proc. of the IRE*, vol. 35, no. 12, pp. 1479–1484, 1947.

[3] R. Collin and S. Rothschild, "Evaluation of antenna Q," *IEEE Trans. Antennas Propag.*, vol. 12, no. 1, pp. 23–27, 1964.

[4] J. S. McLean, "A re-examination of the fundamental limits on the radiation Q of electrically small antennas," *IEEE Trans. Antennas Propag.*, vol. 44, no. 5, p. 672, 1996.

[5] S. R. Best, "A discussion on the quality factor of impedance matched electrically small wire antennas," *IEEE Trans. Antennas Propag.*, vol. 53, no. 1, pp. 502–508, 2005.

[6] A. Bahr, "On the use of active coupling networks with electrically small receiving antennas," *IEEE Trans. Antennas Propag.*, vol. 25, no. 6, pp. 841–845, 1977.

[7] E. Nordholt and D. Van Willigen, "A new approach to active antenna design," *IEEE Trans. Antennas Propag.*, vol. 28, no. 6, pp. 904–910, 1980.

[8] N. Zhu and R. W. Ziolkowski, "Broad-bandwidth, electrically small antenna augmented with an internal non-Foster element," *IEEE Antennas Wireless Propag. Lett.*, vol. 11, pp. 1116–1120, 2012.

[9] E. Daly and M. Daly, "The effect of phase continuity on synchronous antenna tuning," in *Proc. Intl. Symp. Antennas Propag.*, 2018, pp. 517–518.

[10] K. Schab, D. Huang, and J. J. Adams, "Pulse characteristics of a direct antenna modulation transmitter," *IEEE Access*, 2019.

[11] J. P. Dytioco Santos, F. Fereidoony, M. Hedayati, and Y. E. Wang, "High efficiency bandwidth VHF electrically small antennas through direct antenna modulation," *IEEE Trans. Microw. Theory Techn.*, vol. 68, no. 12, pp. 5029–5041, 2020.

[12] J. Landt, E. Miller, and F. Deadrick, "Time domain modeling of nonlinear loads," *IEEE Trans. Antennas Propag.*, vol. 31, no. 1, pp. 121–126, 1983.

[13] J. Hopf and H. Lindenmeier, "Fast tunable active receiving antennas," *Radio Science*, vol. 16, no. 6, pp. 1143–1147, 1981.

[14] X. Wang, L. P. B. Katehi, and D. Peroulis, "Time-varying matching networks for signal-centric systems," *IEEE Trans. Microw. Theory Techn.*, vol. 55, no. 12, pp. 2599–2613, 2007.

[15] P. Loghmannia and M. Manteghi, "An active cavity-backed slot antenna based on a parametric amplifier," *IEEE Trans. Antennas Propag.*, vol. 67, no. 10, pp. 6325–6333, 2019.

[16] E. Slevin, P. Singletary, K. Whitmore, B. Gurses, N. Opalinski, L. Thompson, M. B. Cohen, and M. Golkowski, "Broadband VLF/LF transmission from an electrically-small structure via time-varying antenna properties," in *IEEE APSURSI*, 2020, pp. 1663–1664. DOI: 10.1109/IEEECONF35879.2020.9330110.

[17] P. J. Singletary and M. B. Cohen, "Using a high-speed plasma as a conducting channel to enable a novel antenna approach," *IEEE Plasma Sci.*, pp. 1–11, 2021. DOI: 10.1109/TPS.2021.3052849.

[18] T. T. Koutserimpas and R. Fleury, "Electromagnetic waves in a time periodic medium with step-varying refractive index," *IEEE Trans. Antennas Propag.*, vol. 66, no. 10, pp. 5300–5307, 2018.

[19] D. Ramaccia, D. L. Sounas, A. Alù, F. Bilotti, and A. Toscano, "Nonreciprocity in antenna radiation induced by space-time varying metamaterial cloaks," *IEEE Antennas Wireless Propag. Lett.*, vol. 17, no. 11, pp. 1968–1972, 2018.

[20] C. Caloz and Z.-L. Deck-Léger, "Spacetime metamaterials—Part I: General concepts," *IEEE Transactions on Antennas and Propagation*, vol. 68, no. 3, pp. 1569–1582, 2019.

[21] ——, "Spacetime metamaterials—Part II: Theory and applications," *IEEE Transactions on Antennas and Propagation*, vol. 68, no. 3, pp. 1583–1598, 2019.

[22] M. R. Shcherbakov, P. Shafirin, and G. Shvets, "Overcoming the efficiency-bandwidth tradeoff for optical harmonics generation using nonlinear time-variant resonators," *Phys. Rev. A*, vol. 100, p. 063 847, 6 Dec. 2019. DOI: 10.1103/PhysRevA.100.063847. [Online]. Available: https://link.aps.org/doi/10.1103/PhysRevA.100.063847.

[23] N. Chamanara, Y. Vahabzadeh, and C. Caloz, "Simultaneous control of the spatial and temporal spectra of light with space-time varying metasurfaces," *IEEE Transactions on Antennas and Propagation*, vol. 67, no. 4, pp. 2430–2441, 2019. DOI: 10.1109/TAP.2019.2891706.

[24] Z. Wu and A. Grbic, "Serrodyne frequency translation using time-modulated metasurfaces," *IEEE Trans. Antennas Propag.*, vol. 68, no. 3, pp. 1599–1606, 2019.

[25] S. Taravati and A. A. Kishk, "Space-time modulation: Principles and applications," *IEEE Microw. Mag.*, vol. 21, no. 4, pp. 30–56, 2020.

[26] S. A. Maas, *Nonlinear microwave and RF circuits*. Artech House, 2003.

[27] M. B. Steer, "Simulation of nonlinear microwave circuits— an historical perspective and comparisons," in *IEEE MTT-S International Microwave Symposium Digest*, vol. 2, 1991, pp. 599–602.

[28] R. J. Gilmore and M. B. Steer, "Nonlinear circuit analysis using the method of harmonic balance—a review of the art. part i. introductory concepts," *International Journal of Microwave and Millimeter-Wave Computer-Aided Engineering*, vol. 1, no. 1, pp. 22–37, 1991.

[29] C. R. Chang, P. L. Heron, and M. B. Steer, "Harmonic balance and frequency-domain simulation of nonlinear microwave circuits using the block newton method," *IEEE transactions on microwave theory and techniques*, vol. 38, no. 4, pp. 431–434, 1990.

[30] T. J. Aprille and T. N. Trick, "Steady-state analysis of nonlinear circuits with periodic inputs," *Proceedings of the IEEE*, vol. 60, no. 1, pp. 108–114, 1972.

[31] Z.-X. Du, A. Li, X. Y. Zhang, and D. F. Sievenpiper, "A simulation technique for radiation properties of time-varying media based on frequency-domain solvers," *IEEE Access*, vol. 7, pp. 112 375–112 383, 2019.

[32] S. Bass, A. Palmer, K. Schab, K. Kerby-Patel, and J. Ruyle, "Conversion matrix method of moments for time-varying electromagnetic analysis," *arXiv preprint arXiv:2103.06135*, 2021.

[33] K. Schab, B. Shirley, and K. Kerby-Patel, "Scattering properties of spherical time-varying conductive shells," *arXiv preprint arXiv:2105.00058*, 2021.

[34] N. M. Krylov and N. N. Bogoliubov, *Introduction to non-linear mechanics*. Princeton University Press, 1949.

[35] G. Kirchhoff, "On the solution of the equations obtained from the investigation of the linear distribution of galvanic currents," *IRE transactions on circuit theory*, vol. 5, no. 1, pp. 4–7, 1958.

[36] A. R. Oliveira, "History of krylov-bogoliubov-mitropolsky methods of nonlinear oscillations," *Advances in Historical Studies*, vol. 6, no. 01, p. 40, 2017.

[37] M. Urabe, "Galerkin's procedure for nonlinear periodic systems," *Archive for Rational Mechanics and Analysis*, vol. 20, no. 2, pp. 120–152, 1965.

[38] ——, "Periodic solutions of differential systems, galerkin's procedure and the method of averaging," *Journal of differential equations*, vol. 2, no. 3, pp. 265–280, 1966.

[39] C. A. Fletcher, "Computational galerkin methods," in *Computational galerkin methods*, Springer, 1984, pp. 72–85.

[40] E. M. Baily, "Steady-state harmonic analysis of nonlinear networks.," 1969.

[41] J. C. Lindenlaub, "An approach for finding the sinusoidal steady state response of nonlinear systems," in *Proc. 7th Ann. Allerton Conf. Circuit and System Theory*, Univ. Illinois, 1969.

[42] S. Egami, "Nonlinear, linear analysis and computer-aided design of resistive mixers," *IEEE Transactions on Microwave Theory and Techniques*, vol. 22, no. 3, pp. 270–275, 1974.

[43] A. R. Kerr, "A technique for determining the local oscillator waveforms in a microwave mixer (short papers)," *IEEE Trans. Microw. Theory Techn.*, vol. 23, no. 10, pp. 828–831, 1975.

[44] M. Nakhla and J. Vlach, "A piecewise harmonic balance technique for determination of periodic response of nonlinear systems," *IEEE Transactions on Circuits and Systems*, vol. 23, no. 2, pp. 85–91, 1976.

[45] K. S. Kundert and A. Sangiovanni-Vincentelli, "Simulation of nonlinear circuits in the frequency domain," *IEEE Transactions on Computer-Aided Design of Integrated Circuits and Systems*, vol. 5, no. 4, pp. 521–535, 1986.

[46] F. Filicori, M. Scalas, and C. Naldi, "Nonlinear circuit analysis through periodic spline approximation," *Electronics Letters*, vol. 15, no. 19, pp. 597–599, 1979.

[47] R. Gilmore and F. Rosenbaum, "Modeling of in nonlinear distortion gaas mesfets," in *1984 IEEE MTT-S International Microwave Symposium Digest*, IEEE, 1984, pp. 430–431.

[48] L. Chua and A. Ushida, "Algorithms for computing almost periodic steady-state response of nonlinear systems to multiple input frequencies," *IEEE Transactions on circuits and systems*, vol. 28, no. 10, pp. 953–971, 1981.

[49] K. S. Kundert, G. B. Sorkin, and A. Sangiovanni-Vincentelli, "Applying harmonic balance to almost-periodic circuits," *IEEE transactions on microwave theory and techniques*, vol. 36, no. 2, pp. 366–378, 1988.

[50] V. Rizzoli, C. Cecchetti, A. Lipparini, and F. Mastri, "General-purpose harmonic balance analysis of nonlinear microwave circuits under multitone excitation," *IEEE Transactions on Microwave Theory and Techniques*, vol. 36, no. 12, pp. 1650–1660, 1988.

[51] J. J. Grainger, W. D. Stevenson, W. D. Stevenson, *et al.*, *Power system analysis*. 2003.

[52] *Harmonic balance simulation on ADS*, Agilent ADS, Jan. 2003.

[53] *Simulation and Analysis Guide*. National Instruments AWR, 2019.

[54] (2006). "Ansoft releases nexxim™ v3.0," [Online]. Available: https://www.microwavejournal.com/articles/12545-ansoft-releases-nexxim-v3-0 (visited on 11/08/2019).

[55] B. Wan and X. Wang, "Overview of commercially-available analog/rf simulation engines and design environment," in *2014 12th IEEE International Conference on Solid-State and Integrated Circuit Technology (ICSICT)*, IEEE, 2014, pp. 1–4.

[56] K. Gopal, M. Nakhla, K. Singhal, and J. Vlach, "Distortion analysis of transistor networks," *IEEE Transactions on Circuits and Systems*, vol. 25, no. 2, pp. 99–106, 1978.

[57] H. Floberg and S. Mattisson, "Symbolic distortion analysis of non-linear elements in feedback amplifiers using describing functions," *International journal of circuit theory and applications*, vol. 23, no. 4, pp. 345–356, 1995.

[58] V. Rizzoli, F. Mastri, and D. Masotti, "A hierarchial harmonic-balance technique for the efficient simulation of large-size nonlinear microwave circuits," in *1995 25th European Microwave Conference*, IEEE, vol. 2, 1995, pp. 615–619.

[59] S. Sancho, A. Suarez, and F. Ramirez, "Phase and amplitude noise analysis in microwave oscillators using nodal harmonic balance," *IEEE transactions on microwave theory and techniques*, vol. 55, no. 7, pp. 1568–1583, 2007.

[60] A. Demir, D. Long, and J. Roychowdhury, "Computing phase noise eigenfunctions directly from harmonic balance/shooting matrices," in *VLSI Design 2001. Fourteenth International Conference on VLSI Design*, IEEE, 2001, pp. 283–288.

[61] J. M. Ortega and W. C. Rheinboldt, *Iterative solution of nonlinear equations in several variables*. SIAM, 2000.

[62] E. Gluskin, "The use of non-linear capacitors," *international Journal of Electronics*, vol. 58, no. 1, pp. 63–81, 1985.

[63] A. S. Sedra and K. C. Smith, *Microelectronic Circuits*. Oxford University Press, 2010.

[64] A. Palmer, "Investigation of a generalized frequency domain method for modeling time-varying loads on antennas," M.S. thesis, University of Oklahoma, 2019.

[65] R. Garbacz and R. Turpin, "A generalized expansion for radiated and scattered fields," *IEEE Trans. Antennas Propag.*, vol. 19, no. 3, pp. 348–358, 1971.

[66] R. Harrington and J. Mautz, "Theory of characteristic modes for conducting bodies," *IEEE Trans. Antennas Propag.*, vol. 19, no. 5, pp. 622–628, 1971.

[67] Y. Rahmat-Samii and E. Michielssen, "Electromagnetic optimization by genetic algorithms," *Microw. J.*, vol. 42, no. 11, pp. 232–232, 1999.

[68] J. L. Ethier and D. A. McNamara, "Antenna shape synthesis without prior specification of the feedpoint locations," *IEEE Trans. Antennas Propag.*, vol. 62, no. 10, pp. 4919–4934, 2014.

[69] M. Capek, L. Jelinek, and M. Gustafsson, "Shape synthesis based on topology sensitivity," *IEEE Trans. Antennas Propag.*, vol. 67, no. 6, pp. 3889–3901, 2019.

[70] M. Gustafsson, D. Tayli, C. Ehrenborg, M. Cismasu, and S. Nordebo, "Antenna current optimization using MATLAB and CVX," *FERMAT*, vol. 15, no. 5, pp. 1–29, 2016.

[71] M. Gustafsson, M. Capek, and K. Schab, "Tradeoff between antenna efficiency and Q-factor," *IEEE Trans. Antennas Propag.*, vol. 67, no. 4, pp. 2482–2493, 2019.

[72] C. Jiang, T. K. Johanson, and V. Krozer, "Conversion matrix analysis of gaas hemt active gilbert cell mixers," in *INMMIC*, IEEE, 2006, pp. 94–97.

[73] R. F. Harrington, *Field computation by moment methods*. Wiley-IEEE Press, 1993.

[74] S. Rao, D. Wilton, and A. Glisson, "Electromagnetic scattering by surfaces of arbitrary shape," *IEEE Trans. Antennas Propag.*, vol. 30, no. 3, pp. 409–418, 1982.

[75] Y. Yeh and K. Mei, "Theory of conical equiangular-spiral antennas–Part I–Numerical technique," *IEEE Trans. Antennas Propag.*, vol. 15, no. 5, pp. 634–639, 1967. DOI: 10.1109/TAP.1967.1139029.

[76] D. Jiao and J.-M. Jin, "Fast frequency-sweep analysis of RF coils for MRI," *IEEE Trans. Biomed. Eng.*, vol. 46, no. 11, pp. 1387–1390, 1999.

[77] Y. H. Lo, S. He, L. Jiang, and W. C. Chew, "Finite-width gap excitation and impedance models," in *Proc. Intl. Symp. Antennas Propag.*, IEEE, 2011, pp. 1297–1300.

[78] XFDTD, Remcom 2020, version 7.8.1.4.

[79] Advanced Design System, Keysight 2020.

[80] J. M. Manley and H. E. Rowe, "Some general properties of nonlinear elements-Part I. General energy relations," *Proc. of the IRE*, vol. 44, no. 7, pp. 904–913, 1956.

[81] H. Heffner and G. Wade, "Gain, band width, and noise characteristics of the variable-parameter amplifier," *Journal of Applied Physics*, vol. 29, no. 9, pp. 1321–1331, 1958.

[82] W. J. Robertson, “Parametric amplifier design,” Ph.D. dissertation, The Ohio State University, 1959.

[83] A. Waksberg *et al.*, “An s-band parametric amplifier.,” 1960.

[84] G. Matthaei, “A study of the optimum design of wide-band parametric amplifiers and up-converters,” *IRE Transactions on Microwave Theory and Techniques*, vol. 9, no. 1, pp. 23–38, 1961.

[85] J. DeJager, “Maximum bandwidth performance of non-degenerate parametric amplifier with single-tuned idler circuit,” *IEEE Transactions on Microwave Theory and Techniques*, vol. 12, no. 4, pp. 459–467, 1964.

[86] A. Frost, “Parametric amplifier antenna,” *PROCEEDINGS OF THE INSTITUTE OF RADIO ENGINEERS*, vol. 48, no. 6, pp. 1163–1164, 1960.

[87] M. Gustafsson, K. Schab, L. Jelinek, and M. Capek, “Upper bounds on absorption and scattering,” *New J. Phys.*, 2020.

[88] K. Kanaly, “Design and validation of measurement methodology for time-varying scatterers and radiators,” M.S. thesis, The University of Oklahoma, Jan. 2022.